題目(和文)	
Title(English)	Study on Y2O3:Er,Yb Nanopararticles Prepared by Laser Ablation in Liquid
著者(和文)	布川貴史
Author(English)	Takashi Nunokawa
出典(和文)	学位:博士(工学), 学位授与機関:東京工業大学, 報告番号:甲第9494号, 授与年月日:2014年3月26日, 学位の種別:課程博士, 審査員:和田　裕之,小田原　修,吉本　護,中村　一隆,原　正彦
Citation(English)	Degree:Doctor (Engineering), Conferring organization: Tokyo Institute of Technology, Report number:甲第9494号, Conferred date:2014/3/26, Degree Type:Course doctor, Examiner:,,,,
学位種別(和文)	博士論文
Type(English)	Doctoral Thesis

A doctoral dissertation

Study on Y_2O_3:Er,Yb Nanoparticles Prepared by Laser Ablation in Liquid

Department of Innovative and Engineered Materials

Interdisciplinary Graduate School of Science and Engineering

Tokyo Institute of Technology

Takashi Nunokawa

March 2014

Supervised by

Associate Professor Hiroyuki Wada

Professor Osamu Odawara

List of Contents

Chapter 1 General introduction

1.1 Applications of fluorescent materials

In this section, applications of fluorescent materials are introduced. Rare-earth doped phosphors have attracted much attention by utilizing potential for luminescent materials and wavelength conversion. For example, rare-earth doped phosphors are applied as white LEDs, wavelength converting solar cell and imaging materials from device to biology. I will give a full detail of them.

1.1.1 Bio-imaging

Bio-imaging is technology that analyzes the body as image by capturing tissues, cells and protein. Mainly, early detection of tumor tissues is used. Quantum-dot semiconductors and fluorescent protein have ever been often researched. As representative quantum-dot semiconductors, CdSe, CdTe, and CdS have been researched [1-4]. Toxic materials, such as Cd are used. Short wavelength visible light (400-500 nm) is used as the excitation wavelength in the quantum-dot semiconductors. Also, in the fluorescent protein, it is a problem that the photo-fading rate is quick. Ultra violet light (200-400 nm) is used as the excitation wavelength in the fluorescent protein. In these materials, damages of the tissue and auto-fluorescence are problems by using a short wavelength. Therefore, fluorescent materials by excitation of long wavelength are desirable.

A. Biological window

In a human body, there is an area where light is easy to be transmitted. There is the area of the low absorption coefficient of hemoglobin (HbO_2) and water as a function of wavelength [5]. In a visible light area, there is an absorption area of the hemoglobin. Also, in an infrared area, there is an absorption area of the water. In near infrared area, however, the absorption of hemoglobin and water is low. The area is called as “biological window”. Therefore, a fluorescent probe in the area of both excitation and fluorescent wavelength, have been required.

B. Auto-fluorescence

In a bio-imaging, auto-fluorescence is a significant problem. An auto-fluorescence is phenomena that living substances are emitted by excitation light. The mouse abdomen is emitted by excitation light of 468 nm [6]. In excitation light of 468 nm, living substances are emitted. In a general, living substances are emitted by excitation light of short wavelength visible area. As representative living substances, there are vitamin group (Riboflavin and Vitamin B_6), Neurotransmitter (Serotonin and Catecholamine), amino acid (Tryptophan and

Tyrosine), and coenzyme (NADH and FAD) [7-9]. In excitation light of 980 nm, on the other hand, emission of living substances is not observed. In order to mark an objective tissue, fluorescent materials by excitation light above 500 nm are required.

C. EPR effect

To take the nanoparticles in tumor cells, particle size of nanoparticles is significant. The particle size of nanoparticles between 10 and 200 nm is required. This is called as EPR effect (Enhanced Permeability and Retention Effect) [10-12]. In the particle size under 10 nm, the nanoparticles are promptly eliminated by a kidney. In the particle size above 200 nm, the nanoparticles are taken in a liver by phagocytosis of Kupffer cells.

Upconversion nanoparticles emitting visible light by excitation of near infrared have attracted much attention. Bio-imaging have been often researched by using the upconversion nanoparticles because of the unique optical properties [6, 13-18]. Upconversion nanoparticles are prepared by doping activators (Er) and sensitizers (Yb) in the host materials, such as Y_2O_3 [14-16] and $NaYF_4$ [6, 13, 17-18]. Using the transmission of an excitation light and emission light, visualization of living cells is possible without a surgical operation. The mouse tumor cells are visualized by upconversion nanoparticles. It is a significant technology that the nanoparticles are transferred to certain cells. Various technologies that modify an antibody [19], peptide [20], and folic acid [21] on the surface of nanoparticles have been reported.

1.1.2 Photodynamic therapy (PDT)

One of the non-invasive cancer treatments includes photodynamic therapy (PDT). Cancer treatments by PDT are carried out in the next order. 1. Photosensitizer molecules (Talaporfin [22], Porfimer sodium [23], and Chlorin e6 [24]) are injected in a living body. 2. Living cells such as cancer cells are irradiated with light of a certain wavelength. 3. Active oxygen is generated by energy transfer of the excited photosensitizer. 4. The active oxygen killed cancer cells.

In a general, visible light is often used for light irradiated on the living light. However, it is difficult that light of low bio-permeability, such as visible light, is penetrated outside the body. Upconversion nanoparticles emitting visible light by irradiating near infrared light have attracted much attention. The research has been often reported recently [25-27]. Irradiating near infrared light of high bio-permeability, active oxygen is generated by visible light emitting from upconversion nanoparticles. (Figure 1-1)

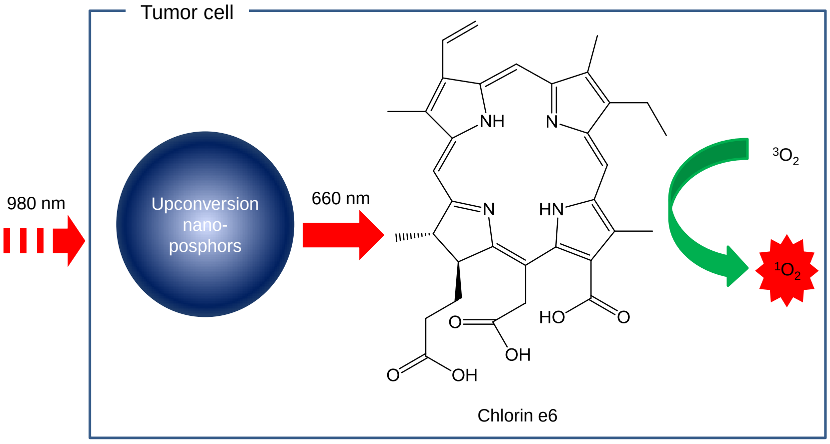

Figure 1-1. Generation of the active oxygen by combination of upconversion phosphor and chlorin e6

1.1.3 White light emission diode (LED)

As a new illuminated light source substituted for incandescent lamps and fluorescent lamps, white light emission diode (LED) is widely used. Advantages of white LED are high luminous efficiency, energy saving, environment friendliness, and long persistence. In the present, a widely prevailing white LED is often used for yellow phosphors (YAG:Ce) and blue LED [28] (Figure 1-2(a)). However, a problem of color rendering properties is pointed out that human skins look pale and a cooking does not look delicious. Therefore, researches, that emission wavelength shifts red and blue wavelength by doping Gd and Ga in YAG crystal respectively, have been often carried out [29]. Also, researches of the green and red phosphors emitting light by blue LED have been carried out (Figure 1-2(b)). White LEDs of the high color rendering properties are prepared by controlling the amount of the green and red phosphors. As a representative phosphors, researches of the sialon phosphor ($Sr_3Si_{13}Al_3O_2N_{21}:Eu^{2+}$) has been performed [30]. A sialon phosphor has attract an attention because it prevented from decreasing the luminous efficiency by thermal quenching, compared with YAG:Ce. As next generation white LED, furthermore, UV-LED and RGB phosphors are used. Red, green, and blue phosphors are emitted by excitation of UV-LED [31] (Figure 1-2(c)). In the blue phosphors, $BaMgAl_{10}O_{17}:Eu^{2+}$ [32] are used. In the green phosphors, uses of $(Sr,Ba)_2SiO_4:Eu^{2+}$ [33] and $Ba_3Si_6O_{12}N_2:Eu^{2+}$ [34] is considered. In the red phosphors, $CaAlSiN_3:Eu^{2+}$ [35] is used as well as white LED of excitation by blue LED. Also, upconversion phosphors have been researched for white LED [36, 37]. In the emission of the blue and red, Tm and Pr are used as dopant. In the emission of the green and red, Er is used as dopant.

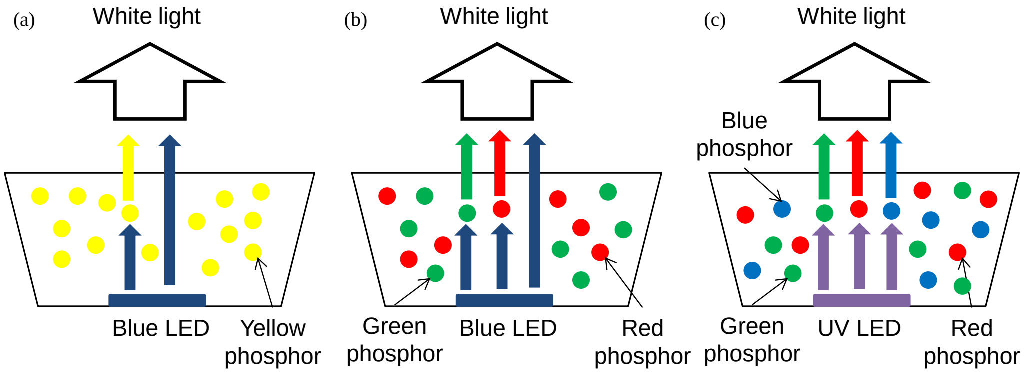

Figure 1-2. Representative methods of generating white light from LEDs: blue LED + yellow phosphor (a), blue LED + green and red phosphors (b), and UV-LED + RGB phosphors (c).

1.1.4 Plasma Display Panel (PDP)

Rare earth phosphors are used for Plasma Display Panel (PDP). Mainly, phosphors by excitation of vacuum ultra violet (VUV) are used. Figure 1-3 shows an illustration of AC drive system of PDP. Electricity is discharged by applying a voltage to inter-electrode. Mixture gases of Xe-He are excited by this electricity charge. VUV is generated by excitation of Xe-Ne. Phosphors emit light by excitation of VUV. Red, green, and blue emitted by excitation of VUV are irradiated from the phosphors to the outside through glass. Phosphors for PDP require next points. 1. Excitation band is UVU range. 2. Surface defects are as few as possible and luminance and luminous efficiency are high. 3. Persistence is high in VUV. 4. An afterglow is suitable to display an image. 5. Color purity of the emission is high. 6. Degradation by a heating process is few in the manufacture of the panels. 7. Manufacturing cost is cheap.

Below are some examples that are used as PDP phosphors. In the present, $BaMgAl_{10}O_{17}$:Eu, Zn_2SiO_4:Mn, and $(Y,Gd)BO_3$:Eu is used as blue, green, and red phosphors, respectively [32, 38, 39].

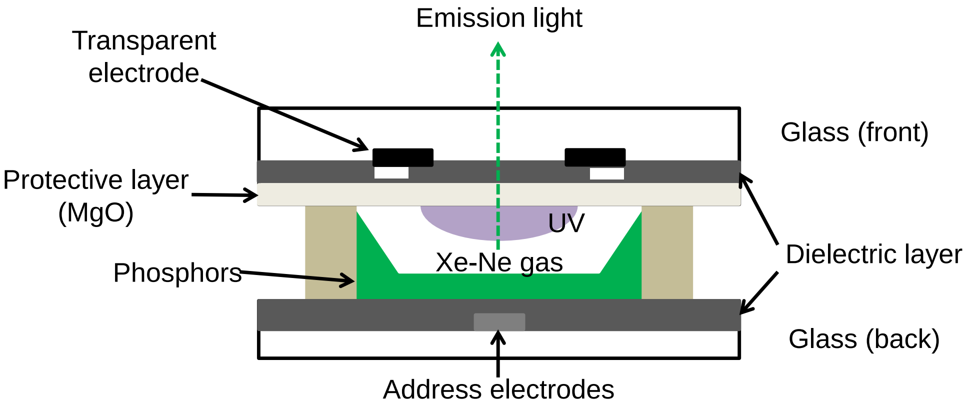

Figure 1-3. An illustration of AC drive system of PDP.

1.1.5 Solar cell [40]

The energy can be semi permanently used by a solar cell. A solar cell is a competent device that does not emit greenhouse gas, such as a CO_2 by the power generation. Silicon is used for more than 90 % of the prevailing solar cells now. Energy conversion efficiency of the solar cells is high (25 %). In terms of the cost and reliability, Si solar cells are widely used. Electron-hole pairs are generated by irradiation with light of energy more than band gap of Si ($E_g = 1.12$ eV). The Si solar cells generated electricity from the electron-hole pairs. That is, the conversion efficiency is high in the wavelength near Eg. Mainly, solar cells have spectral sensitivity between 400 and 1100 nm. Even if Si solar cells are supplied with photons that have much higher energy than Eg, such as ultra violet, extra energy is lost as the heat. On the other hand, in the wavelength of the low energy, such as an infrared light, Si solar cells cannot be generated electricity, because of not reaching energy of band gap. In current stage, conversion efficiency is limited by mismatch between solar spectral and band gap. Theoretical limits of conversion efficiency reach 30 % by Shockley-Queisser limit [41]. If ultraviolet and infrared are effectively utilized for solar cells, they can generate electricity over theoretical limits. As a one of the plan, spectral convert layers using phosphors are considered. (Figure 1-4)

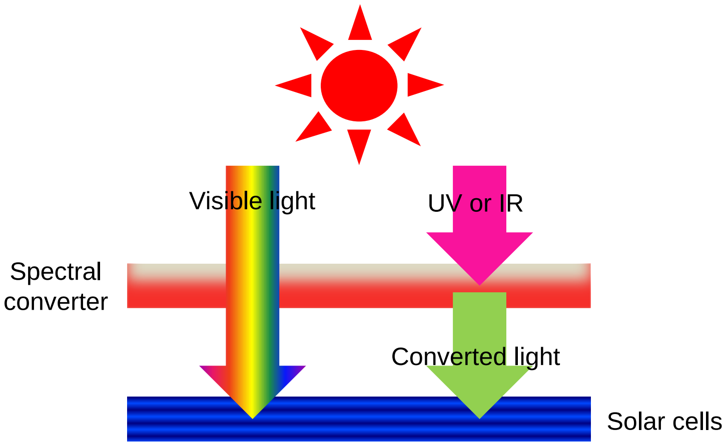

Figure 1-4. An illustration of spectral converter.

Spectral converter is classified into three types. (a) Down shift: One photon of high energy converts one photon of low energy [42-43]. (b) Down conversion (quantum cutting): One photon of high energy converts two photons of low energy [44]. (c) Up conversion: Two photons of low energy convert one photon of high energy [45]. (Figure 1-5)

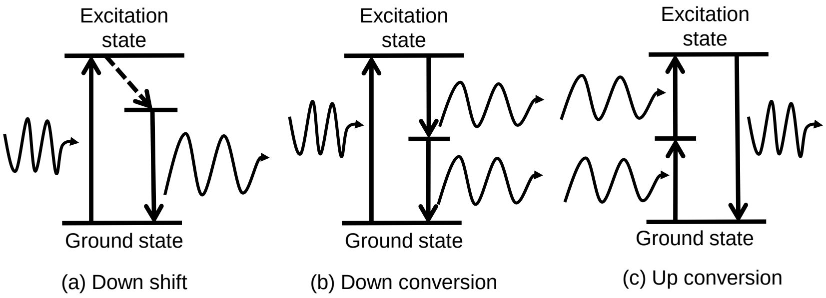

Figure 1-5. An illustration of the energy band in spectral converter.

1.1.6 Scintillation [46]

Scintillation phosphors are materials emitted by excitation of X-ray and γ-ray. Scintillation phosphors are used for a radiation detector and a medical diagnosis, such as X-ray photograph, computed tomography (CT), and positron emission tomography (PET).In the field of a medical diagnosis, scintillation phosphors are emitted by X-ray. The emission is used as image. In the field of a radiation detector, two types are classified. One is a thermoluminescence dosimeter (TLD). Scintillation phosphors irradiated with radiations absorb a partition of the energy. Electrons and holes are excited in the crystal of scintillation phosphors. Electron is semi-stable state by capturing in the lattice defects. When scintillation phosphors are heats in this state, they back to stable states by recombining the captured electrons and the trapped holes. Scintillation phosphors are emitted by this recombination. Other is a scintillation counter. Photo-multipliers receive light emitted by irradiation with radiations. Concentration of radioactive substance from the total amount of the radiations and radiation spectra from intensity of the emission pulse are measured.

Scintillation phosphors require next points. 1. Luminous efficiency is high toward radiations. 2. Absorption coefficient is high toward radiations. 4. An afterglow of scintillation phosphors is short. 5. It is difficult that scintillation phosphors are degraded by irradiation of radiations.

1.2 Upconversion phosphors [47]

Upconversion phosphors are introduced in this section A general phosphor has characteristics that emission wavelength is longer than excitation wavelength, called as Stokes shift. On the other hand, upconversion phosphors has characteristics that emission wavelength is shorter than excitation wave length, called as anti-Stokes shift. In 1966, upconversion mechanisms were advocated by F. Auzel [47]. This upconversion phosphor has been often researched by various researchers. In this section, characteristics of the upconversion phosphors are introduced.

1.2.1 Excited state absorption (ESA) and energy transfer upconversion (ETU)

In order to realize that rare earth doped materials effectively up-convert photon energy, it is important to choice activators and sensitizers and excitation wavelength. Even if combination of activators and sensitizers is same, the optical properties are difference by the concentration, host materials, and excitation wavelength. However basic luminescence processes are interpreted by absorption of light, radiative and non-radiative relaxation, and energy transformation.

The reason why upconversion phenomenon is distinct in rare earth doped phosphors is an excited state absorption (ESA). This phenomenon happen because rare earth ion excited to intermediate state, excited to higher state by absorbing another photon. For example, rare earth materials, such as Er^{3+} that have many intermediate states are observed. (Figure 1-6(a)) After that, in Yb^{3+} doped materials, a sensitizing effect is observed. Absorption wavelength of Yb^{3+} is around 1000 nm. Yb^{3+} has high absorption cross section. High concentration of Yb^{3+} (20 ~ 30 mol%) can be doped due to be difficult to self-quenching. Life of the excitation state is comparatively long. Yb^{3+} can be emitted by transferring energy to another rare earth element. Luminous efficiency can be remarkably enhanced by combining sensitizers (Yb^{3+}) and activators that have emission light in the visible region (Er^{3+} and Tm^{3+}). Upconversion by energy transformation of these processes is called as an energy transfer upconversion (ETU). (Figure 1-6(b))

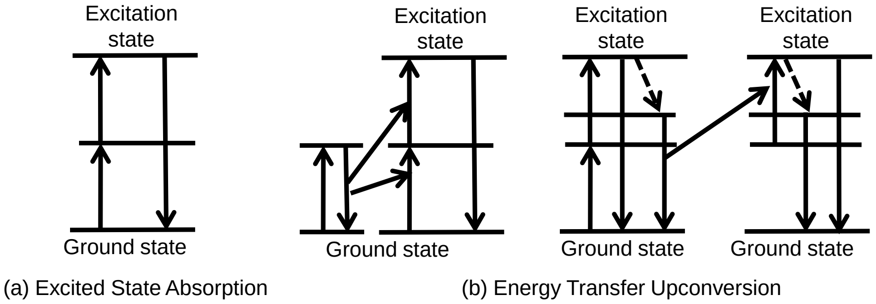

Figure 1-6. An illustration of ESA and ETU.

Upconversion phosphors emit light by absorbing multi-step photon. In a general, they emit light by absorbing two or three photons. In upconversion phosphors, relationships between emission intensity and excitation power are given as follow:

$$I_{em} \propto P_{ex}^{\;n} \tag{1-1}$$

where I_{em} denotes the emission intensity; P_{ex}, the excitation power of a laser diode; and *n*; the number of photons. If upconversion phosphors emit light by absorbing two photons, the number of photons is 2. If they emit light by three photon absorption, the number of photons is 3. It is found that upconversion phosphors emit light depending on excitation power.

Upconversion processes observed the most recently are photon avalanche effects. In 1979, they are observed by J. S. Chivian et al. When upconversion processes, such as ETU and ESA of Pr^{3+}-doped $LaCl_3$ and $LaBr_3$, are investigated, it is found that intensity of upconversion emission is dramatically increased. When dramatic increase of the emission intensity happens, it is found that transmission of $LaCl_3$:Pr is dramatically deceased by Reference 48. This effect is attributed to increase of the population of excitation state by cross relaxation section. That is, because of increasing the population in intermediate state of rare earth, the emission intensity is remarkably increased (Figure 1-7). This phenomenon is called as a photon avalanche effect. This effect is observed in many rare earth phosphors, such as Sm^{3+}, Nd^{3+}, Tm^{3+}, and Er^{3+} [49-52].

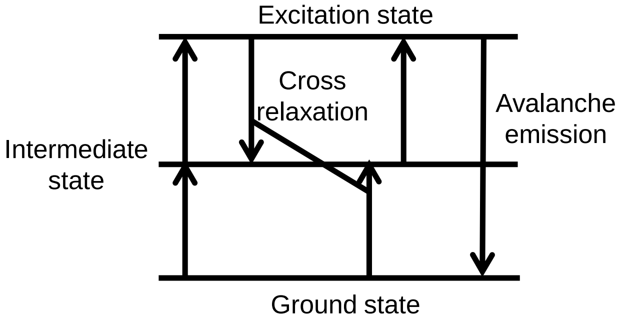

Figure 1-7. Simplified energy scheme for the avalanche mechanism.

1.2.2 Host materials

For the phosphors, host materials are significant substances. Also, various host materials are used for upconversion phosphors. Host materials, such as Y_2O_3, $NaYF_4$, and YVO_4 are used. Luminous efficiency is difference by the vibration of host materials. Thermal relaxation of excitation state in 4f orbital of rare earth can be controlled by the vibration of host materials. Thermal relaxation is that excitation state energy of the rare earth ion is transmitted to host materials as thermal vibration. The thermal relaxation is called as multi phonon relaxation because multiple vibrations are excited. If binding energy between host materials is low when the rare earth ions relax thermally, thermal relaxation rate is low because more phonon energy must be excited. In general, thermal relaxation rate *w* (s^{-1}) is given as follow:

$$w \propto \exp\left(-k \frac{\Delta E}{h\nu_{\max}}\right) \tag{1-2}$$

where ΔE (J) is energy difference between 4f excitation state and state under it, k (-) is constant, $h\nu_{max}$ (J) is phonon vibration of host materials [53]. Figure 1-8 shows thermal relaxation rate as a function of phonon energy of host materials. $NaYF_4$ as host material is often used for upconversion phosphors. Because $NaYF_4$ is lower phonon energy than other host materials, it is often researched as materials that emit effectively light. Y_2O_3 used in this study is chemically stable and can be applied for various fields. The phonon energy of host materials is around 350 cm^{-1} and 550 cm^{-1}, in $NaYF_4$ and Y_2O_3, respectively [53-54].

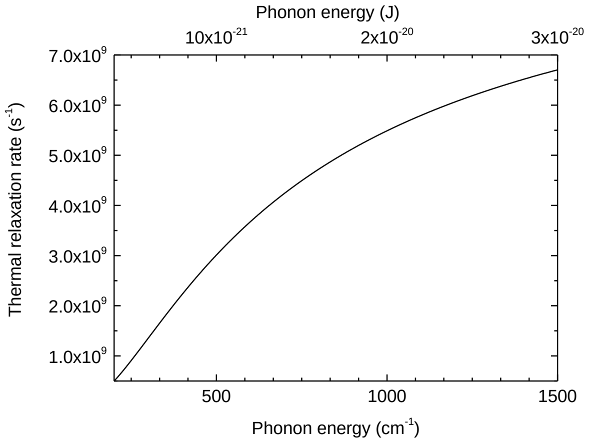

Figure 1-8. Thermal relaxation rate as a function of phonon energy of host materials.

・Crystal structure [56]

Y_2O_3, $NaYF_4$, and YVO_4 that regard yttrium as three valences of cation are used for host materials of the rare earth doped phosphors. Ionic radius of Y^{3+} is close to that of the other rare earth. Also, chemical properties of Y^{3+} are similar to those of the other rare earth. So, three valences rare earth ion can be doped in these host materials.

In this study, Y_2O_3 is introduced because of using Er-Yb-doped Y_2O_3. Rare earth doped Y_2O_3 has been often used as displays and illuminations because of a highly stable material. Y_2O_3:Eu [57] and Y_2O_3:Tb [58] have been often researched. Figure 1-9 shows a crystal structure of Y_2O_3. A crystal structure of Y_2O_3 is called as *I*a3: C-type structure. The basic crystal structure is a body center cubic (BCC) structure that a, b, and c axis are 10.604 Å, respectively. Six oxygen atoms are combined with a yttrium atom. Also, three oxygen atoms are combined with two yttrium atoms. In the rare earth phosphors, rare earth enter Y^{3+} site.

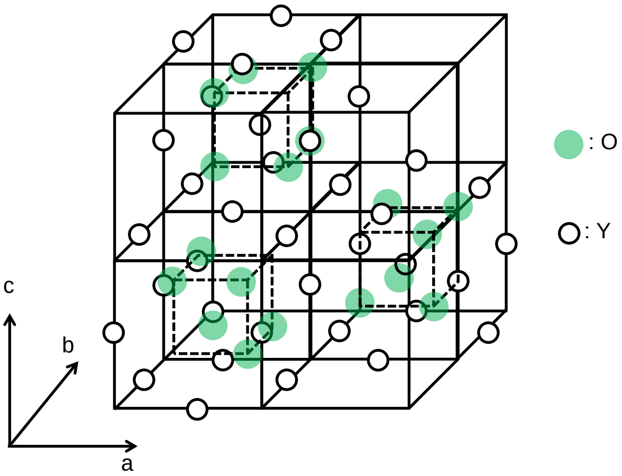

Figure 1-9. *I*a3: C-type Y_2O_3 structure.

1.2.3 Activators and sensitizers [46, 58]

Rare earth ions that emit upconversion luminescence are various. There are Pr, Ho, Er, and Tm as the representative rare earths. Emission and excitation wavelength are different by energy bands of 4f orbital in rare earth. Figure 1-10 shows energy diagrams of the representative rare earths that emit upconversion luminescence. These energy diagrams are advocated by G. H. Dieke et al [59]. These are energy diagrams of 4f orbital in rare earth, when each rare earth is doped in $LnCl_3$ as a host material. These energy diagrams have been considered in not only $LnCl_3$ but also various host materials.

Letters written next to orbitals are term symbols. In the case of a kind of lanthanide, because 4f orbital is inside $5s^2 5p^6$ orbital, many physical properties, such as magnetic moment etc, depend on f orbitals. Summation of orbital angular momentum (li) in electrons of the 4f orbital is regarded as L. Summation of spin angular momentum (si) is regarded as S. In the case of heavy element, such as a lanthanide, because spin orbital coupling cannot be ignored, total angular momentum J is $J = L - S$ less than 7 electrons in 4f orbital and $J = L + S$ more than 7 electrons in 4f orbital (Russell-Saunders coupling). Split of energy state in one atom depends on repulsion between the electrons or spin orbital coupling. Therefore, electronic state regarding transition state in f orbital can be understood in more detail by using term symbols $^{2S+1}L_J$. For example, in the case of Er^{3+}, it has an electronic configuration of $4f^{11}$. In the ground state, when spin orbital momentum S is 3/2, orbital angular momentum L is 6 and total angular momentum J is 15/2. In the ground state, a term symbol of Er^{3+} is expressed as $^4I_{15/2}$.

Yb^{3+} mainly works as not an activator but a sensitizer. Because energy band of Yb^{3+} is around 1000 nm, Yb^{3+} absorbs and radiate near infrared. By doping Yb^{3+} with other rare earth ion, energy transfer happens. As a result, Yb^{3+} stimulates upconversion luminescence. In this study, Er-Yb-codoped Y_2O_3 is used as upconversion phosphors. Table 1-1 shows upconversion phosphor materials.

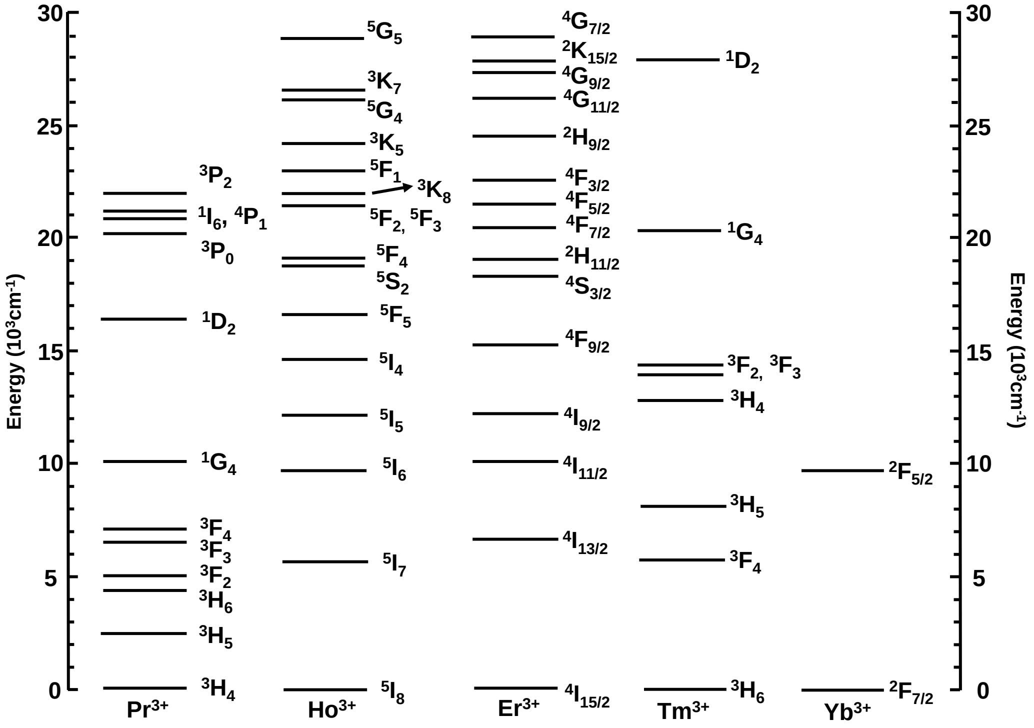

Figure 1-10. Energy level diagrams of representative rare earths ion that emits upconversion luminescence.

Table 1-1. Materials that emit upconversion luminescence.

Materials	Emission wavelength (λ_{em})	Excitation wavelength (λ_{ex})	Reference
Y_2O_3:Er,Yb	535, 670 nm	978 nm	60
Y_2O_3:Tm,Yb	478, 490 nm	976 nm	61
Y_2O_3:Ho,Yb	420, 429, 490, 550, 668 nm	978 nm	62
Y_2O_3:Pr,Yb	457, 486, 510, 550 nm	976 nm	63
$NaYF_4$:Er,Yb	517, 536, 651 nm	980 nm	18
$NaYF_4$:Tm,Yb	475, 650 nm	975 nm	64
$NaYF_4$:Ho,Yb	542, 645 nm	980 nm	65
$NaYF_4$:Pr,Yb	482, 522, 606, 688 nm	980 nm	66
YVO_4:Er,Yb	525, 550, 660 nm	970 nm	67
Y_2O_2S:Er,Yb	410, 492, 534, 555, 672 nm	980 nm	68
$LaPO_4$:Er,Yb	550, 675 nm	980 nm	69
$BaTiO_3$:Er,Yb	523, 548, 656 nm	980 nm	70

1.2.4 Upconversion luminescent process [47].

In this subsection, upconversion luminescent process in Y_2O_3:Er,Yb is introduced. When excitation light uses 980 nm NIR, I show luminescent process. It is found that Y_2O_3:Er,Yb emits three colors of the red (660 nm), green (550 and 540 nm), and blue (410 nm).

First, the red emission ($^2F_{9/2} \rightarrow {}^4I_{15/2}$) is considered. By the excitation of 980 nm NIR, $^2F_{7/2} \rightarrow {}^2F_{5/2}$ of Yb and $^4I_{15/2} \rightarrow {}^4I_{11/2}$ of Er are excited. The energy transfer to Er happened because of the relaxation of Yb. Then, non-radiative relaxation of $^4I_{11/2} \rightarrow {}^4I_{13/2}$ occurs in Er. $^4I_{13/2} \rightarrow {}^4F_{9/2}$ of Er is excited by 980 nm NIR and the energy transfer of Yb. Thereafter, the red emission happens by backing to the ground state ($^2F_{9/2} \rightarrow {}^4I_{15/2}$).

Second, the green emission ($^2H_{11/2}/{}^4S_{3/2} \rightarrow {}^4I_{15/2}$) is considered. By the excitation of 980 nm NIR, $^4I_{15/2} \rightarrow {}^4I_{11/2}$ of Er is excited. $^4I_{11/2} \rightarrow {}^4F_{7/2}$ of Er is excited by 980 nm NIR and the energy transfer of Yb. The non-radiative relaxation of $^4F_{7/2} \rightarrow {}^2H_{11/2}$ and $^4F_{7/2} \rightarrow {}^4S_{3/2}$ in Er occurs. Then, the green emission occurs due to backing to the ground state ($^2H_{11/2}/{}^4S_{3/2} \rightarrow {}^4I_{15/2}$).

Finally, the blue emission ($^2H_{9/2} \rightarrow {}^4I_{15/2}$) has two routes. One goes through the red emission. By the excitation of 980 nm NIR, the state of the red emission is excited. $^4S_{3/2} \rightarrow {}^4K_{15/2}$ of Er is excited by 980 nm NIR and the energy transfer of Yb. Thereafter, the blue emission happens by backing to the ground state ($^2H_{9/2} \rightarrow {}^4I_{15/2}$). The other goes through the green emission. $^4S_{3/2} \rightarrow {}^4K_{15/2}$ of Er is excited by 980 nm NIR and the energy transfer of Yb. The non-radiative relaxation of $^4K_{15/2} \rightarrow {}^2H_{9/2}$ in Er occurs. Thereafter, the blue emission happens by backing to the ground state ($^2H_{9/2} \rightarrow {}^4I_{15/2}$).

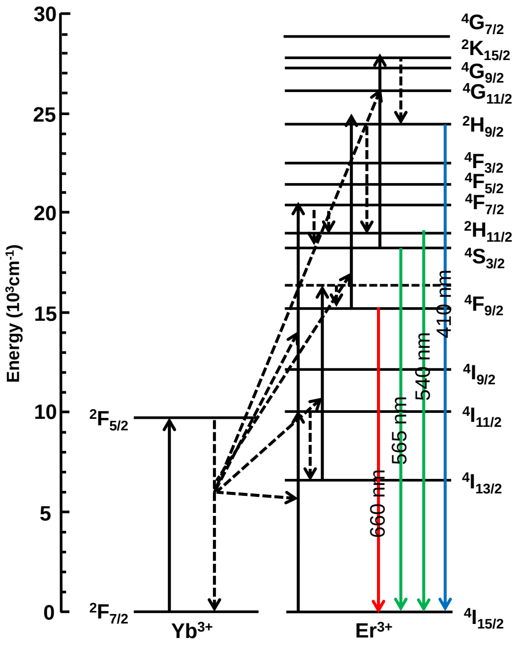

Figure 1-11. Energy-level diagrams of Er^{3+} and Yb^{3+} in Y_2O_3 by the excitation of 980 nm NIR.

1.3 Optical properties and general preparation of nano-phosphors

Inorganic nano-materials that differ from inorganic materials of the bulk attract much attention because of having unique optical properties. Metal nanoparticles, such as gold and silver, have unique absorption wavelength in visible range by surface plasmon resonance [71-72]. In semiconductor nanoparticles, band gap is increased by depending on the particle size, and the absorption wavelength shift to shorter wavelength [73]. From the optical properties, it is expected that the nanoparticles are applied for solar cells [74] and bio-imaging [1]. In Dope-type nano-phosphors, in 1994, R. N. Bhargava et al. reported that when modified surface of $ZnS:Mn^{2+}$ nano-phosphors by using organic materials, luminous efficiency is increased with decreasing particle size [75]. In this section, optical properties and general preparation of nano-phosphors are introduced.

1.3.1 Optical properties of nano-phosphors

It is known that nanoparticles of metal and inorganic materials have various effects on optical properties and catalytic activity, compared to bulk materials. In this subsection, effect on optical properties by size reduction of nanometer order level will be introduced.

A. Surface defects

Specific surface area of the particle is increased with decreasing the particle size. The surface defects are increased with increasing the specific surface area. The excited electron is captured by surface defect state. Luminous efficiency of nano-phosphors is decreased by non-radiative relaxation. To solve this problem, researches are carried out that surface defect states disappear, such as silica covered core/shell particles [76] and particles modified with organic materials [77]. These researches prevent nanoparticles from decreasing luminous efficiency by surface defect states.

B. Quantum size effects [78]

When the particle size of the semiconductors is reduced up to a few nano-meter sizes, valence and conduction band is narrow by discrete energy levels. As a result, band gap is increased. A characteristic blue shift of absorption wavelength in the semiconductor nanoparticles appears. That is, emission wavelength is varied by controlling a size of semiconductor nanoparticles. (Figure 1-12)

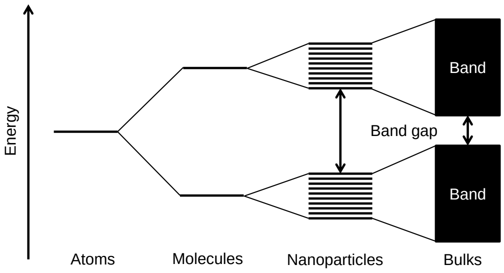

Figure 1-12. An illustration of relationship between material size and electronic energy.

C. Scattering

It is found that scattering of excitation light can be decreased by reducing particle size up to 1/10 of visible wavelength. This phenomenon can be described by Rayleigh scattering. The scattering intensity I_s (-) is given by:

$$I_s = I_0 \frac{\pi^4 d^6}{8\lambda^4 R^2}\left(\frac{n^2-1}{n^2+2}\right)^2\left(1+\cos^2\theta\right) \tag{1-3}$$

where I_0 (-) is incident light, d (m) is particle size, λ (m) is light of wavelength, R (m) is the distance to the particle, n (-) is the refractive index of the particle, and θ (°) is the scattering angle. From this formula, the scattering intensity is compared to the sixth power of particle size, and is affected by the particle size. Scattering light can be prevented by reduction of the particle size. So, there is a prospect of increase of the luminous efficiency. (Figure 1-13)

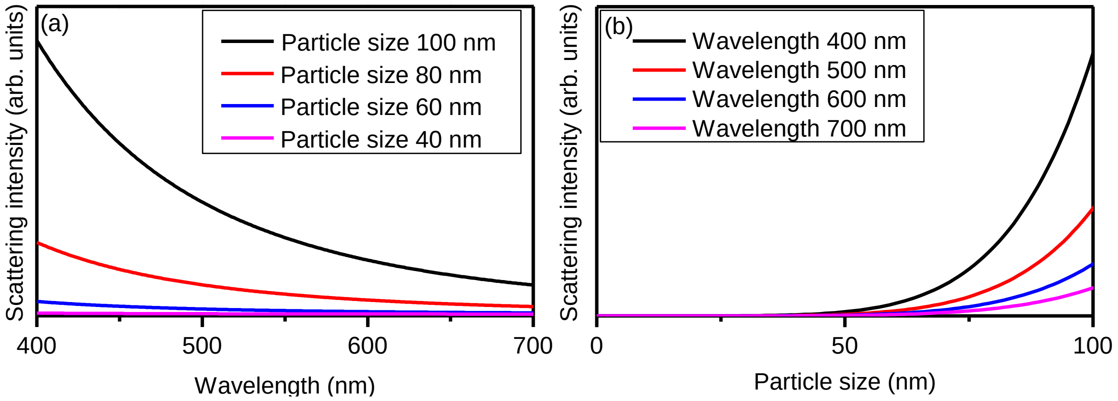

Figure 1-13. The scattering intensity I_s as a function of the wavelength λ (a) and the particle size d (b).

1.3.2 Preparation of nano-phosphors

Preparation methods of nanoparticles are various [78]. In general, preparation methods of nanoparticles are classified as bottom-up and top-down method. As bottom-up methods, chemical reaction syntheses are widely used. As top-down methods, nanoparticles are prepared by using laser irradiation and gas phase deposition. In this subsection, bottom-up methods are introduced mainly.

A. Reverse micelle method [79]

When a little of water is added into organic solvent dissolved a surfactant, reverse micelles are generated by facing outside hydrophobic groups and inside hydrophilic groups. Reverse micelle method is method synthesized nanoparticles by using chemical reaction field of the droplet in reverse micelle called as “water pool”. Because of using the restricted reaction field, the prepared nanoparticles are prevented from aggregating each other. Also, particle size is controlled by size of “water pool”. Sodium bis(2-ethylhexyl)sulfosuccinate (AOT) and heptane are used as surfactant and organic solvent, respectively.

B. Hydrothermal synthesis [80]

Hydrothermal synthesis is a method synthesizing inorganic materials under water vapor of high pressure. High temperature and pressure is prepared by heating closed containers, called as autoclave, including water and starting materials. Because the vapor pressure is extremely high, and water structures in a high temperature are different from those in a room temperature, inorganic materials are easy to be dissolved into water. The inorganic materials are generated by crystalizing from the solution. High quality nanoparticles can be prepared because, in the high temperature, the properties of solubility and reactivity in organic materials are changed. Mono-dispersed nanoparticles can be prepared by adjusting pressure, temperature, and reaction time. Also, a method reacted in nonpolar solvent is called as a solvothermal synthesis [81].

C. Polymerized complex method [82]

Polymerized complex method is method preparing inorganic materials that distribute uniformly dopants by carrying out a polymerization reaction of the plural metal complexes. By dissolving plural metal salts into the solution of citric acid and propylene glycol, citric acid complexes of the metal are synthesized. Instead of the citric acid, a malic acid is used for the synthesis. Ester polymerization reaction is accelerated by heating the glycol solution into which citric acid complexes of the metal dissolve. As the polymerization reaction proceeds, viscosity of the solution is increased. Polyester resin that metallic ions are uniformly distributed in is synthesized. After that, precursors are synthesized by the pyrolysis reaction.

D. Spray pyrolysis method [83]

Spray pyrolysis method is a representative process converting droplets into particles. This method proceeds to applications of the industrialization because heating and reaction time is a few seconds, and fine particles can be continuously prepared. The preparation methods are as follows. Droplets are prepared by spraying raw material solution that metallic salts are dissolved into. By carrier gas, the droplets directly enter a high temperature field such a reaction furnace. In the reaction furnace, one solvent in the droplets evaporates, and the other raw materials in the droplets are solid particles by the pyrolysis reaction.

1.4 Laser ablation

Laser ablation is a process that etches a solid surface. When a solid is irradiated with laser of the intensity exceeding a threshold, electronic, thermal, photochemical, and dynamic energy is converted on the solid surface. As a result, neutral atoms, molecules, zwitter-ion, radical, cluster, electron, and photon are explosively discharged. This technology pays attention because of top-down preparation of nanoparticles.

1.4.1 Laser ablation in gas phase

In the gas phase, laser ablation has been widely used for preparation of nano-clusters and thin films. This technology is used for Si nano-cluster [84] and C, such as fullerene [85] and carbon nanotube (CNT) [86]. Si nano-clusters are expected to apply optoelectronics. In the thin films, on the other hand, pulsed laser deposition (PLD) is used for thin films of the superconductive oxide and ferroelectric materials, such as $YBa_2Cu_3O_{7-x}$ [87] and $Pb(Zr,Ti)O_3$ [88] respectively.

In the laser ablation in gas phase, a general mechanism is introduced. In the low energy density of the pulsed laser, the temperature on surface of the targets is rapidly increased by laser irradiation. However, no transient melting temperature is reached. Targets are cooled by heat conductivity of themselves. Although targets don’t reach molten state, a local change including atom ejections is observed (Figure 1-14 (a)). In the middle energy density of the pulsed laser, molten layers are generated by laser irradiation (Figure 1-14 (b)). When amorphous Si is irradiated with a pulsed laser, a part of the amorphous Si is crystalized [89]. This is a phenomenon called as a laser anneal. In the high energy density of the pulsed laser, electrons and atoms from the targets surface are explosively ejected. The photo-electrons ejected from the molten layers obtain kinetic energy by electric field of laser. This is called as an inverse bremsstrahlung. After that, atoms are ionized by electrons and atoms colliding. After these process, plasma called as “plume plasma” is generated. In the higher energy density of the pulsed laser, the temperature of the plasma plume is high. High excitation plasma is generated by excitation of the core electrons (Figure 1-14 (c)).

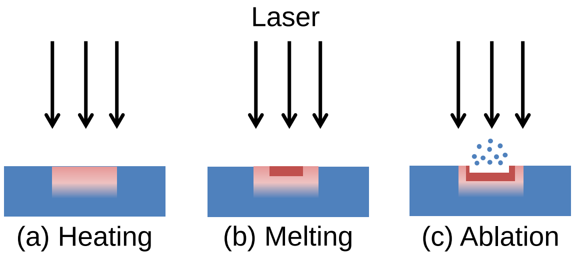

Figure 1-14. Heating (a), melting (b), and ablation (c) by irradiation with a pulse laser.

1.4.2 Laser ablation in liquid

Laser ablation in liquid is a method preparing the nanoparticles by irradiating a solid surface with a laser in solution (Figure 1-15). In 1993, T. Cotton et al. prepared the nanoparticles by irradiating materials, such as gold, silver, platinum, and copper, with a laser in liquid [90]. In 2000, F. Mafuné et al. prepared gold nanoparticles in surfactants by this technology. Since then, the nanoparticles of the various materials, such as organic materials [91] and ceramics [91], are prepared by this technology. Also, various solutions including water, such as surfactants, polymers, and super critical fluid, are used in this technology [93-96]. In this subsection, a general mechanism of laser ablation in liquid is introduced.

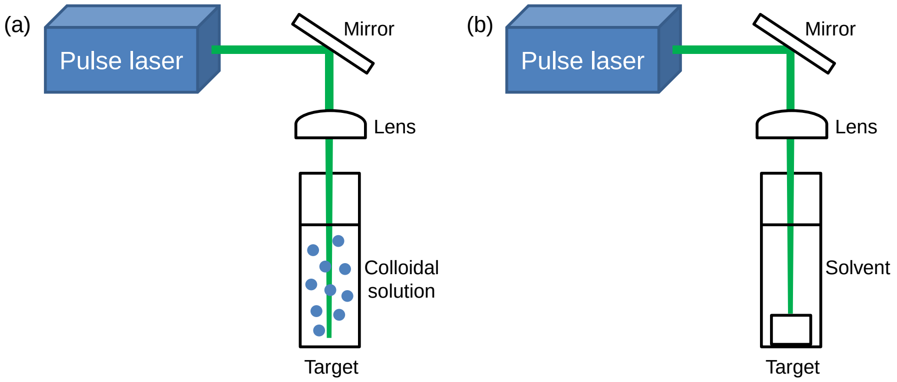

Figure 1-15. An illustration of laser ablation in colloidal solution (a) and laser ablation in liquid by using target plate.

A. Laser ablation in colloidal solution

・Laser melting in liquid [97]

As a new method preparing sphere particles, there is laser melting in liquid. This technology is developed by N. Koshizaki et al. This is a method preparing sphere particles by irradiating colloidal solution with non-focus laser of low fluence. In general, nano-second laser of the low intensity is used. Thus far, ceramics materials, such as B_4C, ZnO, CuO, and Fe_2O_3 have been reported. Figure 1-16 (a) shows a mechanism of Laser melting in liquid. Particles are melted by irradiating aggregated particles with a low fluence laser. The melted particles form spherical particles by the surface energy between solvent and the particles. After that, the particles are quenched and solidified by solvent. The particle size is increased by the repetition of the process.

- Coulomb explosion [98]

One of the size reduction mechanisms by laser ablation in colloidal solution is a coulomb explosion. This phenomenon happens by irradiating the colloidal solution with a focus laser. The target materials have an electric charge by electron ejection of the laser irradiation. This is a phenomenon that the size reduction of particle happens by coulomb repulsion. This phenomenon is called as a fragmentation. This phenomenon is known to happen by using a laser from nano to pico second. (Figure 1-16 (b))

- Photo-thermal process[99]

One of the size reduction mechanisms is a photo-thermal process. This is a phenomenon that happens by irradiating the colloidal solution with a focus laser, as well as coulomb explosion. Surface of the particles is vaporized by laser irradiation. After that, this is a phenomenon that prepares fine nanoparticles by quenching the solvent. This phenomenon is known to happen by using a laser from pico to femto second. (Figure 1-16 (c))

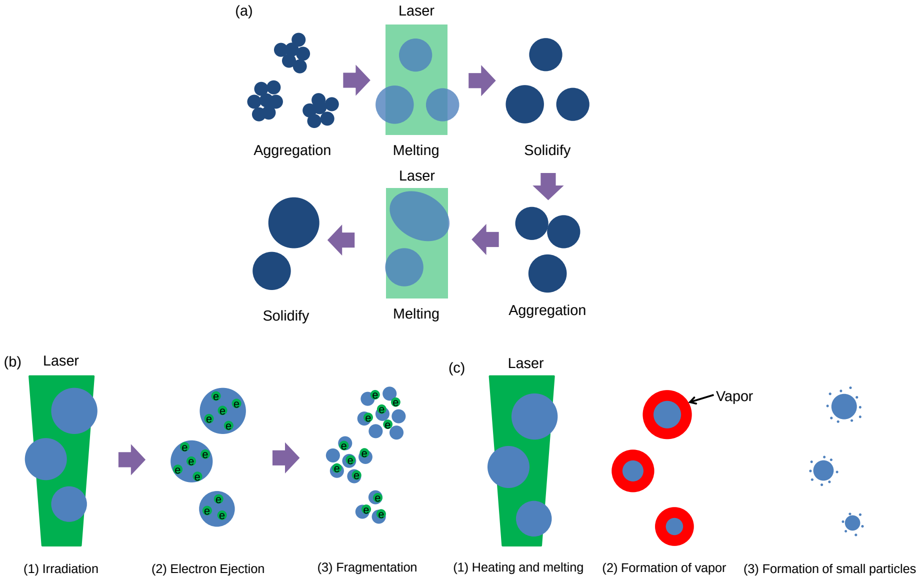

Figure 1-16. An illustration of laser melting in liquid (a), coulomb explosion process (b), and photo-thermal process (c).

B. Laser ablation in liquid by using target plate.

- General mechanism [100]

This technology is used for various materials, such as gold, silver, and ceramics. A general mechanism of laser ablation in liquid by using target plate is introduced. Irradiating the targets with a pulsed laser, a plume plasma is generated in about 0.001-0.1 ns. This plume plasma is materials including atoms, molecules, electrons, clusters, and radical. As a counter reaction of the plume plasma, a shock wave is generated. High pressure is generated by the shock wave. Temperature, pressure, and density in the plume plasma are of the order of 10^3K, 10^9-10^{10}Pa, 10^{22-23} atoms/cm^3, respectively. In a time of about 0.1 ns after irradiation, the plume plasma expands, and is quenched by the surrounding solution. The energy of the plume plasma is released to the surrounding solution. Then, the surrounding solution is heated up to temperatures of the plume plasma with degradation, ionization, and pyrolysis of solution molecules. In a time of 10-100 ns after irradiation, the plume plasma is extinguished. The energy of the plume plasma released to the surrounding solution is induced the rise of the cavitation bubble in the time scale of 0.1-1 μs. The expansion of the cavitation bubble goes on up to time of the order of 100 μs. As the bubble expands, the temperature is decreased. When the bubble collapses, the high energy is used for the rise of a shock wave. Temperature and pressure in bubble's collapse are the same order of the plasma plume (order of 10^3 K, 10^9-10^{10} Pa). After the time scale of 100 μs, particles are generated. Then, surface modifications and oxidation of the nanoparticles happen by reacting with solution molecules.

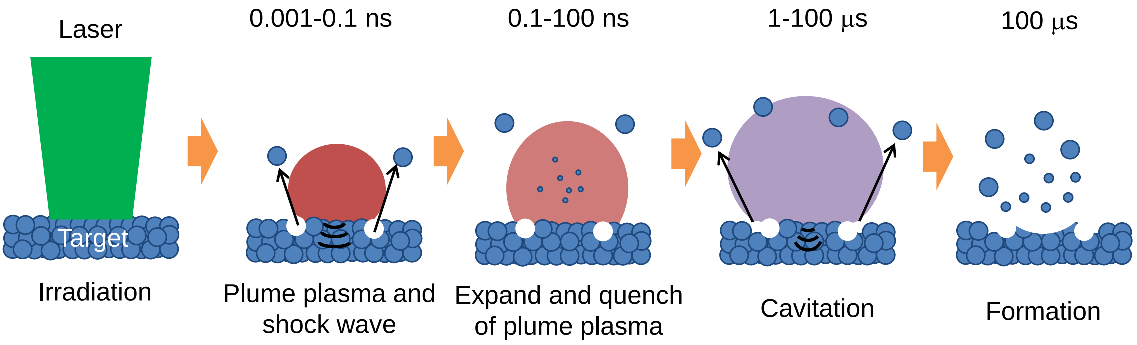

Figure 1-17. General mechanism of laser ablation in liquid by using target plate.

- Pressure generated by laser ablation in liquid [101-104]

Irradiating a pulsed laser in the confined solution, it has been found that high pressure is generated from a shock wave raised by counter reaction of the plume plasma. Fabbro et al. developed to measure experimentally the pressure. The pressure *P* (GPa) raised by laser ablation in liquid is given by the following function:

$$P(GPa) = 0.01\sqrt{\frac{\alpha}{\alpha+3}}\sqrt{Z\left(g\cdot cm^{-2}s^{-1}\right)}\sqrt{I_0\left(GW\cdot cm^{-2}\right)} \tag{1-4}$$

where α (-) is the fraction of the internal energy devoted to thermal energy (typically α≈0.25), I_0 (GW/cm^{-2}) is an incident power intensity, and Z (gcm^{-2}s^{-1}) is the shock impedance between the target and the confined solution. The shock impedance Z is given by the following function:

$$\frac{2}{Z} = \frac{1}{Z_{solution}} + \frac{1}{Z_{target}} \tag{1-5}$$

where $Z_{solution}$ (g·cm^{-2}s^{-1}) and Z_{target} (g·cm^{-2}s^{-1}) are the shock impedances of the solution and the target. For examples, the shock impedance of water, aluminum, and silicon is 0.165×10^6 g·cm^{-2}s^{-1}, 1.5×10^6 g·cm^{-2}s^{-1}, and 2.1×10^6 g·cm^{-2}s^{-1} respectively.

・Temperature by laser ablation in liquid

For laser ablation in liquid, there is temperature as one of the important parameter. After irradiating a target with a laser, temperature can be calculated by observing emission spectra of the ejection. From the emission spectra, Swan band of vibrational transitions can be read. Rotational band of the molecules can be read by measuring the Swan band at high resolution. Temperature can be calculated by analysis of the rotational lines assuming Boltzmann distribution [104]. In the case of Nd:YAG laser (pulse width: 20 ns, pulsed energy:70 mJ, and wavelength: 1064 nm), temperature about 5600 K is obtained [106]. Also, in the case of observation of black body spectra, temperature can be decided by comparing to Plank's formula. Also, from the pressure calculated from shock impedance, volume estimated from the emission images, and amount of the ejection from size of irradiation mark temperature can be calculated by using an ideal gas law.

1.5 Objective of this study

As explained in prior sections, it is known that Y_2O_3:Er,Yb has upconversion properties. The materials are expected to be applied in the wide range between devices and biomaterials. The nanoparticles have been often prepared by chemical reaction methods. In general, sintering process is carried out in chemical reaction methods. But, because crystallinity of the nanoparticles is low in low temperature sintering, luminous efficiency of the phosphor nanoparticles is low. On the other hand, in high temperature sintering, the phosphor nanoparticles are aggregated by necking process. Also, it is significant that activators are uniformly distributed in the preparation of the nanoparticles. Therefore, laser ablation in liquid is expected to prepare the nanoparticle. It is technology that the nanoparticles are prepared by irradiating the laser in solution. However, it is hardly reported that upconversion nanoparticles are prepared by laser ablation in liquid. In this study, Y_2O_3:Er,Yb nanoparticles were prepared by laser ablation in liquid.

This study has been performed in three objectives. First, preparation mechanism of laser ablation in liquid is comprehended. It is difficult that laser ablation in liquid controls the morphology and size distribution of nanoparticles. Preparation mechanism of laser ablation has not been clear. Therefore, it is significant to comprehend preparation mechanism of laser ablation in liquid. One of the objectives is to model preparation mechanism of the ceramics nanoparticles prepared by laser ablation in liquid. Preparation mechanism was considered from the morphology and size distribution of nanoparticles.

Secondly, crystallinity of nanoparticles is significant for nano-phosphor. Amorphous nano-phosphors degrade luminous efficiency. Also, heterogeneous distribution of the dopant in host materials causes self-quenching, which degrades luminous efficiency. Therefore, these parameters have an influence in the optical properties of nanoparticles. One of the objectives is to prepare highly-crystalline nanoparticles that dopants are uniformly distributed in, and to investigate crystallinity and distribution of the dopant in the prepared nanoparticles.

Finally, it is significant to know optical properties of upconversion nanoparticle. Upconversion nanoparticles are used for various applications, such as bio-imaging, PDT, and spectral converter for solar cell. One of the objectives is to investigate the optical properties of Y_2O_3:Er,Yb nanoparticles prepared by laser ablation in liquid.

1.6 References

[1] M. Bruchez, M. Moronne, P. Gin, S. Weiss, and A. P. Alivisato, *Science* 281 (1998) 2013-2015.

[2] S. T. Selvan, T. T-Y Tan, D. K. Yi, and N. R. Jana, *Langmuir* 26 (2010) 11631-11641.

[3] R. Mahtab, H. H. Harden, and C. J. Murphy, *Journal of American Chemical Society* 122 (2000) 14-17.

[4] J. Lović, H. S. Bazzi, Y. Cuie, G. R-A. Fortin, F. M. Winnik, and D. Maysinger, *Journal of Molecular Medicine* 83 (2005) 377-385.

[5] M. S. Patterson, B. C. Wilson, and D. R. Wyman, *Lasers in Medical Science* 6 (1991) 379-390.

[6] H. Kobayashi, N. Kosaka, M. Ogawa, N. Y. Morgan, P. D. Smith, C. B. Murray, X. Ye, J. Collins, G. A. Kumar, H. Bell, and P. L. Choyke, *Journal of Materials Chemistry* 19 (2009) 6481-6484.

[7] N. Billinton and A. W. Knight, *Analytical Biochemistry* 291 (2001) 175-197

[8] J. R. Mansfield, K. W. Gossage, C. C. Hoyt, and R. M. Levenson, *Journal of Biomedical Optics* 10 (2005) 041207 1-9.

[9] M. Yu, F. Li, Z. Chen, H. Hu, C. Zhan, H. Yang, and C. Huang, *Analytical Chemistry* 81 (2009) 930-935.

[10] A. Schädlich, H. Caysa, T. Mueller, F. Tenambergen, C. Rose, A. Göpferich, J. Kuntsche, and K. Mäder, *ACS NANO* 5 (2011) 8710-8720

[11] H. Maeda, *Bioconjugate Chemistry* 21 (2010) 797

[12] Y. Matsumura and H. Maeda, *Cancer Research* 46 (1986) 6387-6392.

[13] J. Zhou, Z. Liu, and F. Li, *Chemical Society Reviews* 41 (2012) 1323-1349.

[14] M. Kimimura, D. Miyamoato, Y. Saito, K. Soga, and Y. Nagasaki, *Langmuir* 24 (2008) 8864-8870

[15] T. Zako, H. Hyodo, K. Kosuke, K. Tokuzen, H. Kishimoto, M. Ito, K. Kaneko, M. Maeda, and K. Soga, *Journal of Nanomaterials* 491471 (2010) 1-7.

[16] G. K. Das and T. T. Yang Tan, *Journal of Physical Chemistry C* 112 (2008) 11211-11217.

[17] L-Q. Xiong, Z-G. Chen, M-X. Yu, F-Y. Li, C. Liu, and C-H. Huang, *Biomaterials* 30 (2009) 5592-5600.

[18] G. Yi, H. Lu, S. Zhao, Y. Ge, W. Yang, D. Chen, and L-H. Guo, *Nano Letters* 4 (2011) 2191-2196.

[19] M. Wang, C. Mi, Y. Zhang, J. Liu, F. Li, C. Mao, and S. Xu, *Journal of Physical Chemistry C* 113 (2011) 19021-19027.

[20] L. Xiong, Z. Chang, Q. Tian, T. Cao, C. Xu, and F. Li, *Analytical Chemistry* 81 (2009)

8687-8694.

[21] Q. Liu, Y. Sun, C. Li, J. Zhou, C. Li, T. Yang, X. Zhang, T. Yi, D. Wu, and F. Li, *ACS Nano* 5 (2011) 3146-3157.

[22] J. Ueda, H. Tsutsui, H. Honda, S. Ichinose, T. Ishizumi, T. Hirata, T. Inoue, K. Ohtani, S. Maehara, K. Imai, Y. Tsunoda, M. Kubota, N. Ikeda, K. Furukawa, T. Okunoda, and H. Kato, *Lung Cancer* 58 (2007) 317-323.

[23] C. J. Lightdale, S. K. Heier, N. E. Marcon, J. S. McCaughan, H. Gerdes, Be. F. Overholt, M. V. Sivak, G. V. Stiegmann, and H. R. Nava, *Gastrointernational Endoscopy* 42 (1995) 507-512.

[24] H. Kato, K. Furukawa, M. Sato, T. Okunaka, Y. Kusunoki, M. Kawahara, M. Fukuoka, T. Miyazawa, T. Yana, K. Matsui, T. Shiraishi, and H. Horinouchi, *Lung Cancer* 42 (2003) 103-111.

[25] H. S. Qian, H. C. Guo, P. C-L. Ho, R. Mahendran, and Y. Zhang, *Small* 5 (2009) 2285-2290.

[26] N. M. Idris, M. K. Gnanasammandhan, J. Zhang, P. C. Ho, R. Mahendran, and Y. Zhang, *Nature Medicine* 18 (2012) 1580-1586.

[27] C. Wang, H. Tao, L. Cheng, and Z. Liu, *Biomaterials* 32 (2011) 6145-6154.

[28] S. Ye, F. Xiao, Y. X. Pan, Y. Y. Ma, and Q. Y. Zhang, *Materials Science and Engineering R* 71 (2010) 1-34.

[29] Y. Pan, M. Wu, and Q. Su *Journal of Physics and Chemistry of Solid* 65 (2004) 845-850.

[30] N. Hirosaki, R-J. Xie, K. Kimoto, T. Sekiguchi, Y. Yamamoto, T. Suehiro, and M. Mitomo, *Applied Physics Letters* 86 (2005) 211905 1-3.

[31] J. K. Sheu, S. J. Chang, C. H. Kuo, Y. K. Su, L. W. Wu, Y. C. Lin, W. C. Lai, J. M. Tsai, G. C. Chi, and R. K. Wu, *IEEE PhotonicsTechnology Letters* 15 (2003) 18-20.

[32] K. B. Kim, Y. I. Kim, H. G. Chun, T. Y. Cho, J. S. Jung, and J. G. Kang, *Chemistry of Materials* 14 (2002) 5045-5052.

[33] H. D. Ngyuen, I. H. Yeo, and S. I. Mho, *ECS Transaction* 28 (2010) 167-173.

[34] Y. H. Song, B. S. Kim, M. K. Jung, K. Senthil, T. Masaki, K. Toda, and D. H. Yoon, *Journal of The Electrochemical Society* 159 (2012) J148-J152.

[35] X. Q. Piao, K. Machida, T. Horikawa, H. Hanzawa, Y. Shimomura, and N. Kijima. *Chemistry of Materials* 19 (2007) 4592-4599.

[36] L. W. Yang, H. L. Han, Y. Y. Zhang, and J. X. Zhong, *Journal of Physical Chemistry C* 113 (2009) 18995-18999.

[37] X. Hou, S. Zhou, T. Jia, H. Lin, and H. Teng, *Journal of Alloys and Compounds* 509 (2011) 2793-2796.

[38] C. Barthou, J. Benoit, P. Benalloul, and A. Morell, *Journal of The Electrochemical Society* 141 (1994) 524-528.

[39] Z. G. Wei, L.D. Sun, C. S. Liao, C. S. Liao, X. C. Jiang, and C. H. Yan, *Journal of Materials Chemistry* 12 (2002) 3665-3670. (Y,Gd)BO_3:Eu

[40] B. M. Ende, L. Aarts, and A. Meijerink, *Physical Chemistry Chemical Physics* 11 (2009) 11081-11095.

[41] W. Schockley and H. J. Queisser, *Journal of Applied Physics* 32 (1961) 510-519.

[42] S. Ye, B. Zhu, J. Luo, Y. Teng, J. Chen, G. Lakshminarayana, G. Qian and J. Qiu, *Applied Physics Letters* 93 (2008) 181110 1-4.

[43] Y. Iso, S. Takeshita, and T. Isobe, *Journal of The Electrochemical Society* 159 (2012) J72-J76

[44] R. T. Wegh, H. Donker, K. D. Oskam, and A. Meijerink, *Science* 283 (1999) 663-666.

[45] J. L. Ferrari, K. O. Lima, E. Pecoraro, R. A. S. Ferreira, L. D. Carlos, and R. R. Gonçalves, *Journal of Materials Chemistry* 22 (2012) 9901-9908.

[46] W. M. Yen, S. Shionoya, H. Yamamoto (Eds.), *Phosphor Handbook* CRC Press, Boca Raton, FL (2006).

[47] F. Auzel, *Chemical Reviews* 104 (2004) 139-173.

[48] J. S. Chivian, W. E. Case, and D. D. Eden, 35 (1979) 124-125.

[49] N. J. Krasutsky, *Journal of Applied Physics* 54 (1983) 1261-1267.

[50] U. Oetliker, M. J. Riley, P. S. May, and H. U. Güdel, *Journal of Luminescence* 53 (1992) 553-556.

[51] H. Ni, and S. C. Rand, *Optics Letters* 17 (1992) 1222-1224.

[52] Y. Onodera, T. Nunokawa. O. Odawara, and H. Wada, *Transactions of the Materials Research Society of Japan* 38 (2013) 317-320.

[53] L. A. Riseberg and H. W. Moos, *Physical Review* 174 (1968) 429-438.

[54] F. Wang and X. G. Liu, *Chemical Society Reviews* 38 (2009) 976-989.

[55] A. Ambrosini, A. Duarte, and K. R. Poeppelmeier, *Journal of Solid State Chemistry* 153 (2000) 41-47.

[56] Y. C. Kang, H. S. Roh, and S. B. Park, *Advanced Materials* 12 (2000) 451-453.

[57] Y. Zin, J. Guo, T. White, T. T. Yang Tan, and R. Xu, *Journal of Physical Chemistry C* 111 (2007) 7893-7897.

[58] P. W. Atkins (Eds) *Physical Chemistry* Six edition Oxford University Press (1998).

[59] G. H. Dieke and H. M. Crosswhite, *Applied Optics* 2 (1963) 675–686.

[60] F. Vetrone, J. C. Boyer, J. A. Capobianco, A. Speghini, and M. Bettinelli, *Journal of Applied Physics* 96 (2004) 661-667

[61] Q. Lü, F. Y. Guo, L. Sun, A. H. Li, and L. C. Zhao, *Journal of Applied Physics* 103 (2008) 123533.

[62] V. Lojpur, M. Nikolić, L. Mančić, O. Milošević, M.D. Dramićanin, *Optical Materials* 35 (2012) 38-44.

[63] C. B. Zheng, Y. Q. Xia, F. Qin, Y. Yu, J. P. Miao, Z. G. Zhang, and W. W. Cao, *Chemical Physics Letters* 496 (2010) 316-320.

[64] W. J. Kim, M. Nyk, and P. N. Prasad, *Nanotechnology* 20 (2009) 185301.

[65] J. Shan, X. Qin, N. Yao, and Y. Ju, *Nanotechnology* 18 (2007) 445607.

[66] X. P. Chen, X. Y. Huang, and Q. Y. Zhang, *Journal of Applied Physics* 106 (2009) 063518.

[67] G. Mialon, S. Türkcan, G. Dantelle, D. P. Collins, M. Hadjipanayi, R. A. Taylor, T. Gacoin, A. Alexandrou, and J. P. Level, *Journal of Physical Chemistry C* 114 (2010) 22449-22454.

[68] G. A. Kumara, M. Pokhrel, A. Martinez, R.C. Dennis, I.L. Villegas, and D.K. Sardar, *Journal of Alloy and Compounds* 513 (2012) 559-565.

[69] P. Ghosh, J. Oliva, E. D. Rosa, K. K. Haldar, D. Solis, and A. Patra, *Journal of Physical Chemistry C* 112 (2008) 9650-9658.

[70] J. Hao, Y. Zhang, and X. Wei, *Angewandte Chemie International Edition* 50 (2011) 6876-6880.

[71] J. Hodak, I. Martini, and G. V. Hartland, *Chemical Physical Letters* 284 (1998) 135-141.

[72] T. R. Jensen, M. L. Duval, K. L. Kelly, A. A. Lazarides, G. C. Schatz, and R. P. Duyne, *Journal of Physical Chemistry B* 103 (1999) 9846-9853.

[73] L. E. Brus, *Journal of Chemical Physics* 80 (1984) 4403-4409.

[74] P. Chewchinda, T. Tsuge, H. Funakubo, O. Odawara, and H. Wada, *Japanese Journal of Applied Physics* 52 (2013) 025001.

[75] R. N. Bhargava, D. Gallagher, X. Hong, and A. Nurmikko, *Physical Review Letters* 72 (1994) 416-419.

[76] Z. Li and Y. Zhang, *Angewandte Chemie International Edition* 118 (2006) 7896-7899.

[77] H. Takahashi and T. Isobe, *Japanese Journal of Applied Physics* 44 (2005) 922-925.

[78] B. L Cushing, V. L. Kolesnichenko, and C. J. O Connor, *Chemical Reviews* 104 (2004) 3893-3946.

[79] T. Hirai, Y. Asada, and I. Komasawa, *Journal of Colloid and Interface Science* 276 (2004) 339-345.

[80] G. Z. Ren, S. J. Zeng, and J. H. Hao, *Journal of Physical Chemistry C* 115 (2011) 20141-20147.

[81] M. R. Davolos, S. Feliciano, A. M. Pires, R. F-C. Marques, and M. Jafelicci, *Journal of Solid State Chemistry* 171 (2003) 268-272.

[82] H. Meyssamy, K. Riwotzki, A. Kornowski, S. Naused, and M. Haasse, *Advanced Materials* 11 (1999) 840-844.

[83] A. Purwanto, I. W. Lenggoro, H. Chang, and K. Okuyama, *Journal of Chemical Engineering of Japan* 39 (2006) 68-76.

[84] T. Makimura, Y. Kunii, N. Ono, and K. Murakami, *Japanese Journal of Applied Physics* 35 (1996) L1703-L1705.

[85] H. W. Kroto, J. R. Heath, S. C. O'Brien, R. F. Curl, and R. E. Smalley, *Nature* 318 (1985) 162-163.

[86] T. Guo, P. Nikolaev, A. G. Rinzler, D. Tománek, D. T. Colbert, and R. E. Smalley, *Journal of Physical Chemistry* 99 (1995) 10694-10697.

[87] G. Koren, A. Gupta, R. J. Baseman, M. I. Lutwyche, and R. B. Laibowitz, *Applied Physics Letters* 55 (1989) 2450-2452.

[88] J. F. M. Cillessen, M. W. J. Prins, and R. M. Wolf, *Journal of Applied Physics* 81 (1997) 2777-2783.

[89] M. O. Thompson, G. J. Galvin, J. W. Mayer, P. S. Peercy, J. M. Poate, D. C. Jacobson, A. G. Cullis, and N. G. Chew, *Physical Review Letters* 52 (1983) 2360-2363.

[90] J. Neddersen, G. Chumanov, and T. M. Cotton, *Rapid Communication* 47 (1993) 1959-1964.

[91] F. Mafuné, J. Kohno, Y. Takeda, T. Kondow, and H. Sawabe, *Journal of Physical Chemistry B* 104 (2000) 9111-9117.

[92] Y. Hosokawa, M. Yashiro, T. Asahi, H. Fukumura, and H. Masuhara, *Applied Surface Science* 154-155 (2000) 192-195.

[93] W. T. Nichol, T. Kodaira, Y. Sasaki, Y. Shimizu, T. Sasaki, and N. Koshizaki, *Journal of Physical Chemistry B* 110 (2006) 83-89.

[94] F. Mafuné, J. Kohno, Y. Takeda, T. Kondow, and H. Sawabe, *Journal of Physical Chemistry B* 105 (2001) 5114-5120.

[95] M. Cueto, M. Sanz, M. Oujja, F. Gámez, B. Martínez-Haya, and M. Castillejo, *Journal of Physical Chemistry C* 115 (2011) 22217-22224.

[96] K. Saitow, T. Yamamura, and T. Minami, *Journal of Physical Chemistry C* 112 (2008) 18340-18349.

[97] H. Q. Wang, A. Pyatenko, K. Kawaguchi, X. Y. Li, Z. Swiatkowska-Warkocka, and N. Koshizaki, *Angewandte Chemie International Edition* 49 (2010) 6361-6364.

[98] S. Inasawa, M. Sugiyama, and Y. Yamaguchi, *Journal of Physical Chemistry B* 109 (2005) 9404-9410.

[99] P. V. Kamat, M. Flumiani, and G. V. Hartland, *Journal of Physical Chemistry B* 102 (1998)

3123-3128.

[100] V. Amendola, and M. Menghetti, *Physical Chemistry Chemical Physics* 15 (2013) 3027-3046.

[101] R. Fabbro, J. Fournier, P. Ballard, D. Devaux, and J. Virmot, *Journal of Applied Physics* 68 (1990) 775-784.

[102] L. Berthe, R. Fabbro, P. Peyre, L. Tollier, and E. Bartnicki, *Journal of Applied Physics* 82 (1997) 2826-2832.

[103] L. Berthe, R. Fabbro, P. Peyre, and E. Bartnicki, *Journal of Applied Physics* 85 (1999) 7552-7555.

[104] L. Berthe, A. Sollier, P. Peyre, R. Fabbro, and E. Bartnicki, *Journal of Physics D: Applied Physics* 33 (2000) 2142-2145.

[105] T. Sakka, S. Iwanaga, Y. H. Ogata, A. Matsunawa, and T. Takemoto, *Journal of Chemical Physics* 112 (2000) 8645-8653.

[106] K. Saito, T. Sakka, and Y. H. Ogata, *Journal of Applied Physics* 94 (2003) 5530-5536.

Chapter 2 Experimental and characterization

2.1 Preparation of target

Table 2-1 shows purity, molecular mass, and makers of reagents for prepared target. Preparation of the target referred [1]. $Y(NO_3)_3 \cdot 6H_2O$ (99.99% Kanto Chemical Co., Inc.), $Er(NO_3)_3 \cdot 5H_2O$ (99.9% Mitsuwa's Pure Chemicals), $Yb(NO_3)_3 \cdot nH_2O$ (99.9% Wako Pure Chemical Industries, Ltd.), and aqueous ammonia (28% Kanto Chemical Co., Inc.) were used as starting materials. $Y(NO_3)_3 \cdot 6H_2O$ (11.1 mmol), $Er(NO_3)_3 \cdot 5H_2O$ (0.125 mmol) and $Yb(NO_3)_3 \cdot nH_2O$ (1.25 mmol) (I calculated as n=5) were completely dissolved in deionized water. Aqueous ammonia (11 mL) was added dropwise to this solution. The prepared solution was aged for 24 h. The precipitations were dried at 900 °C for 2 h. The dried powder was pressed into shapes and sintered at 1250 °C for 4 h. The targets were 9 mm in diameter and 3 mm in height. Figure 2-1 shows a target picture (a) and a SEM image of the surface (b). Figure 2-2 shows an experimental flow chart for the synthesis of the Y_2O_3:Er,Yb target.

Table 2-1. Start materials for preparation of the target.

Reagents	Purity (%)	molecular mass (g/mol)	Makers
$Y(NO_3)_3 \cdot 6H_2O$	99.99 %	383.01	Kanto Chemical Co., Inc.
$Er(NO_3)_3 \cdot 5H_2O$	99.9 %	443.35	Mitsuwa's Pure Chemicals
$Yb(NO_3)_3 \cdot nH_2O$	99.9 %	359.05 (Without Hydrate)	Wako Pure Chemical Industries, Ltd.
NH_4OH	28%	35.04	Kanto Chemical Co., Inc.

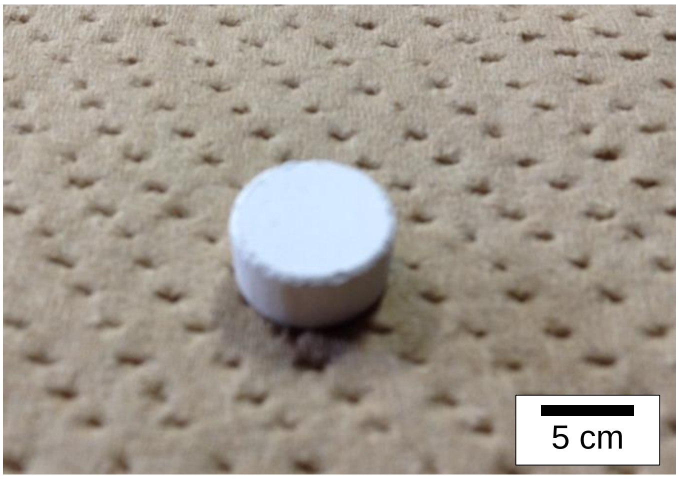

Figure 2-1. Picture of An target.

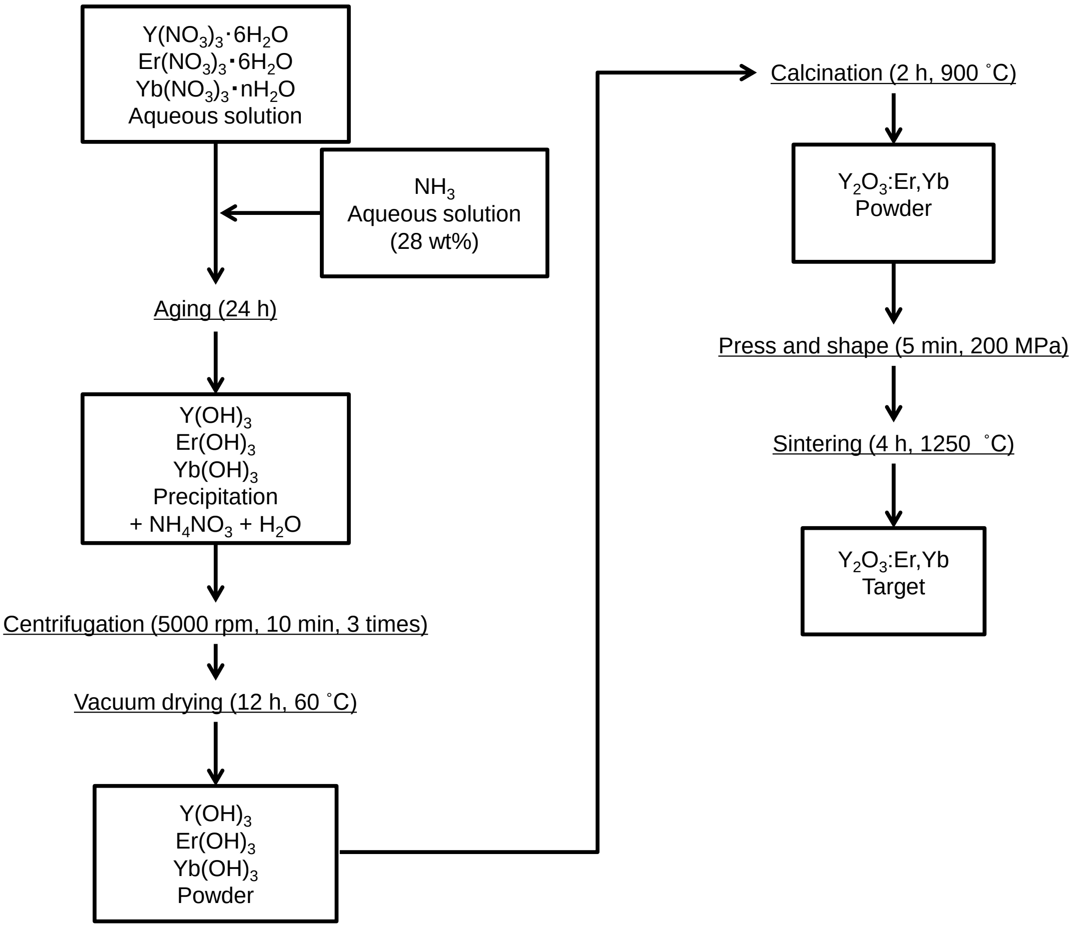

Figure 2-2. Experimental flow chart for the synthesis of the Y_2O_3:Er,Yb target using sol-gel method.

2.2 Laser ablation in liquid

The Y_2O_3:Er,Yb nanoparticles were prepared by laser ablation in liquid. The target was placed on the bottom of the cell that was filled with 2 ml of deionized water. The Nd:YAG laser (Spectron Laser Systems Ltd., SL8585G) served as a light source for pulsed laser ablation and was operated with the second harmonic generation (wavelength: 532 nm) at a laser energy of repetition rate of 10 Hz. When an alignment paper (Laser Create Corp) was irradiated with laser, the average energy density was calculated from the spot size per pulse and the power of the laser. The pulse width was 13 ns when measured with a fast PIN photodiode and a digital oscilloscope. Figure 2-3 shows an illustration of the laser equipment. Conditions of laser ablation in liquid in the preparation of the dot-like nanoparticles were as follows: laser fluence 1.38 J/cm^2 and irradiation time: 15 min. Conditions of laser ablation in liquid in the preparation of the nano-strings were as follows: laser fluence = 1.38 J/cm^2 and irradiation time = 30 min.

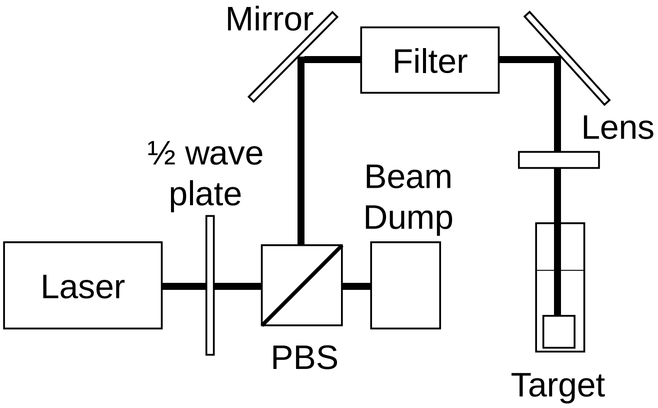

Figure 2-3. An illustration of the laser equipment.

2.3 Crystallinity evaluation

X-ray diffractometer (XRD, PANalytical X'pert-PRO-MRD) was used for crystallinity evaluation of the materials. At the X-ray resource, Cu K_{α} was used. In the normal measurement, X-ray tube voltage and X-ray tube voltage was 40 kV and 30 mA, respectively. The normal samples were measured on the scan range: 10–70°, scan speed: 1.000°/min, and step width: 0.02°.

2.4 Morphology and size distribution

The morphology and dispersibility of the primary particles was observed by scanning electron microscopy (SEM, Hitachi High-Technologies Co. S-4800), transmission electron microscopy (TEM, JEOL Ltd. JEM-1010BS or Hitachi High-Technologies Co. H-8100), and scanning transmission electron microscopy (STEM, JEOL Ltd. JEM-2100F). The colloidal solution 2 μl of Y_2O_3:Er,Yb was placed onto the elastic carbon supporting film (Okenshoji Co., Ltd.). A powder of the Y_2O_3:Er,Yb targets was placed on a microscope stage. After that, the samples were observed. In SEM observation, I carried out as follow conditions; main accelerating voltage was 5 kV, and main magnifications were 100 and 200 K. In TEM and STEM observation, I carried out as follow conditions; main accelerating voltage was 200 kV, and main magnifications were from 150 k to 1 M.

The average particle size and dispersibility of the secondary particle was measured by dynamic light scattering (DLS, Sysmex Co. Zetasizer Nano). The laser source of the DLS was a He-Ne laser (633 nm). A cuvette cell, which the prepared colloidal solution entered, was set on DLS equipment. The average particle size was calculated by the scattering intensity of the fluctuation, which is dependent on the Brownian motion of the particle. Measurement temperature was used as 25 °C. As refractive index of Y_2O_3:Er,Yb, refractive index of Y_2O_3 was used as 1.93 in 25 °C. Refractive index and viscosity of H_2O in 25 °C were used as 1.330 and 0.8872, respectively.

2.5 Composition analysis

A scanning transmission electron microscopy energy dispersive X-ray spectroscopy (STEM-EDX, JEOL Ltd. JEM-2100F) and an inductively coupled plasma mass spectroscopy (ICP-MS, PerkinElmer Japan Co. Ltd. ELAN DRC-e) were used for the composition analysis. At the STEM-EDX measurement, the colloidal solution 2 μl of Y_2O_3:Er,Yb was placed onto the elastic carbon supporting film as well as TEM and SEM. After that, the samples were measured.

At the ICP-MS measurement, the samples dissolved in HNO_3 aqua of 15 ml (1M, Kanto Chemical Co., Inc) were used. The prepared colloidal solution was dried on a vacuum dryer or a rotary evaporator. After that, the dried powder was dissolved in HNO_3 aqua. If the powder could not be dissolved, it was put in ultrasonic device at 55 °C.

2.6 Optical properties

Optical properties were measured by fluorescent spectrophotometer (Hitachi High-Technologies Co. F-7000). At the optical properties of a target, grated target in the solid folder was measured. At the optical properties of the nanoparticles, dried nanoparticles were measured. As an experimental procedure, the colloidal solution was dropped on a slide glass. The slide glass was dried. The slide glass, which nanoparticles were attached, was covered with a quartz glass. At the optical properties of the colloidal solution, the solution in a quartz cell was measured. In measurement of fluorescent spectrophotometer, I carried out as follow conditions. Range of the measured fluorescent wavelength was from 400 to 700 nm (visible region). Voltage of photo multiplier was 700 V. Slit width was 1 or 5 nm.

2.7 Single level nanoparticle spectroscopy

Spectra of the upconversion nanoparticles in single level were measured. Single level nanoparticle spectroscopy was measured at the method used by T. Asahi et al. [2-6]. The prepared colloid solution was dropped on a slide glass. The slide glass was dried. The excitation light used a femtosecond laser (Spectra Physics, Tsunami, wavelength: 793 nm, Pulse width: 100 fs, repetition rate: 80 MHz). The laser was irradiated through objective lens. The beam size was 0.8 μm. Figure 2-4 shows the illustration of single level nanoparticle spectroscopy.

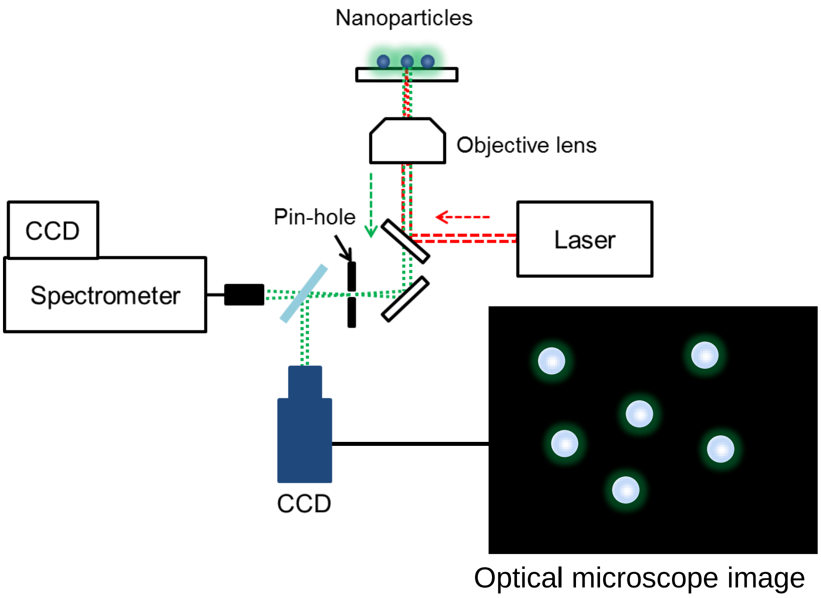

Figure 2-4. An illustration of single level nanoparticle spectroscopy

2.8 References

[1] B. Y. Kokuoz, K. Serivalsatit, B. Kokuoz, O. Geiculescu, E. McCormick, and J. Ballato, *Journal of American Ceramics Society* 92 (2009) 2247–2253.

[2] T. Itoh, T. Asahi, and H. Matsuhara, *Applied Physics Letters* 79 (2001) 1667-1669.

[3] T. Asahi, T. Sugiyama, and H. Matsuhara, *Account of Chemical Research* 49 (2008) 1790-1798.

[4] R. Yasukuni, G. Laurent, K. Okazaki, M. Oki, T. Torimoto, and T. Asahi, *Journal of Photochemistry and Photobiology A: Chemistry* 221 (2011) 194-198.

Chapter 3 Morphology of Y_2O_3:Er,Yb nanoparticles

3.1 Introduction

Upconversion fluorescent materials have attracted much attention because of their unique optical properties and potential applications in the field of bio-imaging, color displays, and wave length shifter of solar cell [1-3]. The upconversion fluorescent materials are substances that emit visible light by irradiating near infrared as an exciting light [4]. Articles on the upconversion fluorescent properties of rare-earth doped Y_2O_3 have been reported. Er^{3+} as activator functions as the upconversion fluorescent materials [5]. Because Yb^{3+} absorb near infrared at 980 nm ($^2F_{5/2} \rightarrow {}^2F_{7/2}$), it is often used as an effective sensitizer [6]. In particular, Y_2O_3 as a host material has the same crystal structure as Er_2O_3 and Yb_2O_3 [7-9]. Y_2O_3 includes a comparatively high refractive index, low phonon energy, and high chemical and thermal stability.

Although upconversion nanoparticles have been prepared by various wet chemical synthesis, laser ablation in liquid is focused on. This technology is for preparing the nanoparticles by irradiating the targets with a pulsed laser beam in liquid [10]. Also, it is hardly reported that upconversion nanoparticles are prepared by laser ablation in liquid. As general mechanism, when a pulsed laser is irradiated on target in the solution, a plume plasma is generated on the surface of target [11]. The plume plasma generates high temperature and high pressure. Nanoparticles are generated by quench of the plume plasma. Also, shock wave is generated by counteraction of the plume plasma. A fragmentation of target occurs by high pressure of the shock wave. The energy of the plume plasma released to the surrounding solution generates a cavitation bubble. Also, the cavitation bubble generates high temperature and high pressure. The cavitation bubble is involved to the preparation of nanoparticles.

Laser ablation in liquid has many advantages. The nanoparticles are formed easily. The nanoparticles are collected with high efficiency, compared with preparation in the gas phase. Pure colloidal solutions can be prepared, depending on the surrounding solution. Also, laser ablation in liquid has some disadvantages. Although it is reported that nanoparticles of gram order scale can be prepared by laser ablation in liquid [12], productivity of the prepared nanoparticles is still far from achievement of the other method like wet chemical synthesis. As the reason, laser is scattered by cavitation bubble generated on the target surface. It is difficult to controlled size distribution of the prepared nanoparticles [13]. It is difficult to control size shape of the prepared nanoparticles [14].

In this chapter, a Y_2O_3:Er,Yb nanoparticles were prepared by changing laser fluence and irradiation time. As a result, nanoparticles of the various shapes were observed. The morphology of the particle prepared by laser ablation in liquid was investigated. Investigation of the particle morphology is lead to elucidate mechanisms of laser ablation in liquid. From mechanisms that have been proposed so far, the prepared nanoparticles formation process was considered.

3.2 Experimental

3.2.1 Preparation of the target

$Y(NO_3)_3 \cdot 6H_2O$ (99.99% Kanto Chemical Co., Inc.), $Er(NO_3)_3 \cdot 5H_2O$ (99.9% Mitsuwa's Pure Chemicals), $Yb(NO_3)_3 \cdot 5H_2O$ (99.9% Wako Pure Chemical Industries, Ltd.), and aqueous ammonia (28% Kanto Chemical Co., Inc.) were used as starting materials. $Y(NO_3)_3 \cdot 6H_2O$ (11.1 mmol), $Er(NO_3)_3 \cdot 5H_2O$ (0.125 mmol) and $Yb(NO_3)_3 \cdot nH_2O$ (1.25 mmol) were completely dissolved with deionized water. Aqueous ammonia (11 mL) was added dropwise to this solution. The prepared solution was aged for 24 h. The precipitations were dried at 900 °C for 2 h. The dried powder was pressed into shapes and sintered at 1250 °C for 4 h. The targets were 9 mm in diameter and 3 mm in height.

An overview of the synthesis scheme is given by the following reaction steps:

$$RE(NO_3)_3 + 3NH_4OH \rightarrow RE(OH)_3 + 3NH_4NO_3 \qquad (3\text{-}1)$$

$$2RE(OH)_3 \xrightarrow{900\ ^\circ C} RE_2O_3 + 3H_2O \qquad (3\text{-}2)$$

where RE indicates Y, Er, Yb.

3.2.2 Laser ablation in liquid

The Y_2O_3:Er,Yb colloidal solution was prepared by laser ablation in liquid. The target was placed on the bottom of the cell that was filled with 2 ml of deionized water. The Nd:YAG laser (Spectron Laser Systems Ltd., SL8585G) served as a light source for pulsed laser ablation and was operated with the second harmonic generation (wavelength: 532 nm) at a laser energy of 26.0 mJ/pulse and a repetition rate of 10 Hz. The average energy density of the laser was varied in the range of 0.59 – 3.61 J/cm^2. When an alignment paper (Laser Create Corp) was irradiated with laser, the average energy density from the spot size per pulse and the power of the laser was calculated. The pulse width was 13 ns when measured with a fast PIN photodiode and a digital oscilloscope.

3.2.3 Characterizations

The composition of the synthesized target and the prepared nanoparticles characterized with an X-ray diffractometer (XRD, PANalytical X'pert-PRO-MRD). The average particle size was measured by Dynamic Light Scattering (DLS, Sysmex Co. Zetasizer Nano). The laser source of the DLS was a He-Ne laser (633 nm). The morphology of the nanoparticles was observed by scanning electron microscopy (SEM, Hitachi High-Technologies Co. S-4800) and transmission electron microscopy (TEM, JEOL Ltd. JEM-1010BS). The colloidal solution of Y_2O_3:Er,Yb was placed onto the elastic carbon supporting film. A powder of the Y_2O_3:Er,Yb targets was placed on a microscope stage. The elemental analysis of the nanoparticles was performed by energy dispersive X-ray (TEM-EDX) spectroscopy.

3.3 Result and discussion

3.3.1 Phase identification

Figure 3-1 shows the XRD patterns of Y_2O_3:Er,Yb in the synthesized target and the prepared nanoparticles. The standard diffraction data was referred by ICDD-PDF-4 no. 01-079-1716. The synthesized targets and the prepared nanoparticles had a space group *I*a3 of the C-type Y_2O_3 structure. These nanoparticles were prepared at an average fluence of 4.2 J/cm^2. It was found that the crystal phase of the nanoparticles prepared by laser ablation in liquid was the same as that of the targets. No additional peaks representing other phases were observed.

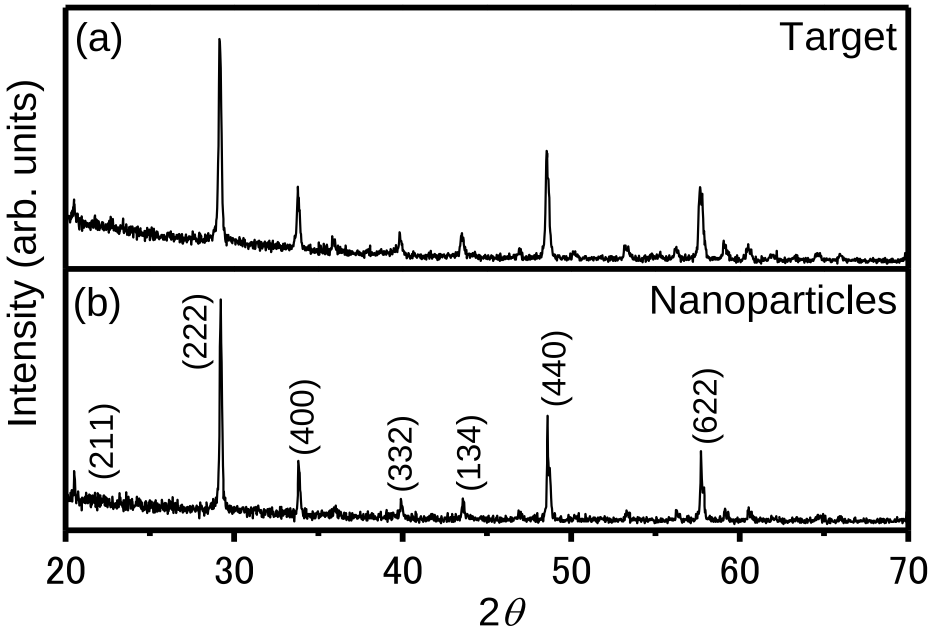

Figure 3-1. XRD pattern of targets (a), and the prepared nanoparticles (b).

3.3.2 Effect of the laser fluence

Figure 3-2 shows the average particle size as a function of the average fluence in laser ablation in liquid (a) and the histograms (b). The secondary particle size was measured with DLS from 0.60 to 3.61 J/cm^2 on the laser fluence. This particle size was calculated from the scattering intensity of the fluctuation, which is dependent on the Brownian motion of the particle. So these particle sizes are a fluid mechanical diameter. It was found that the particle size increased with the increasing the fluence of the laser. Yoshimura et al. showed a similar tendency [15]. The particle size would be increased by aggregating each other.

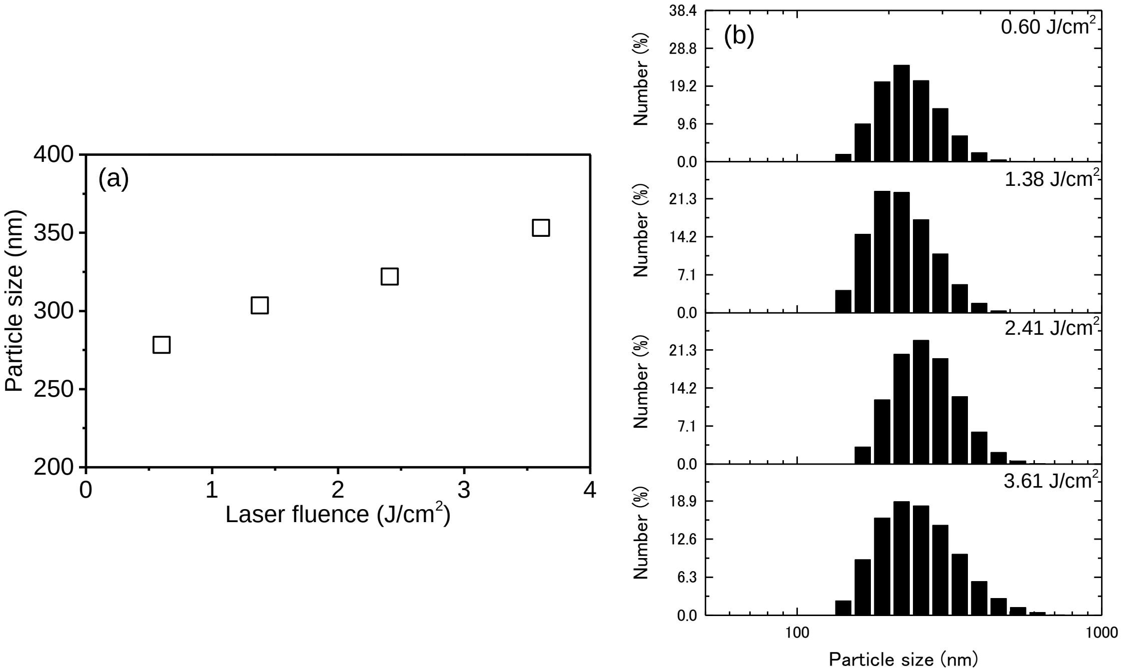

Figure 3-2. Particle size as a function of the fluence for laser ablation in liquid (a) and histograms (b).

The morphology of the nanoparticles was observed by SEM. In SEM images, nanoparticles of a few hundreds nm were observed. Figure 3-3 shows the SEM images of the synthesis targets and the nanoparticles prepared by laser ablation in liquid. Figure 3-3(a) shows the SEM images of the targets. Many aggregated nanoparticles of a few hundreds nm were observed. Figure 3-3 (b)-(d) shows the SEM images of the nanoparticles. The average fluence in Figure 3-3(b)-(d) is 0.59, 1.06 and 1.61 J/cm^2, respectively. In 0.35 J/cm^2, the nanoparticles of a few hundreds nm were not observed. In the range between 0.59 and 1.61 J/cm^2, the nanoparticles of a few hundreds nm were observed. During the preparation of the nanoparticles, the threshold laser fluence ranged between 0.35 and 0.59 J/cm^2. It was found that the particle size increased with increasing laser fluence in a similar manner as DLS. The nanoparticles were aggregated to each other. The size of the primary particles was nearly unchanged by the laser fluence. It was found that the size and morphology of the nanoparticles of a few hundreds nm was nearly the same as the size and morphology of the targets.

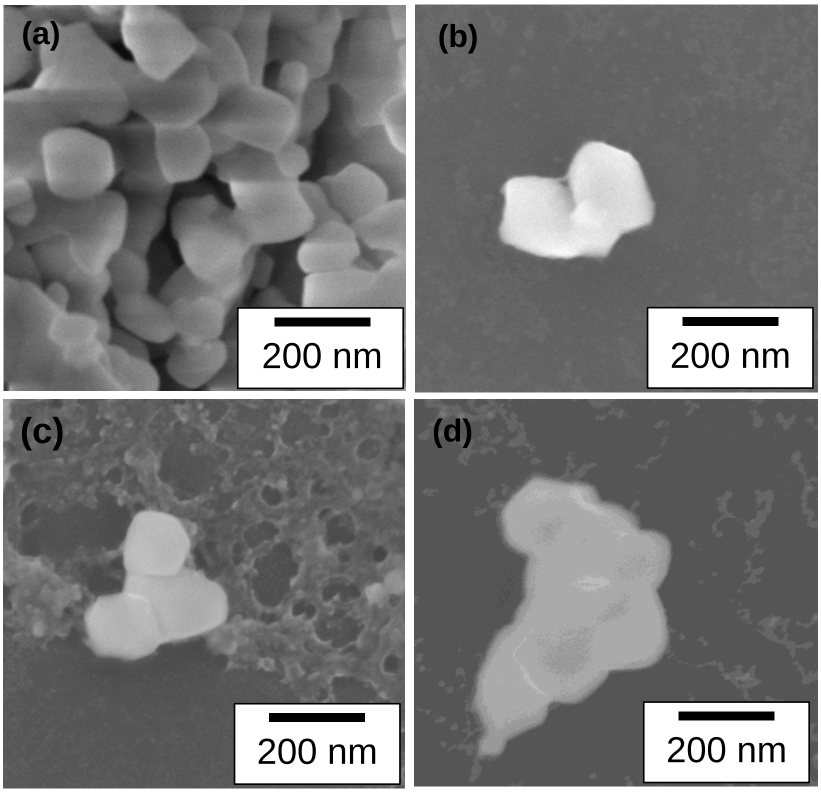

Figure 3-3. SEM images of the targets and the nanoparticles. Target (a), 0.59 J/cm^2 (b), 1.06 J/cm^2 (c), and 1.61(d) J/cm^2 [16].

Figure 3-4 shows the histograms of the targets and the nanoparticles from the SEM images (Figure 3-3). These histograms show the primary particle size. Figure 3-4 (a) shows the histograms of the targets, Figure 3(b)-(d) shows the histograms of the nanoparticles. The average particle size was 122.2 ± 39.2 nm. As well as SEM images, the laser fluence in Figure 3-4 (b)-(d) is 0.60, 1.06, and 1.61 J/cm^2, respectively. The average particle sizes are 148 ± 49.6 nm, 152 ± 48.6 nm, and 143 ± 49.0 nm at the laser fluence of 0.60, 1.06, and 1.61 J/cm^2, respectively. After laser irradiation, the primary particle size was increased. In fact, sphere particles were observed by SEM (Figure 3-5). These particles would be prepared by heat of laser. The laser fluence was 1.38 J/cm^2. After the primary particles aggregated, they would be melted by heat of the laser. Similar phenomenon happens in reference [17].

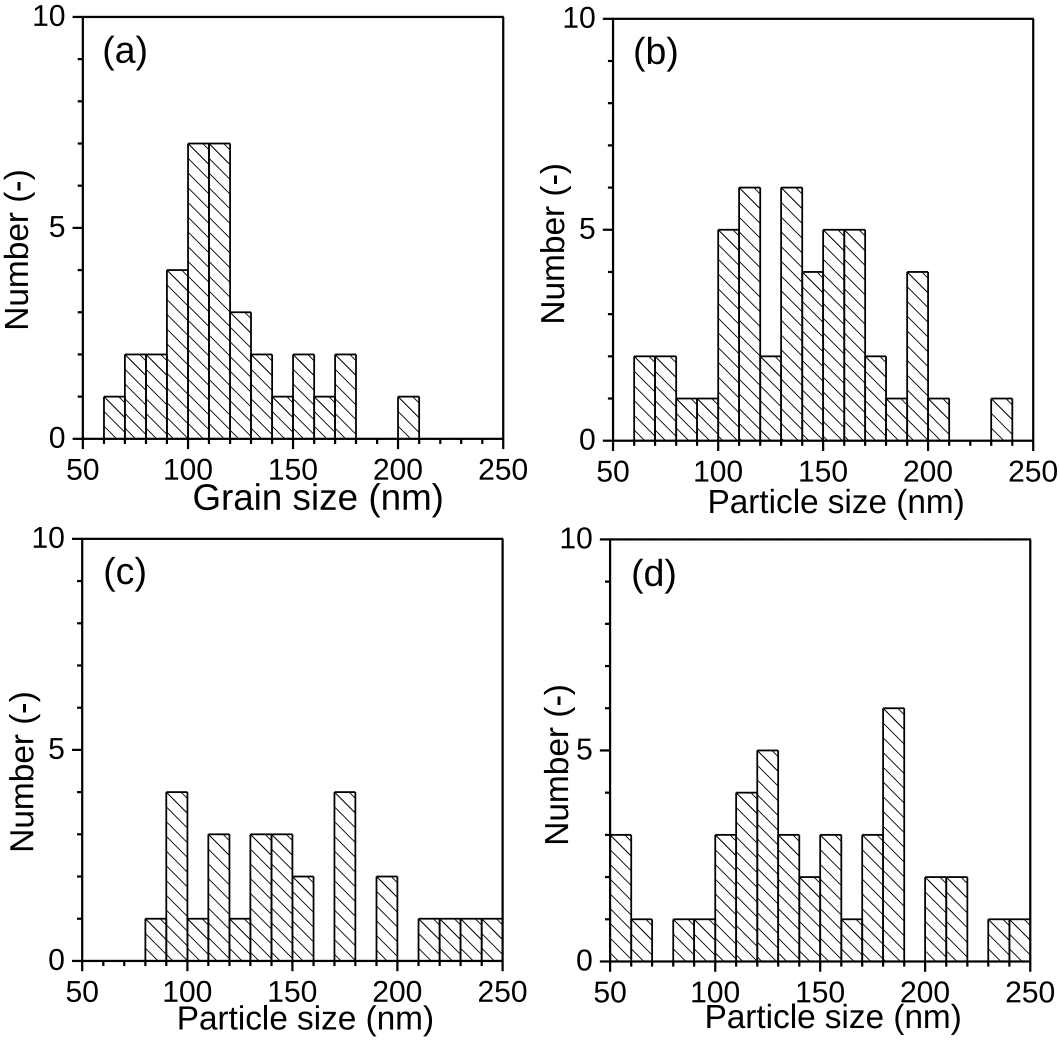

Figure 3-4. Histograms of the targets and the nanoparticles from the SEM images (Figure 3-3). Targets (a), 0.60 J/cm^2 (b), 1.06 J/cm^2 (c), and 1.61 J/cm^2 (d).

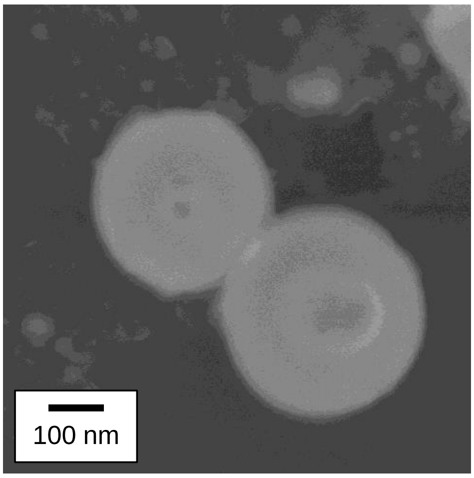

Figure 3-5. SEM image of sphere particles in laser fluence of 1.38 J/cm^2.

SEM images showed the fine nanoparticles of a few tens nm surrounding the larger nanoparticles. Figure 3-6 (a), (b) and (c) shows the SEM images for the fluence of 0.60, 1.38 and 3.61 J/cm^2, respectively. At 0.60 J/cm^2, dot-like nanoparticles were observed. At both 1.38 and 3.61 J/cm^2, net-work materials were observed. These net-work materials are called often nano-strings [18]. These materials would be generated by quenching of plume plasma.

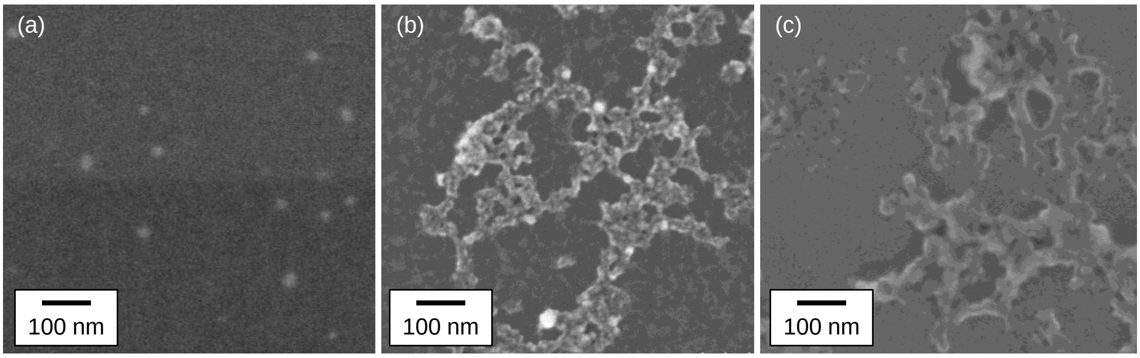

Figure 3-6. SEM images at the laser fluence of 0.60 (a), 1.38 (b), and 3.61 J/cm^2 (c).

Figure 3-7 shows the histograms of nanoparticles and nano-strings shown in Figure 3-6. Figures 3-7 (a) shows the histogram of the particle size of the dot-like nanoparticles at the laser fluence of 0.60 J/cm^2. When the laser fluence was 0.60 J/cm^2, the average particle size was 22.0 ± 4.3 nm. Figures 3-7 (b) and (c) show the histograms of the width of the nano-strings at the laser fluence of 1.38 and 3.61 J/cm^2, respectively. In the former case, the average width of the nano-strings was 25.0 ± 7.5 nm. In the latter case, the average width of the nano-strings was 29.7 ± 16.4 nm. Figure 3-8 shows particle and nano-string size as a function of the laser fluence. It was observed that the laser fluence increased with increasing gradually in the size. Also, the laser fluence increased with increase of error bar. That is, nano-strings were generated by the aggregation of the dot-like nanoparticles. It was suggested that neck growth of liquid sintering happened in the interface between dot-like nanoparticles

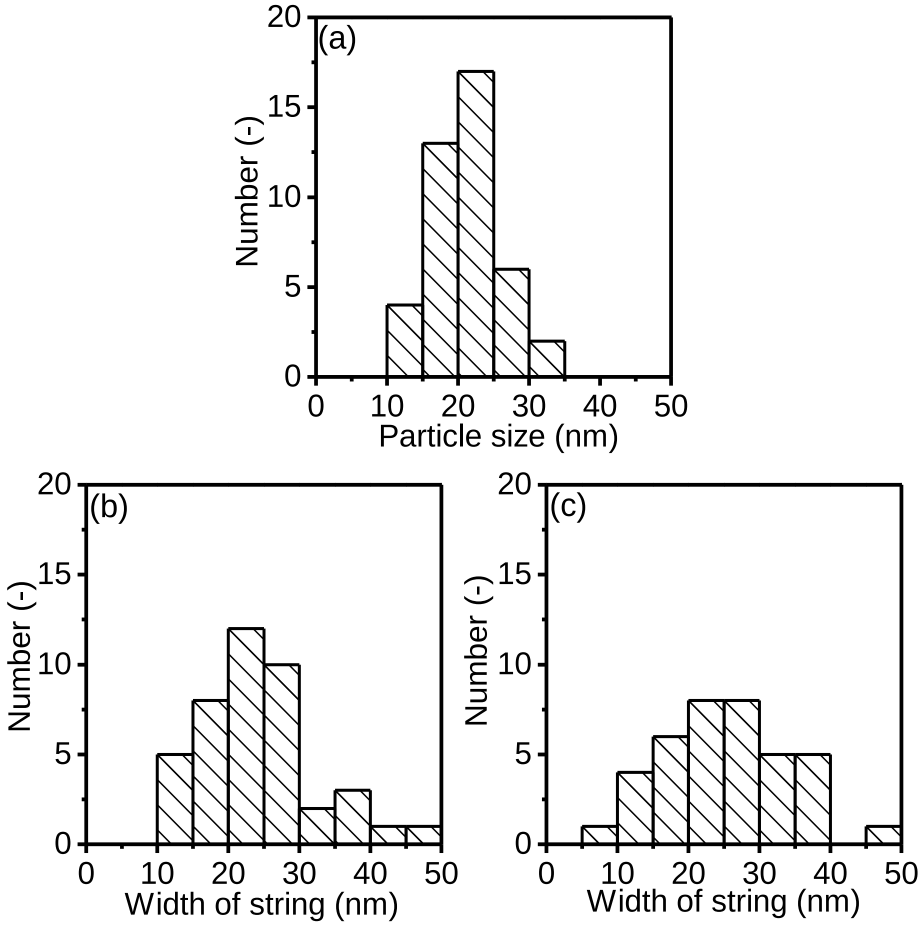

Figure 3-7. Histograms of nanoparticles and nano-strings shown in Figure 3-6.

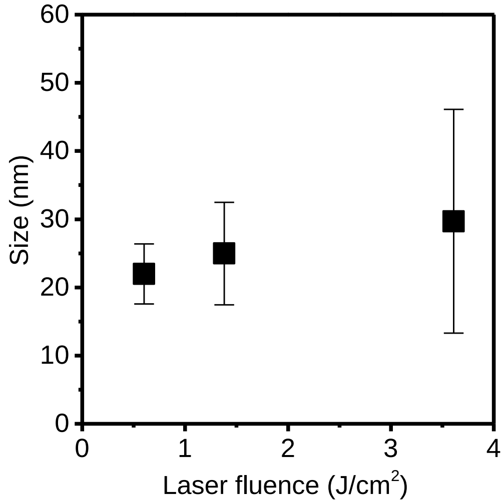

Figure 3-8. Particle and nano-string size as a function of the laser fluence.

Figure 3-9 (a) shows the TEM images for the laser fluence of the 1.61 J/cm^2. In Figure 3-9 (a), nano-strings with lattice fringes were observed. The images confirmed that the direction of the lattice fringes varied. Then, lattice spacings *d* of 3.06 Å were observed. This corresponded to the d_{222} lattice plane of cubic Y_2O_3. Therefore, it was found that this nano-string was cubic Y_2O_3. Figure 3-9 (b) shows the EDX spectrum of the nano-strings. The peaks of Y (K_{ab}, K_β, L_α), Yb (L_α, M), and Er ($LIII_{ab}$, L_α, M) were identified. Additional peaks for Cu were attributed to the copper grid. Based on these findings, it was concluded that the nano-strings was Y_2O_3:Er,Yb.

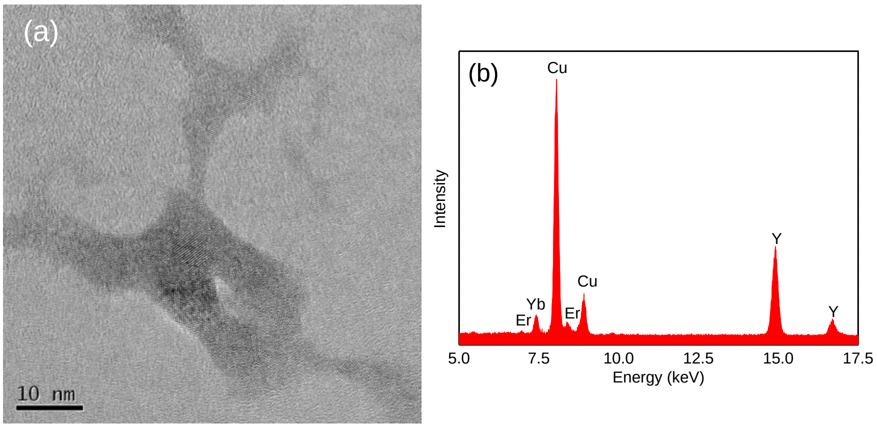

Figure 3-9. TEM images of a nano-string (a) and the EDX spectrum (b).

Figure 3-10 shows productivity as a function of the laser fluence. The productivity of the particles was measured by ICP-MS. The productivity of the particles was increased with increasing the laser fluence. S. Barcikowski et al. reported that the productivity of the particles was increased with increasing the laser fluence [12]. From Figure 3-6, the dot-like nanoparticles were generated at low fluence. The nano-strings were generated at high fluence. At the relationship between morphology and productivity of the particles, when productivity of the particles was increased, it was suggested to be easy to generate nano-strings.

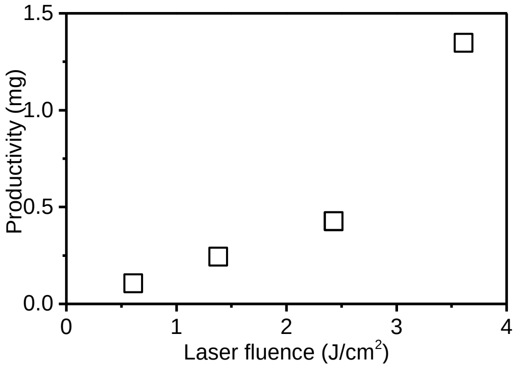

Figure 3-10. Productivity as a function of the laser fluence.

3.3.3 Effect of the irradiation times

Figure 3-11 shows the average particle size and the histograms measured by DLS at various irradiation times. Then, the laser fluence was 1.38 J/cm^2. The average particle was increased with passing the irradiation time. After irradiation time was 30 min, the average particle size was saturated. As well as the effect of laser fluence, the particle size would be increased by aggregating each other. However, differing from the effect of laser fluence, because at the constant fluence, melting energy which laser fluence was transferred to was limited, the average particle size would be saturated.

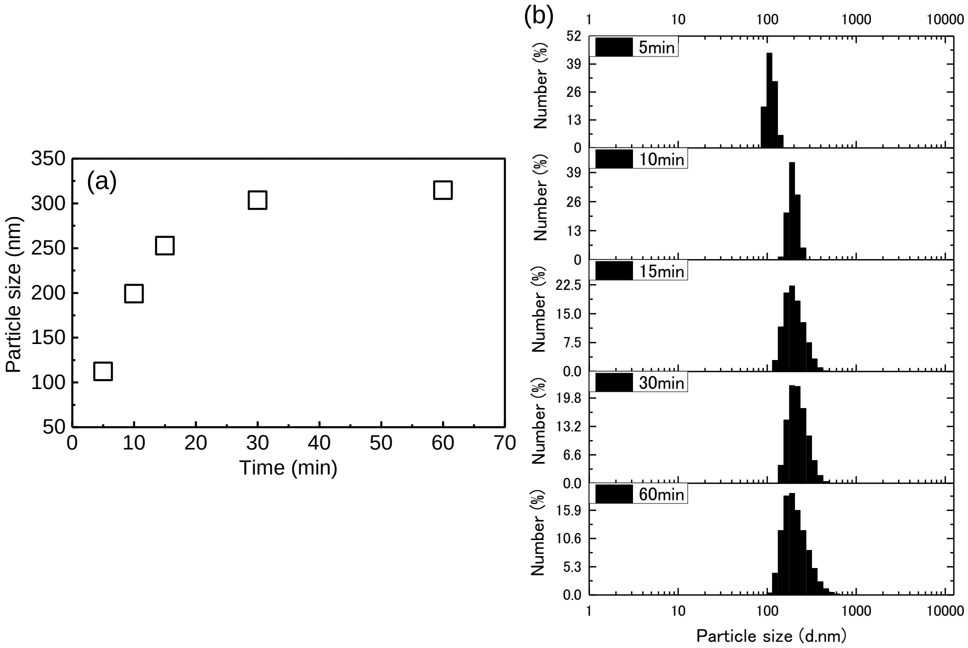

Figure 3-11. Particle size (a) and histograms (b) of the nanoparticles on the irradiation time.

The morphology of the nanoparticles was observed by SEM. In SEM images, nanoparticles of a few hundreds nm were observed. Figure 3-12(a) shows the SEM images of the targets. Figure 3-12 (a)-(e) shows the SEM images of the nanoparticles prepared by laser ablation in liquid. The irradiation time in Figure 3-12 (a)-(e) is 5, 10, 15, 30, and 60 min, respectively. Many aggregated nanoparticles of a few hundreds nm were observed. It was found that the particle size increased with passing irradiation time in a similar manner as DLS. However, when irradiation time after 15 min was passing, the secondary particle size was unchanged. The size of the primary particles was nearly unchanged by the irradiation time. It was found that the size and morphology of the nanoparticles of a few hundreds nm was nearly the same as the size and morphology of the targets.

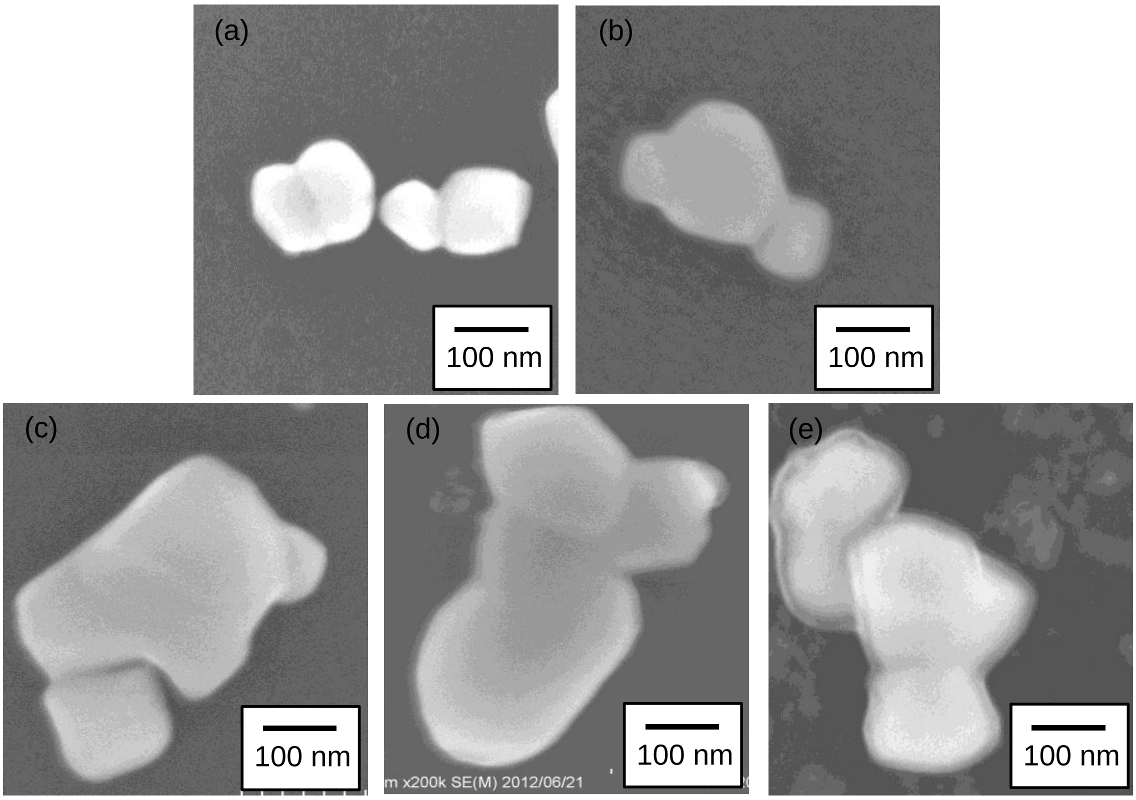

Figure 3-12. SEM images of the nanoparticles of a few hundreds nm prepared by the laser irradiation. Irradiation times were 5 (a), 10 (b), 15 (c), 30 (d), and 60 min (e).

Figure 3-13 shows the SEM images of the nanoparticles after the laser irradiation. Figures 3-13 (a), (b), (c), and (d) show the SEM images at irradiations times of 5, 15, 30, and 60 min, respectively. The nanoparticles having a particle size of a few tens nanometers were observed after laser irradiation. These nanoparticles were prepared by quenching the plume plasma generated on the target surface by laser irradiation, because the morphology and the size of the prepared nanoparticles were different from those of the target particles. At irradiation times of between 5 and 15 min, dot-like nanoparticles were observed. In an irradiation time of 30 min, on the other hand, nano-strings, which have a network structure, were observed. In an irradiation time of 60 min, a network structure was generated by aggregating the dot-like nanoparticles. From these results, it was concluded that the irradiation time increased with an increase in the number of dot-like nanoparticles. Thereafter, when the irradiation time crossed 30 min, the dot-like nanoparticles aggregated. Nano-strings were generated by heating the aggregated dot-like nanoparticles.

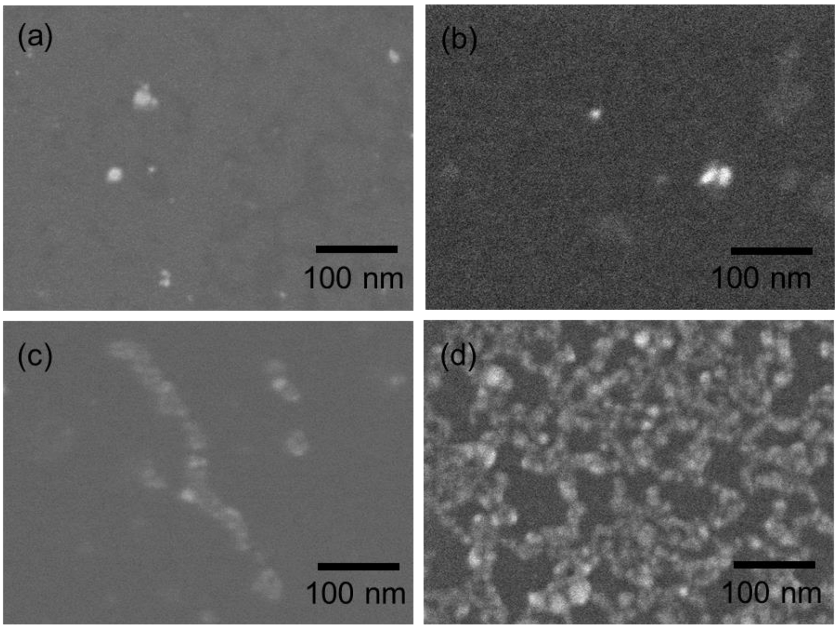

Figure 3-13. SEM images of the nanoparticles prepared by the laser irradiation. Irradiation times were 5 (a), 15 (b), 30 (c), and 60 min (d).

Figure 3-14 shows the histograms of nanoparticles and nano-strings shown in Figure 3-13. Figures 3-14 (a) and (b) show the histograms of the particle size of the dot-like nanoparticles at irradiation times of 5 and 15 min, respectively. When the irradiation time was 5 min, the average particle size was 16.0 ± 3.7 nm. In the latter case, the average particle size was 18.7 ± 5.5 nm. Figures 3-14 (c) and (d) show the histograms of the width of the nano-strings at irradiation times of 30 and 60 min, respectively. In the former case, the average width of the nano-strings was 21.8 ± 4.9 nm. In the latter case, the average width of the nano-strings was 21.9 ± 4.9 nm. Figure 3-15 shows particle and nano-string size as a function of the irradiation time. At the irradiation time from 5 to 30 min, it was observed that the irradiation time increased with a gradual increase in the particle size. At the irradiation time after 30 min, it was observed that the average width of the nano-strings hardly changed. That is, nano-strings were generated by the aggregation of the dot-like nanoparticles. The structure these nano-strings are known as the network structure prepared by laser ablation in liquid [19-22].

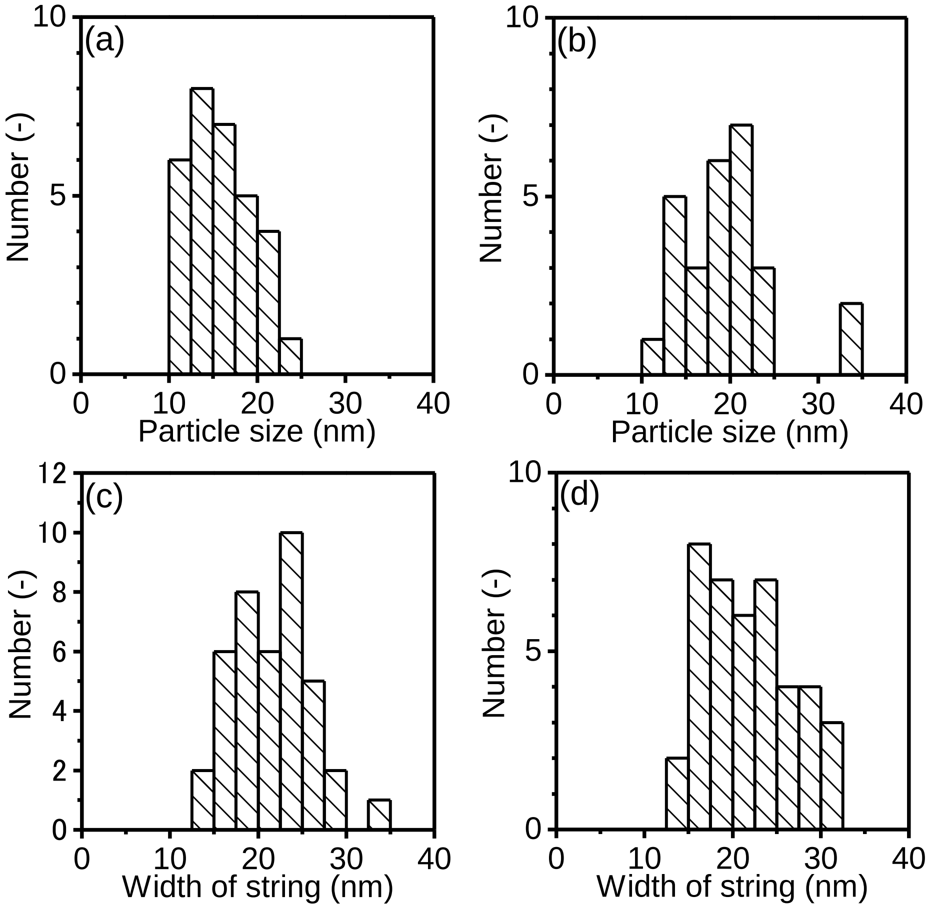

Figure 3-14. Histograms of nanoparticles and nano-strings shown in Figure 3-13.

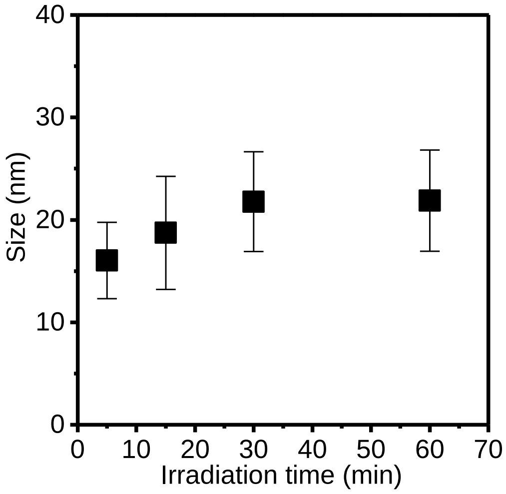

Figure 3-15. Particle and nano-string size as a function of the irradiation time.

Figure 3-16 shows productivity as a function of the irradiation time. As well as the effect of laser fluence, the productivity of the particles was measured with ICP-MS. The productivity of the particles was increased with passing the irradiation time. From Figure 3-13, the dot-like nanoparticles were generated at short irradiation times. The nano-strings were generated at long irradiation times. At the relationship between morphology and The productivity of the particles, when productivity of the particles is increased, it is suggested to be easy to generate nano-strings as well as the effect of laser fluence.

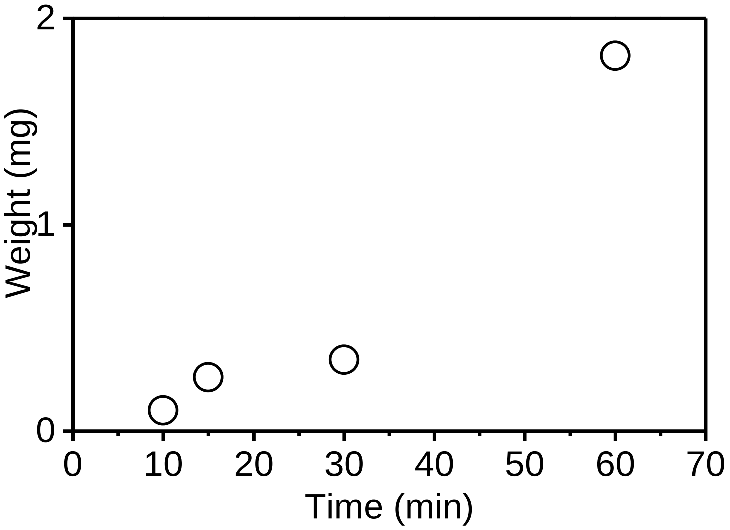

Figure 3-16. Productivity as a function of the irradiation time.

3.3.4 Laser ablation in colloidal solution

After colloidal solution prepared by laser ablation in liquid was separated by using a membrane filter (pore size: 0.1 μm), laser ablation in colloidal solution was carried out (Figure 3-17). Figure 3-18 shows SEM images of nanoparticles prepared by laser ablation in colloidal solution. Figure 3-18 (a), (b), and (c) are 0 min, 10 min, and 30 min of the irradiation time, respectively. The laser fluence was 1.38 J/cm^2. Although nano-strings were observed at 0 min of irradiation time, no nano-strings were observed at 10 min and 30 min of irradiation time. Instead of the nano-strings, nanoparticles of a few hundreds nm were observed. These nanoparticles would be prepared from nano-strings heated by laser irradiation. That is, sintering by laser irradiation would happen. Also surrounding fine nanoparticles would be prepared by coulomb explosion process.

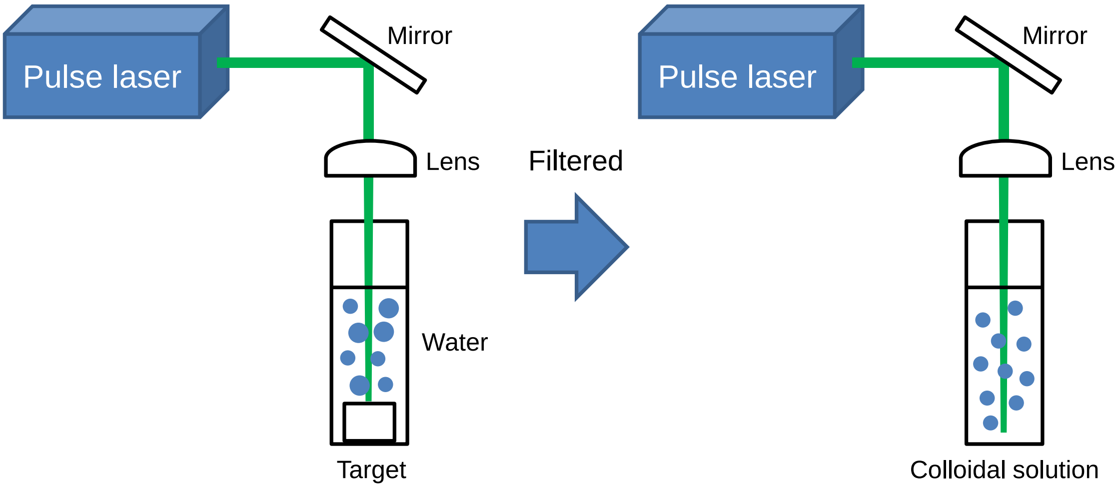

Figure 3-17. Experimental procedure of laser ablation in liquid.

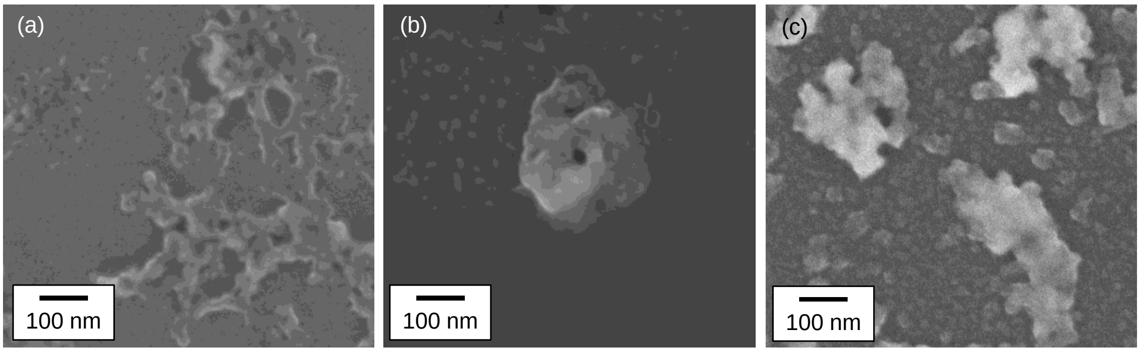

Figure 3-18. SEM images of nanoparticles prepared by laser ablation in colloidal solution: irradiation time was 0 min (a), 10 min (b), and 30 min (c).

3.3.5 Preparation process

When targets are irradiated with a laser, a plume plasma is prepared on the surface of the target [10]. Firstly, it has been known that a shock wave of high pressure was created on the target surface by counteraction of the plume plasma. The plume plasma is expanded and quenched by surrounding solution. After quenching the plasma plume, a cavitation bubble is generated. Then, a shock wave is generated by counteraction of the cavitation bubble. The particles of a few hundreds nm would be prepared at high pressure and shock wave by fragmentation of the target. On the contrary, in the particles of a few tens nm, nucleation would occur and they would be grown in the plume plasma which consisted of materials such as atoms, electrons, ions and clusters. At low energy densities or short irradiation time, the fine dot-like nanoparticles would be prepared. The number of dot-like nanoparticles increased with increased the energy density or irradiation time. Subsequently, the dot-like nanoparticles were aggregated to each other. When a laser was irradiated again, the aggregated dot-like nanoparticles melted from the heat of laser. Finally, the nano-strings formed by these phenomena. Figure 3-19 shows an illustration of the nanoparticles formation process.

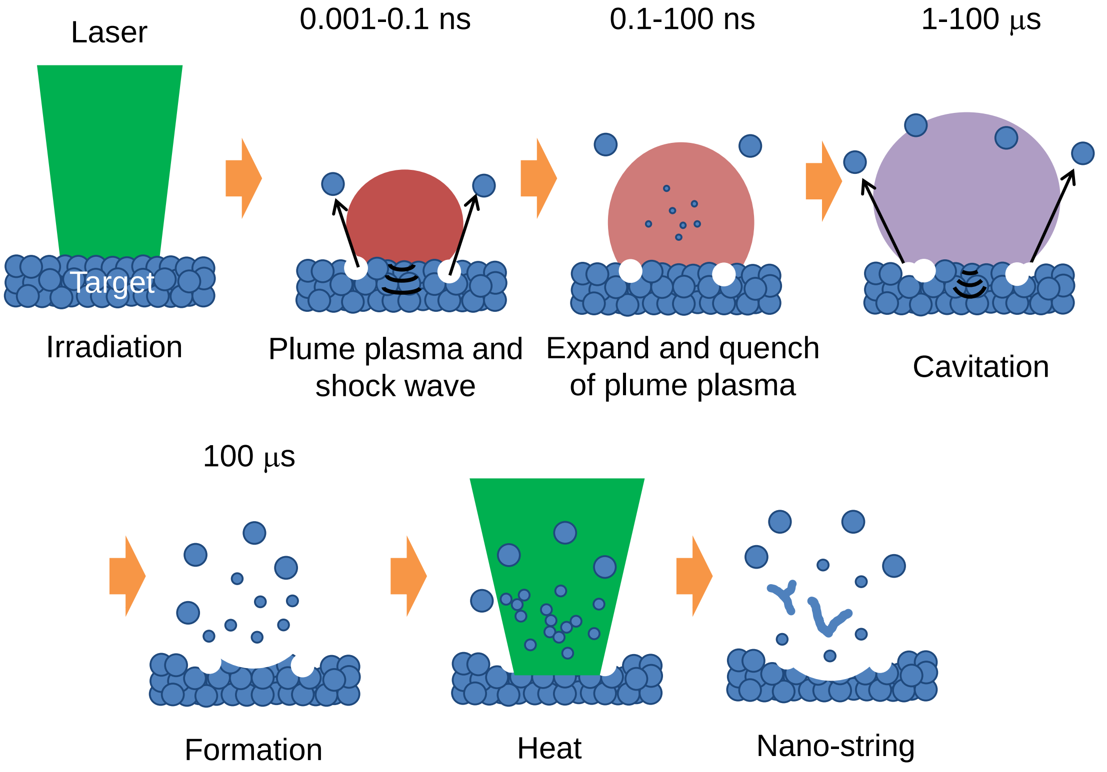

Figure 3-19. An illustration of the nanoparticles formation process.

3.4 Conclusions

Y_2O_3:Er,Yb nanoparticles were successfully prepared by laser ablation in liquid. The coarse nanoparticles were observed by SEM. When targets are irradiated with a laser, a plume plasma is prepared on the surface of the target. High pressure of shock wave was generated by counteraction of plume plasma. After quenching the plasma plume, a cavitation bubble is generated. Then, a shock wave is generated by counteraction of the cavitation bubble. The coarse nanoparticles would be prepared by the shock wave. The coarse nanoparticles depend on particle of target surface. Conversely, the fine nanoparticles were prepared by quench of the plume plasma. The number of the fine nanoparticles was increased with increasing laser fluence or irradiation time. As a result, nano-strings would be prepared by increasing the number of the fine nanoparticles. Nano-string would form network structure by heat of the laser.

3.5 References

[1] J. Zhou, Z. Liu, and F. Li, *Chemical Society Reviews* 41 (2012) 1323-1349.

[2] E. Downing, L. Hesselink, J. Raslton, and R. Macfarlane, *Science.* 273 (1996) 1185-1189.

[3] B. M. Ende, L. Aarts, and A. Meijerink, *Physical Chemistry Chemical Physics* 11 (2009) 11081-11095.

[4] F. Auzel, *Chemical Reviews* 104 (2004) 139-173.

[5] J. A. Capobianco, F. Vetrone, J. C. Boyer, A. Speghini, and M. Bettinelli, *Journal of Physical Chemistry B* 106 (2002) 1181-1187.

[6] F. Vetrone, J. C. Boyer, J. A. Capobianco, A. Speghini, and M. Bettinelli, *Journal of Applied Physics.* 96 (2004) 661-667.

[7] A. Ambrosini, A. Duarte, K. R. Poeppelmeier, M. Lane, C. R. Kannewurf, and T. O. Mason, *Journal of Solid State Chemistry*. 153 (2000) 41-47.

[8] Z. Heiba, H. Okuyucu, and Y. S. Hascicek, *Journal of Applied Crystallography*. 35 (2002) 577-580.

[9] C. Meyer, J. P. Sanchez, and J. Thomasson, and J. P. Itie, *Physical Review B.* 51 (1995) 12187-12192.

[10] F. Mafune, J. Kohno, Y. Takeda, T. Kondow, and H. Sawabe, *Journal of Physical Chemistry B.* 104 (2000) 9111-9117.

[11] V. Amendola, and M. Menghetti, *Physical Chemistry Chemical Physics*. 15 (2013) 3027-3046.

[12] C. L. Sajti, R. Sattari, B. N. Chichkov, and S. Barcikowski, *Journal of Physical Chemistry C.* 114 (2010) 2421-2427.

[13] V. Amendola, and M. Menghetti, *Journal of Materials Chemistry*. 17 (2007) 4705-4710.

[14] Z. Yan, G. Compagnini, and D. B. Chrisey, *Journal of Physical Chemistry C.* 115 (2011) 5058-5062.

[15] F. Yoshimura, K. Nakamura, F. Wakai, M. Hara, M. Yoshimoto, O. Odawara, H. Wada, *Applied Surface Science.* 257 (2011) 2170-2175.

[16] T. Nunokawa, Y. Onodera, M. Hara, Y. Kitamoto, O. Odawara, and H. Wada, *Applied Surface Science*. 261 (2012) 118-122.

[17] H. Q. Wang, A. Pyatenko, K. Kawaguchi, X. Y. Li, Z. Swiatkowska-Warkocka, and N. Koshizaki, *Angewandte Chemie International Edition.* 49 (2010) 6361-6364.

[18] S. Inasawa, M. Sugiyama, and Y. Yamaguchi, *Journal of Physical Chemistry B.*109 (2005) 9404-9410.

[19] K. Saitow, Y. Okamoto, and Y. F. Yano, *Journal of Physical Chemistry C.* 116 (2012) 17252-17258.

[20] S. Besner, A. V. Kabashin, and M. Meunier, *Applied Physics A*, 88, (2007) 269-272.

[21] J. P. Sylvestre, S. Poulin, A. V. Kabashin, E. Sacher, M. Meunier, and J. H-T. Luong. *Journal of Physical Chemistry B*, 108 (2004) 16864-16869.

[22] T. Tsuji, N. Watanabe, and M. Tsuji. *Applied Surface Science*, 211 (2003) 189-193.

Chapter 4 Crystallinity of Y_2O_3:Er,Yb nanoparticles

4.1 Introduction

As a significant problem in the preparation of nano-phosphors, a homogeneous distribution of activators in host materials is important. When activators are distributed heterogeneously in host materials, localized concentration quenching occurs because of the migrating excitation energy. Because the probability of non-radiative relaxation by a trap state such as a surface defect increases, the luminous efficiency decreases. The homogeneous distribution of activators is a significant theme in the field of nano-phosphors [1, 2].

Further, fluorescent nanoparticles have been prepared by various wet chemical methods, such sol-gel method [3, 4], hydrothermal synthesis method [5, 6], and reverse micelle method [7, 8]. In general, however, a sintering process is carried out for the preparation of nanoparticles. In this low-temperature process, the crystallinity of nanoparticles is low [2, 9-10]. Therefore, the luminous efficiency is low because of the scattering of the excitation light. In contrast, at a high temperature, the particle size is increased [2, 11]. It is difficult to prepare fine nanoparticles having a high luminous efficiency. Hence, laser ablation in liquid has been focused on. This is a technology using which nanoparticles are prepared by irradiating a highly crystalline bulk target with a laser [12]. Thus, the preparation of the highly crystalline nanoparticles is possible. As a general mechanism, when a target is irradiated with a laser, plume plasma is generated on the target. Then, nanoparticles are prepared by quenching this plume plasma around a solvent [13-15]. Moreover, a shock wave is generated as an opposite reaction. After the quenching of the plume plasma, cavitation bubbles are generated. Therefore, it is known that a high pressure (in the order of a few GPa) is generated on the surface of the targets [16-17]. The shock wave and the cavitation bubble have a significant effect on the generation of nanoparticles.

As described in chapter 3, it has been discovered that the nanoparticles having a particle size of a few hundred nanometers can be prepared by using a shock wave and cavitation bubbles and that the nanoparticles having a particle size of a few ten nanometers prepared by the quenching of plume plasma. However, the details of the crystallinity and the distribution of the dopant in nanoparticles prepared by laser ablation in liquid are not yet known.

In this chapter, the crystallinity and the distribution of the dopants in nanoparticles prepared by laser ablation in liquid were investigated. For the preparation of the nanoparticles, nano-second Nd:YAG laser was used. The crystallinity of the nanoparticles was investigated by using an X-ray diffractometer (XRD). The distribution of the dopant in the nanoparticles was investigated by using scanning transmission electron microscopy-energy dispersive X-ray spectroscopy (STEM-EDX).

4.2 Experimental

Preparation method of the target was as same as that in chapter 3. A laser equipment was used as same as that in chapter 3. Volume of de-ionized water and plastic cuvette were as same as that in chapter 3. Conditions of laser ablation in liquid in the preparation of the dot-like nanoparticles were as follows: laser fluence 1.38 J/cm^2 and irradiation time: 15 min. Conditions of laser ablation in liquid in the preparation of the nano-strings were as follows: laser fluence = 1.38 J/cm^2 and irradiation time = 30 min. In order to investigate the composition ratio of the nanoparticles generated from the quenching of the plume plasma, these nanoparticles under 100 nm were separated by using a membrane filter (Omnipore membrane filter, Filter Type: 0.1 μm Merck Millipore).

An X-ray diffractometer (XRD, Philips X'pert-PRO-MRD) was used for measuring the crystallinity of the prepared nanoparticles. The prepared Y_2O_3:Er,Yb nanoparticles were placed onto an elastic carbon supporting film. The film was dried at 60 °C for 1 h. The morphology of the nanoparticles was observed with SEM (Hitachi High-Technologies Co. S-4800) and TEM (JEOL Ltd. JEM-1010BS or Hitachi High-Technologies Co. H-8100). In the elemental analysis of the nanoparticles, STEM–EDX (JEOL Ltd. JEM-2100F) and ICP-MS (PerkinElmer Japan Co. Ltd. ELAN DRC-e) was used.

4.3 Results and discussion

4.3.1 Full-width half-maximum and crystallite diameter

Figure 4-1 shows the XRD patterns of the synthesized target and nanoparticles prepared by laser ablation in liquid. Figures 4-1 (a), (b), and (c) show the XRD patterns of the nanoparticles prepared in the laser fluence of 1.38, 2.43, 3.61 J/cm^2, respectively. Figure 4-1 (d) shows the XRD patterns of the prepared target. It was confirmed that the prepared nanoparticles and the target had *Ia*3 C-type crystal structure of Y_2O_3 (PDF No. 01-089-5592). No additional peak representing any other crystal phase was confirmed in the nanoparticles prepared by laser irradiation. The full-width half-maximum (FWHD) of the peaks at $2\theta = 29.1°$ was 0.14 in the target. The FWHD of the peaks ($2\theta = 29.1°$) of the nanoparticles prepared by laser ablation in liquid was between 0.11 and 0.14. Table 4-1 shows FWHD and crystallite diameter. Therefore, nanoparticles were prepared by laser ablation in liquid while maintaining an almost high crystallinity of the target. Crystallite diameter D (nm) was calculated by the Scherrer formula. The formula is given by the follows

$$D = \frac{K\lambda}{(\beta\cos\theta)} \tag{4-1}$$

where K is the shape coefficient for the reciprocal lattice point (K = 0.89), λ is the wavelength of the Cu Kα radiation (0.154 nm), β is the corrected half-width of the diffraction peak, and θ is Bragg's angle of the diffraction peak. Crystallite diameter of target was smaller than particle size of SEM observation in Figure 3-4 (a). The target would be poly-crystal particle by aggregation of plural crystallite diameters. Also, after laser irradiation, the crystallite diameter was smaller than particles in Figure 3-4. The crystallite diameter was larger than size of nano-strings. That is, the measured powder was included into both nanoparticles of a few hundreds nm and nano-strings. Because coarse nanoparticles, nano-strings, and dot-like nanoparticles were melted by the laser irradiation, the prepared nanoparticles ware poly-crystal. Therefore, the crystallite diameter was smaller than coarse nanoparticles. Figure 4-2 shows this illustration.

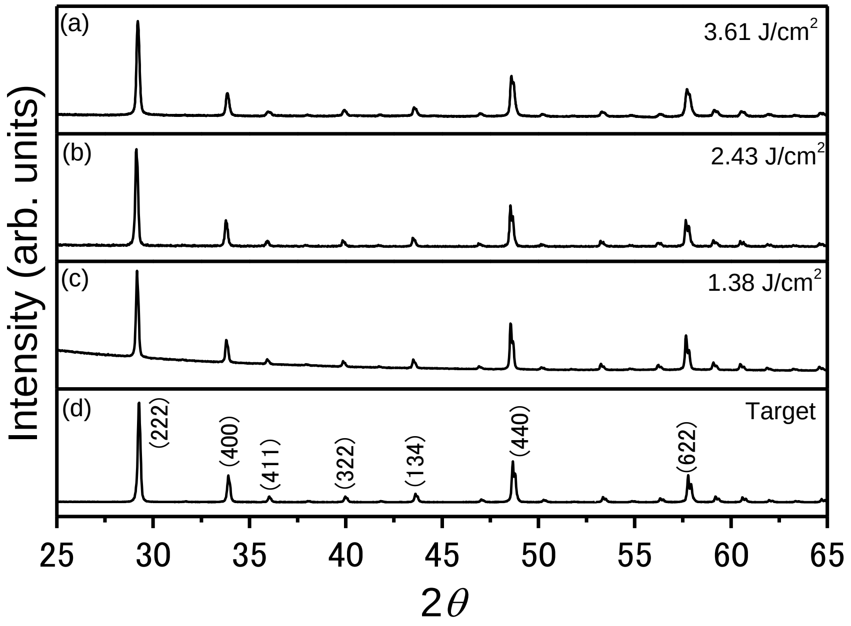

Figure 4-1. XRD patterns of the nanoparticles prepared in the fluence of 1.38 (a), 2.43 (b), 3.61 J/cm^2 (c), and the synthesized targets (d).

Table 4-1. FWHD and crystallite diameter of the target and the nanoparticles prepared by laser ablation in liquid.

		FWHD in 2θ=29.1°	Crystallite diameter (nm)
(a)	3.61 J/cm^2	0.14	59.6
(b)	2.43 J/cm^2	0.11	78.6
(c)	1.38 J/cm^2	0.12	67.8
(d)	Target	0.14	94.5

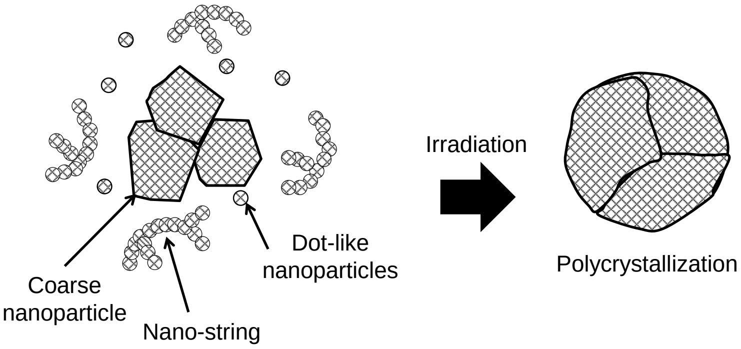

Figure 4-2. Discussion of the decreased crystallite diameter.

Figure 4-2 (a) shows TEM image of the nanoparticles prepared by laser ablation in liquid on the irradiation time of 5 min (The laser fluence: 3.61 J/cm^2). Figure 4-2 (b) is the high magnification image. Dot-like nanoparticles were observed. The nanoparticles had no lattice fringe. That is, the nanoparticles were amorphous. On the other hand, Figure 4-2 (c) shows TEM image of the nanoparticles prepared by laser ablation in liquid on the irradiation time of 30 min (The laser fluence: 3.61 J/cm^2). Figure 4-2 (d) is the high magnification image. Nano-strings were observed. Lattice fringe of the nano-strings observed. The nano-strings were poly-crystal. As a result, after 30 min of irradiation time, the nanoparticles would be sintered by laser irradiation.

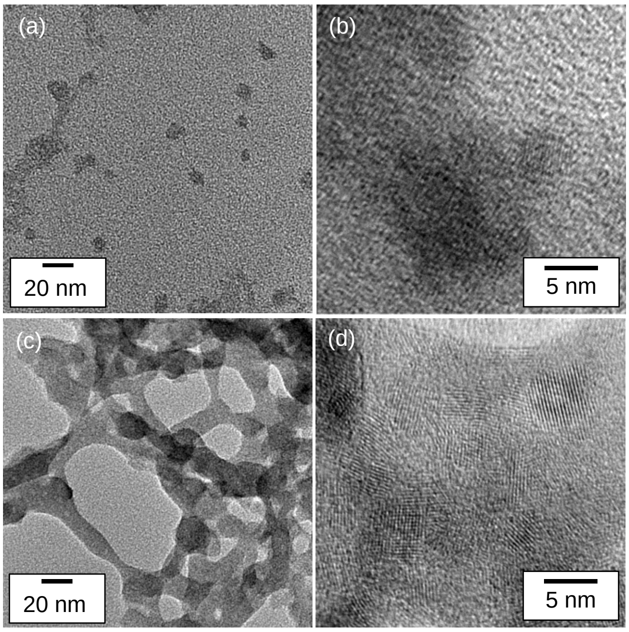

Figure 4-3. TEM pictures of the nanoparticles prepared by laser ablation in liquid: low magnification (a) and high magnification (b) on irradiation time of 5 min and low magnification (c) and high magnification (d) on irradiation time of 30 min.

4.3.2 Distribution of dopants

Figure 4-3 shows a bright-field STEM (BF-STEM) image and the EDX mappings of the nanoparticles prepared by laser ablation in liquid. Further, the aggregation of nanoparticles having a particle size of a few hundred nanometers was observed. Because the nanoparticles were similar to the morphology and the size of the particles in the target, the nanoparticles depending on these target particles were found [18]. The target was fragmented into nanoparticles by the high pressure generated by the shock waves and cavitation bubbles upon laser irradiation. Figure 4-3 (a) shows a BF-STEM image of the nanoparticles prepared by laser ablation in liquid. Figures 4-3 (b), (c), (d), and (e) show the STEM-EDX mappings. The EDX mappings of Y (K_α), Er ($LIII_{ab}$), Yb (L_α), and O (K_α) were observed. It was found that Er and Yb had a uniform distribution in Y_2O_3. That is, the activator (Er) and the sensitizer (Yb) were doped in the host materials (Y_2O_3).

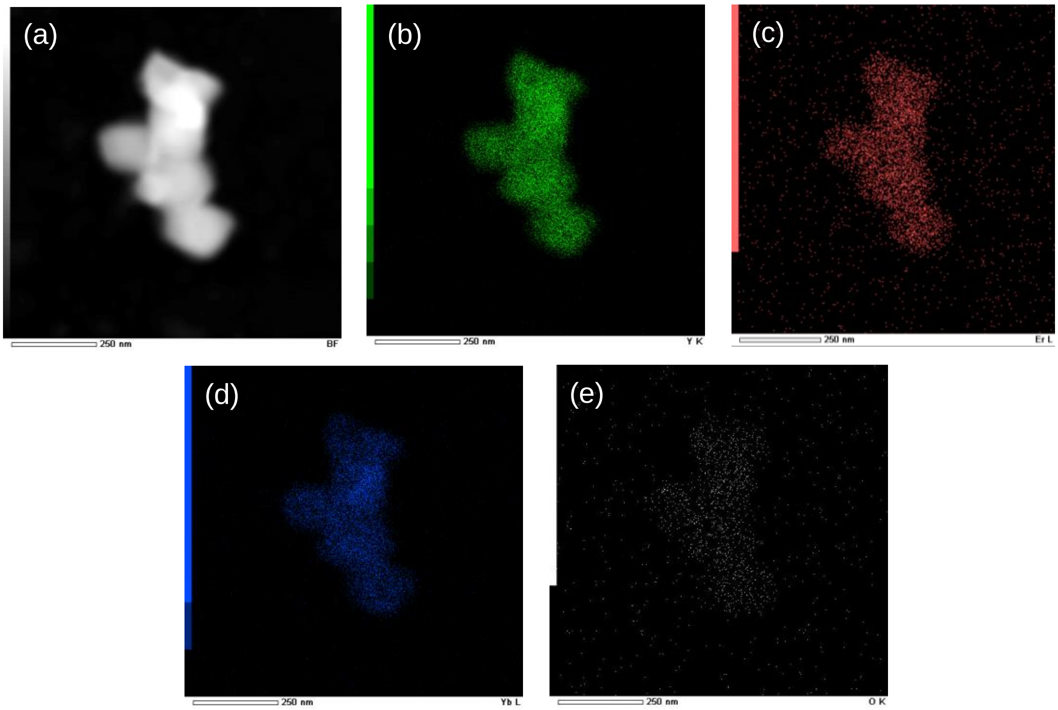

Figure 4-4. BF-STEM image and EDX mappings of the nanoparticles prepared by laser ablation in liquid: BF-STEM image (a), Y (b), Er (c), Yb (d), and O mapping (e).

Dot-like nanoparticles generated by quenching plume plasma were investigated in detail by STEM-EDX. Figure 4-4 (a) shows a TEM image of the dot-like nanoparticles. This nanoparticle was prepared by laser fluence irradiation time 15 min. Lattice fringes of the nanoparticles were observed. That is, highly crystalline nanoparticles were observed. Then, lattice spacings d of 3.06 Å were observed. This corresponded to the d_{222} lattice plane of cubic

Y_2O_3. Therefore, it was found that this dot-like nanoparticle was cubic Y_2O_3. Figure 4-4 (b) shows an STEM image of the dot-like nanoparticles. These dot-like nanoparticles were also observed in the TEM image shown in Figure 4-4 (a). Then, a line analysis of the nanoparticles shown in Figure 4-4 (b) was performed using EDX. Figures 4-4 (c), (d), and (e) show the results of this line analysis. The letters in Figure 4-4 (b) correspond to the EDX spectra shown in Figures 4-4 (c), (d), and (e). From the results of the EDX analysis, the peaks of the Y (K_α, K_β), Er ($LIII_{ab}$), and Yb (L_α) were observed. These nanoparticles were generated by quenching the plume plasma prepared by laser irradiation. It was indicated to be recrystallized to Y_2O_3, after the elements changed into the quenched plasma. From results of STEM-EDX, it was found that uniformly Er-Yb-doped Y_2O_3 nanoparticles were prepared by laser ablation in liquid.

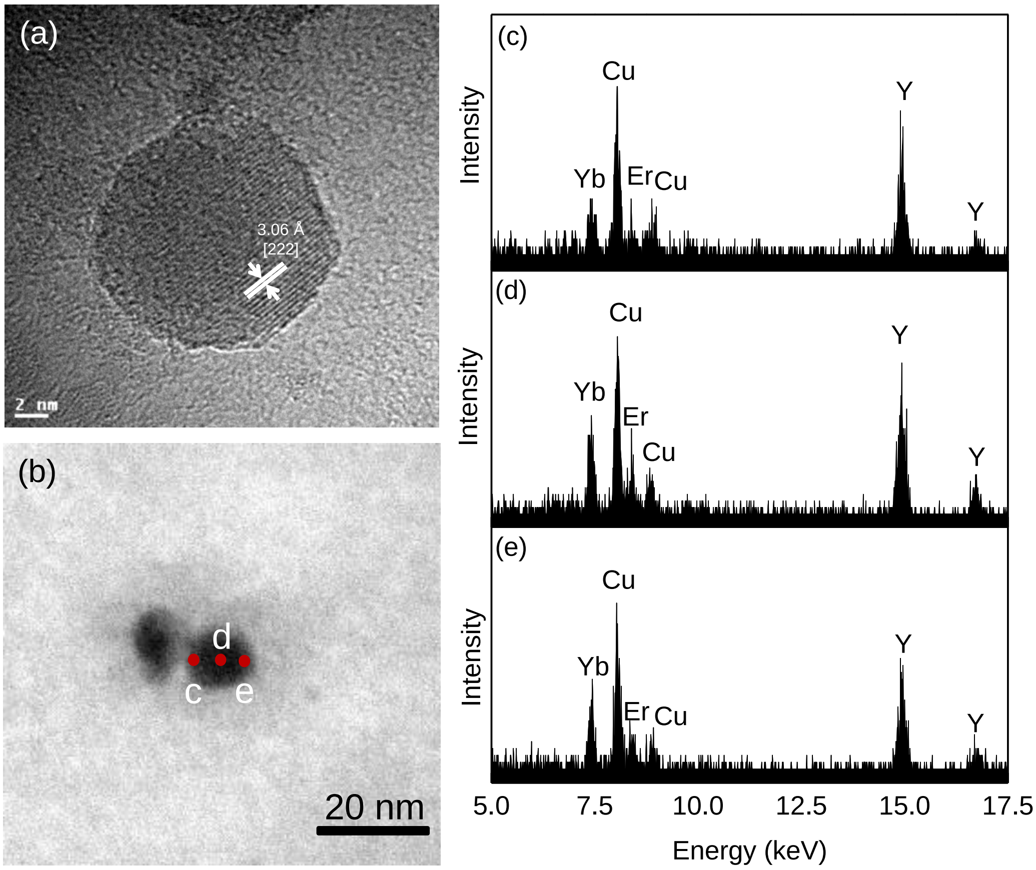

Figure 4-5. TEM image of the dot-like nanoparticles (a), STEM image of the dot-like nanoparticles (b), and line analysis of the dot-like nanoparticles by EDX (c), (d), and (e).

Also, nano-strings generated by quenching plume plasma were investigated in detail by STEM-EDX. Figure 4-5 (a) shows a TEM image of the nano-strings. These nano-strings were prepared by laser fluence irradiation time 30 min. Lattice fringes of the nano-strings were observed. That is, highly crystalline nanoparticles were observed. Then, lattice spacings *d* of

3.06 Å were observed. This corresponded to the d_{222} lattice plane of cubic Y_2O_3. Therefore, it was found that this nano-string was cubic Y_2O_3. Figure 4-4 (b) shows an STEM image of the dot-like nanoparticles. These dot-like nanoparticles were also observed in the TEM image shown in Figure 4-4(a). Then, a line analysis of the nanoparticles shown in Figure 4-4 (b) was performed using EDX. Figures 4-4 (c), (d), and (e) show the results of this line analysis. The letters in Figure 4-5(b) correspond to the EDX spectra shown in Figures 4-5(c), (d), and (e). From the results of the EDX analysis, the peaks of the Y (K_α, K_β), Er ($LIII_{ab}$), and Yb (L_α) were observed. Because, however, thickness of the nano-strings was thin, the peaks of EDX were weak. These nano-strings would be generated by quenching the plume plasma prepared by laser irradiation. It was indicated to be recrystallized to Y_2O_3, after the elements changed into the quenched plasma. From results of STEM-EDX, it was found that uniformly Er-Yb-doped Y_2O_3 nanoparticles were prepared by laser ablation in liquid.

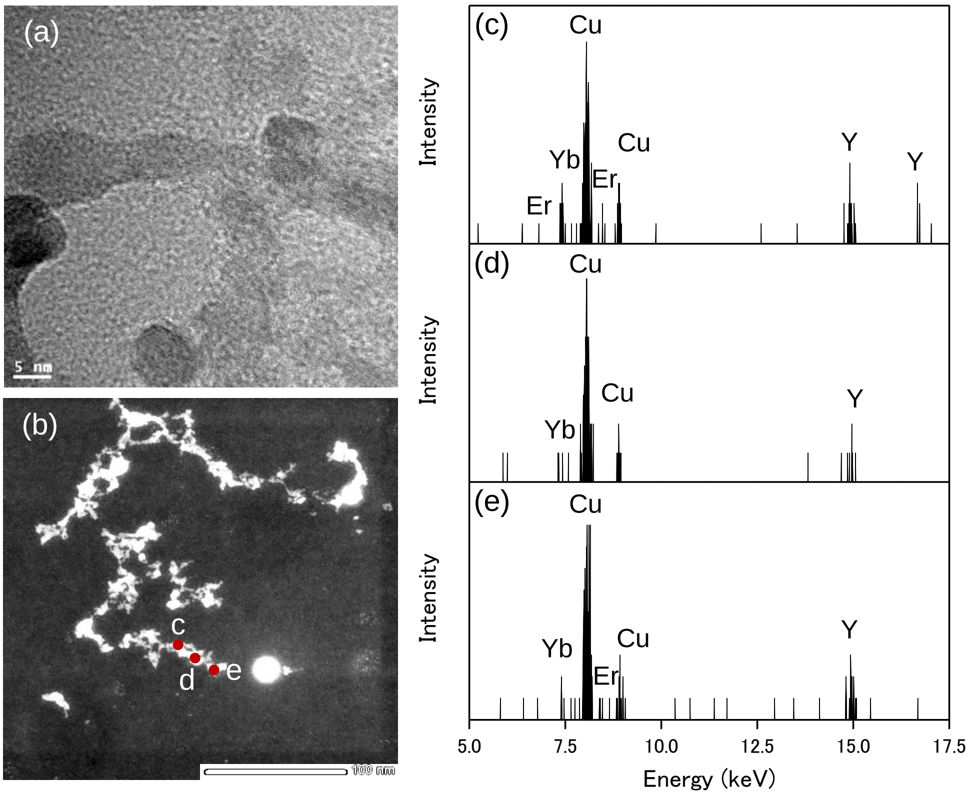

Figure 4-6. TEM image of the nano-strings (a), STEM image of the nano-strings (b), and line analysis of the dot-like nanoparticles by EDX (c), (d), and (e).

4.3.3 Composition ratio

Table 4-2 shows composition ratio of the target, ablated particles, and filtered nanoparticles. The composition ratio was measured by ICP-MS. In the ablated materials, the nanoparticles of a few tens and hundreds nm were mixed. Particle size of filtered nanoparticles is under 100 nm. So these nanoparticles would be prepared by quenching a plume plasma. The composition ratio of the ablated materials was equal or close to that of the target. On the other hand, Yb concentration of the filtered nanoparticles was more decreased than that of the target. Because ionic radius of Yb was smaller than that of the others, Yb concentration would be decreased. Table 4-3 shows ionic radius of Y, Er, and Yb [19].

Table 4-2. Composition ratio of the target, laser ablation in liquid, and filtered nanoparticles.

Elements	Target (mol%)	Laser ablation in liquid (mol%)	Filtered nanoparticles (mol%)
Y^{3+}	86.0	84.4	89.2
Er^{3+}	1.1	1.3	1.4
Yb^{3+}	12.9	14.3	9.4

Table 4-3. Ionic radius of Y, Er, and Yb [19].

Elements	Ionic radius (Å)
Y	0.892
Er	0.881
Yb	0.858

4.4 Conclusions

Y_2O_3:Er,Yb nanoparticles prepared by laser ablation in liquid maintained the high crystallinity of the target. In the irradiation time of 5 min, the prepared nanoparticles were like an amorphous from TEM image. In the irradiation time of 5 min, on the other hand, lattice fringes of the nanoparticles were observed. Further, highly crystalline nanoparticles were observed. From the line analysis by STEM-EDX, Y (K_α, K_β), Er ($LIII_{ab}$), and Yb (L_α) peaks were observed. That is, it was confirmed that uniformly Er-Yb-doped Y_2O_3 nanoparticles were prepared by laser ablation in liquid. The composition ratio was measured by ICP-MS. While the composition ratio of the ablated materials was equal or close to that of the target, Yb concentration of the filtered nanoparticles was more decreased than that of the target.

4.5 References

[1] I. Yu, T. Isobe, and M. Senta, *Journal of Physics and Chemistry of Solids* 54 (1996) 373-379.

[2] J. G. Li, X. D. Li, X. Sun, and T. Ishigaki *Journal of Physical Chemistry C* 112 (2008) 11707-11716.

[3] B. Y. Kokuoz, K. Serivalsatit, B. Kokuoz, O. Geiculescu, E. McCormick, and J. Ballatow: *Journal of American Ceramics Society*, 92 (2009) 2247

[4] J. A. Dorman, J. H. Choi, G. Kuzmanich, and J. P. Chang: *Journal of Physical Chemistry C*, 116 (2012) 10333

[5] X. Li, Q. Li, J. Wang, and J. Li, *Journal of Luminescence*, 124 (2007) 351

[6] S. Chandra, F. L. Deepak, J. B. Gruber, and D. K. Sardar: *Journal of Physical Chemistry C*, 114 (2010) 874

[7] T. Hirai, Y. Asada, I. Komasawa: *Journal of Colloid and Interface Science*, 276 (2004) 339

[8] Olivia A. Graeve, Jessica O. Corral: *Optical Materials*, 29 (2006) 24

[9] H. M. H. Fadlalla, C. C. Tang, E. M. Elssfah, and F. Shi, *Materials Chemistry and Physics* 109 (2008) 436-439.

[10] Y. H. Zhou, J. Lin, S. B. Wang, and H. J. Zhang, *Optical Materials* 20 (2002) 13-20.

[11] J. G. Li, X. D. Li, X. Sun, T. Ikegami, and T. Ishigaki, *Chemistry of Materials* 20 (2008) 2274-2281.

[12] F. Mafuné, J. Kohno, Y. Takeda, T. Kondow, H. Sawabe, *Journal of Physical Chemistry C* 104 (2000) 9111.

[13] V. Amendola and M. Meneghetti, *Physcal Chemistry Chemical Physics*, 15 (2013) 3027-3046.

[14] K. Hatanaka, M. Kawao, Y. Tsuboi, H. Fukumura, and H. Masuhara, *Journal of Applied Physics*, 82 (1997) 11.

[15] T. Sakka, K. Takatani, Y. H. Ogata, and M. Mabuchi, *Journal of Physics D: Applied Physics*, 35 (2002) 65.

[16] R. Fabbro, J. Fournier, P. Ballard, D. Devaux, and J. Virmont, *Journal of Applied Physics*, 68 (1990) 775-784.

[17] L. Berthe, A. Sollier, P. Peyre, R. Fabbro, and E. Bartnicki, *Journal of Physics D: Applied Physics*, 33 (2000) 2142-2145.

[18] T. Nunokawa, Y. Onodera, M. Hara, Y. Kitamoto, O. Odawara, and H. Wada, *Applied Surface Science*. 261 (2012) 118-122.

[19] R. D. Shannon, and C. T. Prewitt *Acta Crystallographica Section B Structural Crystallography and Crystal Chemistry* 25 (1969) 925-946.

Chapter 5 Optical properties of Y_2O_3:Er,Yb nanoparticles

5.1 Introduction

In recent years, rare-earth-doped fluorescent nano-materials have attracted much attention due to their unique optical properties and various potential applications. As potential applications, biological functioning [1,2], solar cell [3,4] and white LED [5,6] is applied. Upconversion nanoparticles are fluorescent materials that emit visible light during the irradiation of near-infrared light.[7,8] Emission mechanism has been clear that upconversion phosphors have been researched by F. Auzel et al. [9-12]

Upconversion materials have characteristics that emission energy is higher than excited energy. In general, upconversion emission is two-step process. In first step, an initial infrared photon populates an intermediate excited state. The infrared photon is accumulated in the intermediate excited state. In second step, population of the higher excited state is increased by infrared photon or an energy transfer from a neighboring ion and a visible photon is emitted. Three basic types of upconversion emission mechanism are known: (i) excited state absorption (ESA): (ii) energy transfer upconversion (ETU); and (iii) photon avalanche (PA).

ESA is emission mechanism in a single ion. It is easy to occur in low concentration of dopants. It is a two-photon process. The ground state absorption (GSA) occurs by an initial pump photon. The photon populates the intermediate excited state. After that, by the absorption of another photon from the excited intermediate state, the photon populates the upper emitting level. ETU is photon absorption involving energy transfer between neighboring ions. In the ETU process, an ion excited to the intermediate excited state by GSA is excited to the upper emitting level by transferring its energy non-radiative of a neighboring ion. PA is a different mechanism from the previous two processes. This effect is attributed to increase of the population of excitation state by cross relaxation section. That is, because of increasing the population in intermediate state of rare earth, the emission intensity is remarkably increased.

In this chapter, optical properties of Y_2O_3:Er,Yb nanoparticles prepared by laser ablation in liquid were investigated. For the application, comprehension of the optical properties is important themes. Specifically, optical properties of the target, nanoparticles prepared by laser ablation in liquid, nanoparticles filtered under 100 nm, and a single level nanoparticle were investigated.

5.2 Experimental

Preparation method of the target was as same as that in chapter 3. A laser equipment was used as same as that in chapter 3. Volume of de-ionized water and plastic cuvette were as same as that in chapter 3. Conditions of laser ablation in liquid in the preparation of the nanoparticles were as follows: laser fluence 3.61 J/cm^2 and irradiation time: 30 min. In order to investigate the optical properties of the nanoparticles generated from the quenching of the plume plasma, these nanoparticles under 100 nm were separated by using a membrane filter as same as that in chapter 4. Filtered colloidal solution was dropped on a slide glass. The slide glass was dried by vacuum oven.

Photoluminescence (PL) spectra and upconversion spectra of the target material were measured by a fluorescent spectrophotometer (Hitachi High-Technologies Co. F-7000) at room temperature. A xenon lamp and laser diode (LD, wavelength: 980 nm THORLABS, Inc. TCLDM9) were used as excitation sources for the photoluminescence and upconversion spectra measurements. To observe the upconversion spectra of the nanoparticles directly, a system with an optical microscope and a femtosecond laser (wavelength: 793 nm Spectra Physics, Tsunami, pulse width: 80 fs, repetition rate: 80 MHz) was used. To observe the nanoparticles, the upconversion colloidal solution was dropped onto a quartz glass slide and dried in air. The luminescence image of the nanoparticles was acquired by a CCD camera, and a spectrum of each nanoparticle was measured by the spectrometer simultaneously by cutting the excitation laser beam with a filter. The observation of the nanoparticles was used by SEM (Hitachi High-Technologies, S-4800). For the SEM measurements, the upconversion colloidal solution was dropped on a carbon membrane on a copper grid and the solvent was removed by drying in a vacuum oven.

5.3 Results and discussion

5.3.1 Optical properties of the target materials

The optical properties of the bulk upconversion materials were investigated. Figure 5-1(a) shows the PL spectra of the target material with an excitation wavelength of 380 nm. In the case of UV excitation, green emission ($^2H_{11/2}/^4S_{3/2} \rightarrow {}^4I_{15/2}$) was dominantly observed. No red emission ($^4F_{9/2} \rightarrow {}^4I_{15/2}$) was observed. Figure 5-1(b) shows the upconversion spectra of the target material excited by a laser diode with a wavelength of 980 nm. In the case of near-infrared excitation, both green and red emission was observed in the upconversion spectrum. Therefore, it was found that Er and Yb were doped in the Y site of the targets.

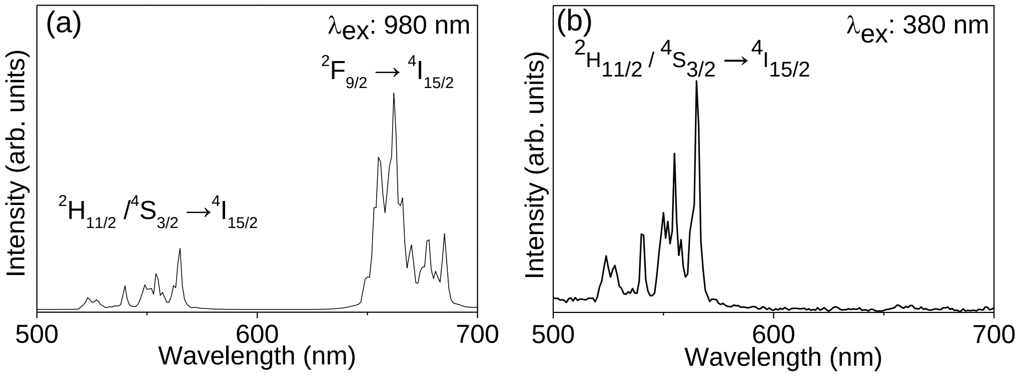

Figure 5-1. (a) PL spectra of target material, (b) upconversion spectra of target material.

Figure 5-2 (a) shows the energy level diagrams of Er^{3+} and Yb^{3+} under irradiating 980 nm LD. A red emission has been reported as follows: a 980 nm LD excites Er^{3+} from the ground state $^4I_{15/2}$ to the excited state $^4I_{11/2}$. Subsequently, a nonradioactive relaxation occurs from the $^4I_{11/2}$ level to the $^4I_{13/2}$ level. In the ESA, the photon energy of a 980 nm LD excites from the $^4I_{13/2}$ level to the $^4F_{9/2}$ level. In the ETU, the photon energy transfers from Yb^{3+} ($^2F_{5/2} \rightarrow {}^2F_{7/2}$) to the Er^{3+} ($^4I_{13/2} \rightarrow {}^4F_{9/2}$). Finally, the red emission is observed from the $^4F_{9/2} \rightarrow {}^4I_{15/2}$ transition in the Er^{3+}. Conversely, a green emission has been reported as follows: a 980 nm LD excites from the ground state $^4I_{15/2}$ to the excited state $^4I_{11/2}$. In the ESA, the photon energy of a 980 nm LD excites from the $^4I_{11/2}$ level to the $^4F_{9/2}$ in the Er^{3+} level. In the ETU, the photon energy transfers from Yb^{3+} ($^2F_{5/2} \rightarrow {}^2F_{7/2}$) to the Er^{3+} ($^4I_{11/2} \rightarrow {}^4F_{7/2}$). Subsequently, a nonradioactive relaxation occurs from the $^4F_{7/2}$ level to the $^2H_{11/2}$ level or the $^4S_{3/2}$ level. Finally, the green emission was observed in the $^2H_{11/2}/^4S_{3/2} \rightarrow {}^4I_{15/2}$ transition. Figure 5-2 (b) shows the energy level diagrams of Er^{3+} on the excitation light of 380 nm. The photon energy of a 380 nm excites from the $^4I_{13/2}$ level to the $^4G_{11/2}$ level in the Er^{3+}. The green emission is observed from the $^2H_{11/2}/^4S_{3/2} \rightarrow {}^4I_{15/2}$ transition in the Er^{3+}. Although Figure 5-2 (b) does not show the blue emission, it comes from the $^2H_{9/2} \rightarrow {}^4I_{15/2}$ transition in the Er^{3+}.

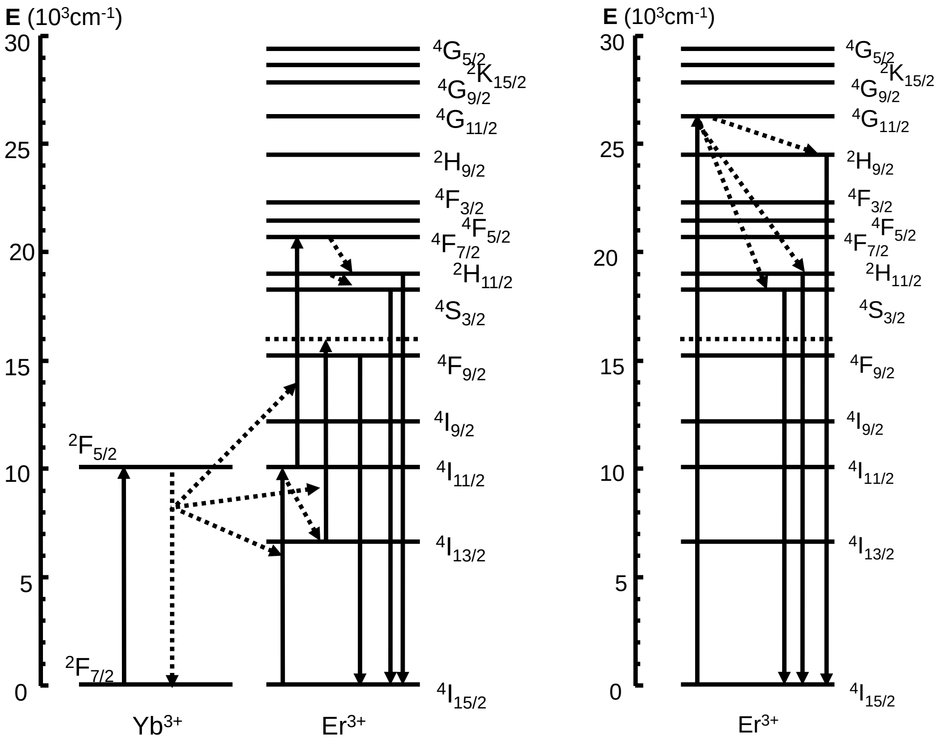

Figure 5-2. Energy level diagrams of Er^{3+} and Yb^{3+} under irradiating 980 nm LD (a) and energy level diagrams of Er^{3+} on the excitation light of 380 nm (b).

Figure 5-3 shows the red and green emission intensity as a function of the excitation light power (980 nm LD). The red and green emission intensity increased with increasing excitation light power. In general, the emission intensity increased next [9, 12].

$$I_{em} \propto P_{ex}^{\ n} \qquad (5\text{-}1)$$

where I_{em} denotes the emission intensity; P_{ex}, the excitation power of a laser diode; and n, the number of photons. However, the emission intensity was dramatically increased at an excitation power of 100 mW in both red and green emission. Because the power of 980 nm LD linearly increased with increasing of the current, and vice versa (Figure S1), dramatic increase of the emission intensity would not depend on 980 nm LD. This effect was called photon avalanche. This mechanism is explained in [13]–[15]. The photon avalanche effect is a phenomenon that occurs in the cross-relaxation section.

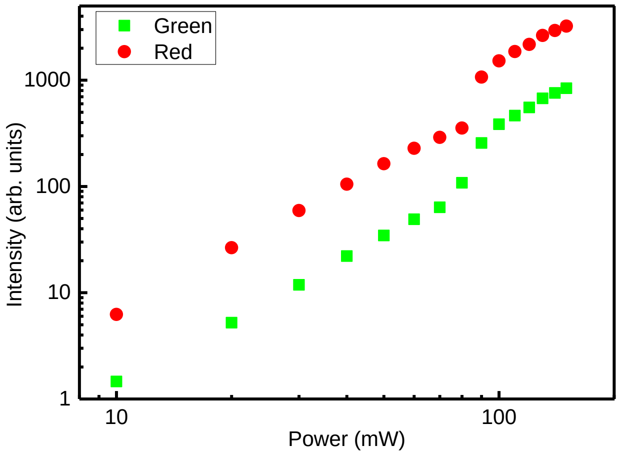

Figure 5-3. Red (660 nm) and green (565 nm) emission intensity in the target as a function of the excitation power of 980 nm LD.

Table 5-1 shows slopes in the red and green emission intensity of targets as a function of the excitation power. In the excitation power under 90 mW, the slopes were 1.96 and 2.02 in the red and green emission, respectively. In the excitation power over 90 mW, the slopes were 2.25 and 2.12 in the red and green emission, respectively. That is, target materials emitted light by absorbing about two photons.

Table 5-1. Slope in the red and green emission intensity of targets as a function of the excitation power.

	Slope under 80 mW	Slope above 90 mW
Red emission	1.96	2.25
Green emission	2.02	2.12

Figure 5-4 (a) shows the photon avalanche process in the red emission. In general, the red intensity is emitted by the absorbance of $^4I_{15/2} \rightarrow {}^4I_{11/2}$ and $^4I_{13/2} \rightarrow {}^4F_{9/2}$ (excited-state absorption: ESA). In the three photons process, the absorbance of $^4I_{15/2} \rightarrow {}^4I_{11/2}$, $^4I_{13/2} \rightarrow {}^4F_{9/2}$, and $^4F_{9/2} \rightarrow {}^4H_{9/2}$ occurs. However, a cross-relaxation section between $^4H_{9/2} \rightarrow {}^4F_{9/2}$ and $^4I_{13/2} \rightarrow {}^4F_{9/2}$ is formed. Then, the electron population in the $^4F_{9/2}$ band is increased by the formation of the cross relaxation section and the absorbance of $^4F_{9/2} \rightarrow {}^4I_{13/2}$. Finally, red light is emitted by $^4F_{5/2} \rightarrow {}^4I_{15/2}$. Therefore, an increase in this electron population causes a dramatic increase in the emission intensity. Figure 5-4 (b) shows the photon avalanche process in the green emission. As well as red emission, a cross-relaxation section causes the photon avalanche of the green emission. In the green emission, a cross-relaxation section between $^4H_{9/2} \rightarrow {}^4S_{3/2}$ and $^4I_{9/2} \rightarrow$

$^4S_{3/2}$ is generated. Therefore, this electron population increases in $^4S_{3/2}$ of Er^{3+} energy level. As a result, the green emission is increased by $^4S_{3/2} \rightarrow {^4I_{15/2}}$.

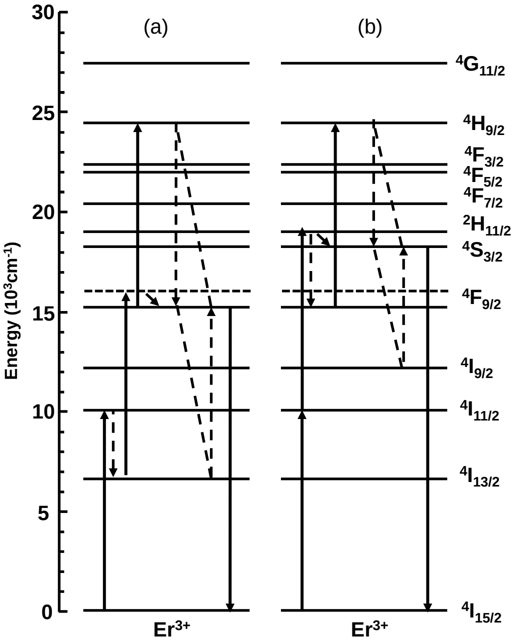

Figure 5-4. General photon avalanche process in red (660 nm) (a) and green (565 nm) (b) emission of energy-level diagram of Er^{3+} ions in Y_2O_3.

Figure 5-5 (a) shows the upconversion spectra of the target material when excited by a femtosecond laser with a wavelength of 793 nm. The PL intensity significantly depends on the excitation wavelength of the femtosecond laser and was highest at 793 nm around 800 nm. The upconversion spectrum of the femtosecond laser (793 nm) was almost the same as that of LD (980 nm) as shown in Figure 5-1(a). No appreciable wavelength shift was observed. Figure 5-5 (b) shows intensity of green (565nm) and red (660 nm) emission as a function of excitation power. As excitation power increased, both intensity of green (565nm) and red (660 nm) emission increased. The intensity ratio of green emission to red emission as a function of excitation power is shown in Figure 5-5 (c). An increase in excitation power causes an increase in this ratio. A similar tendency was observed previously because higher excitation power increased the population of higher green levels ($^2H_{11/2}$/$^4S_{3/2}$). [17]

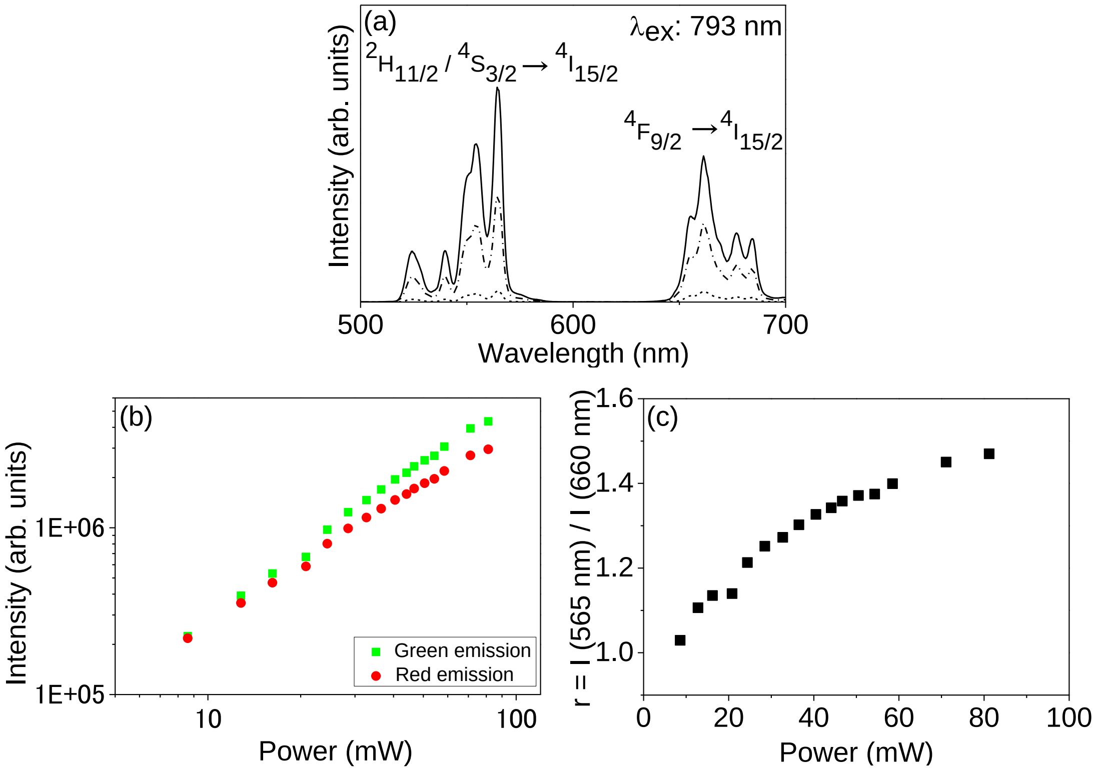

Figure 5-5. (a) Upconversion spectra of target material. Laser power: solid line 81 mW, chain line 44 mW, dotted line 9 mW, (b) Intensity of green (565 nm) and red (660 nm) emission as a function of excitation power, and (c) Intensity ratio of green emission (565 nm) to red emission (660 nm) as a function of excitation power.

Figure 5-6 shows an energy level diagram of Er^{3+}.The mechanism of emission by excitation around 800 nm is reported by [18]. A red emission has been reported as follows: a 800 nm femtosecond laser excites Er^{3+} from the ground state $^4I_{15/2}$ to the excited state $^4I_{9/2}$. Subsequently, a nonradioactive relaxation occurs from the $^4I_{9/2}$ level to the $^4I_{13/2}$ level. The photon energy of a 800 nm femtosecond laser excites from the $^4I_{13/2}$ level to the $^2H_{11/2}$ level. A nonradioactive relaxation occurs from the $^2H_{11/2}$ level to the $^4F_{9/2}$ level. Finally, the red emission is observed from the $^4F_{9/2} \rightarrow {}^4I_{15/2}$ transition in the Er^{3+}. Conversely, a green emission has been reported as follows: as well as red emission, a 800 nm femtosecond laser excites Er^{3+} from the ground state $^4I_{15/2}$ to the excited state $^4I_{9/2}$. Subsequently, a nonradioactive relaxation occurs from the $^4I_{9/2}$ level to the $^4I_{13/2}$ level. The photon energy of a 800 nm femtosecond laser excites from the $^4I_{13/2}$ level to the $^2H_{11/2}$ level. Finally, the green emission was observed in the $^2H_{11/2}/^4S_{3/2} \rightarrow {}^4I_{15/2}$ transition.

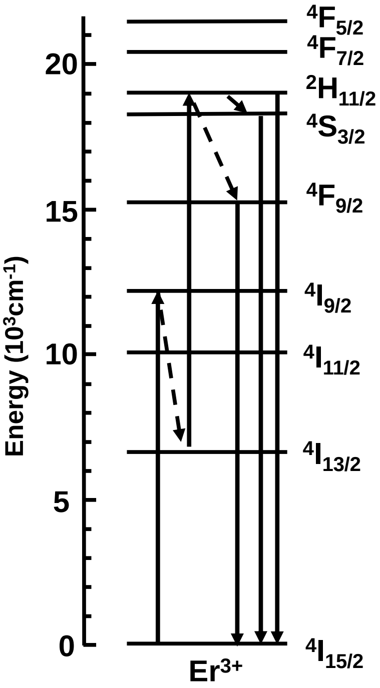

Figure 5-6. An energy level diagram of Er^{3+} under excitation light of 800 nm.

5.3.2 Effect of the laser fluence

Figure 5-7 (a) shows the upconversion spectra of the nanoparticles prepared by varying the laser fluence. The observation of green ($^2H_{11/2}$/ $^4S_{3/2} \rightarrow {}^4I_{15/2}$) and red ($^4F_{9/2} \rightarrow {}^4I_{15/2}$) fluorescence of Er^{3+} was confirmed. Figure 5-7 (b) shows the fluorescent intensity as a function of the laser fluence. It was confirmed that the fluorescent intensity increased with increasing the laser fluence. The size of the primary particle only slightly changed as a result of altering the energy density as shown in Figure 3-3. One reason for the increase in the fluorescent intensity could be a reduction in the surface defects by the aggregated particles due to the passivation of the surface defects of nanoparticles [18,19]. However, the fluorescent intensity would be increased primarily because the number of the nanoparticles increased with the increasing the laser fluence (Figure 3-10).

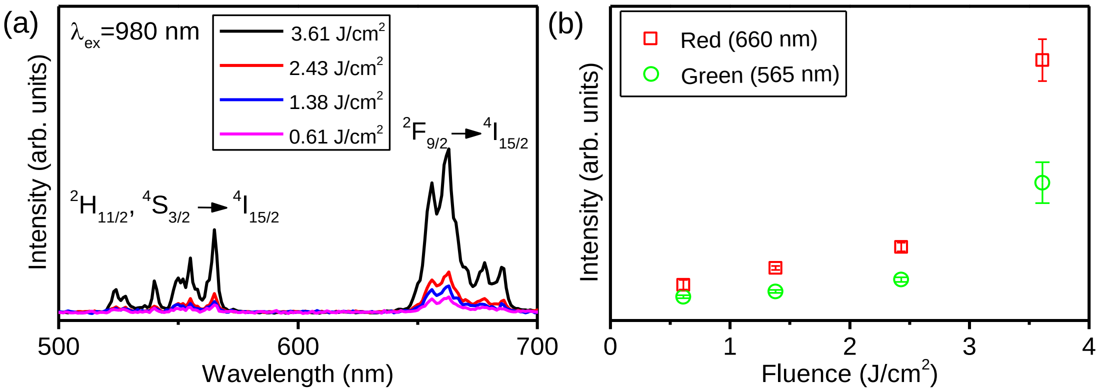

Figure 5-7. Upconversion spectra of the prepared nanoparticles on the various laser fluence (a) and fluorescent intensity as a function of the laser fluence (b).

5.3.3 Effect of the irradiation time

Figure 5-8 (a) shows the upconversion spectra of the nanoparticles prepared by varying irradiation times of laser. The observation of green ($^2H_{11/2}/^4S_{3/2} \rightarrow {}^4I_{15/2}$) and red ($^4F_{9/2} \rightarrow {}^4I_{15/2}$) fluorescence of Er^{3+} was confirmed as well as dependence of the laser fluence. Figure 5-8 (b) shows the fluorescent intensity as a function of the irradiation time. It was confirmed that the fluorescent intensity increased with passing the irradiation time. The size of the primary particle only slightly changed as a result of altering the irradiation time as shown in Figure 3-12. One reason for the increase in the fluorescent intensity could be a reduction in the surface defects by the aggregated particles due to the passivation of the surface defects of nanoparticles. However, the fluorescent intensity would be increased primarily because the number of the nanoparticles increased with the increasing the irradiation time.

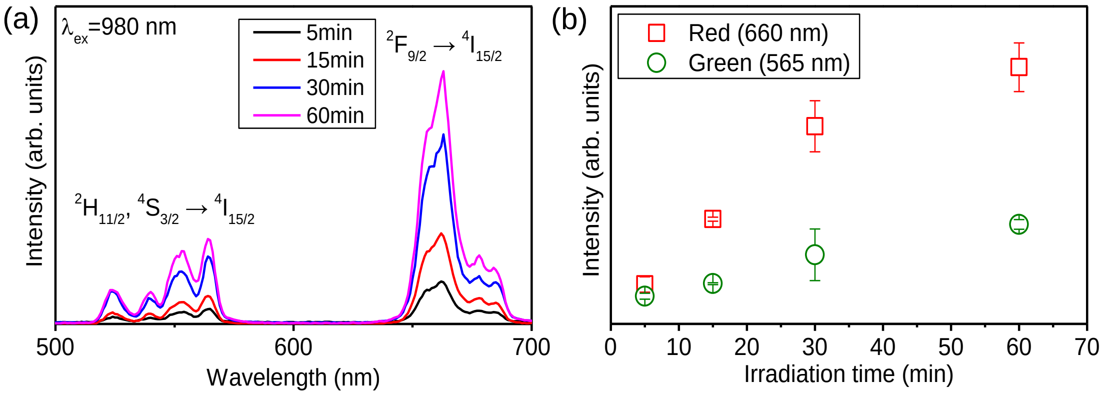

Figure 5-8. Upconversion spectra of the prepared nanoparticles on the various irradiation times of laser (a) and fluorescent intensity as a function of the irradiation time (b).

5.3.4 Filtered nanoparticles

The optical properties of the filtered nanoparticles generated from the quenching of the plume plasma were investigated. Figure 5-9 shows the upconversion spectrum of the filtered nanoparticles upon irradiation with 980 nm LD. The red ($^2F_{9/2} \rightarrow {}^4I_{15/2}$) and green ($^2H_{11/2}/^4S_{3/2} \rightarrow {}^4I_{15/2}$) emissions were observed in the filtered nanoparticles as well as the target (Figure 5-1). It was found that Er and Yb were doped in the Y site of the targets.

Compared to the emission intensity of the target, the emission intensity of nanoparticles was lower than that of the target. In general, the specific surface area of nanoparticles was increased more than that of the bulk. When the specific surface area was increased, the amount of absorption of OH^- and CO_3^{2-} increased. In particular, when water was irradiated with pulsed laser, OH radicals were generated [20, 21]. It was easy to absorb OH on the surface of the nanoparticles prepared by laser ablation in liquid. When molecules with high vibration energy, such as OH^- and CO_3^{2-}, absorbed on the surface of the nanoparticles, the thermal relaxation rate increased. As a result, the emission intensity decreased [22].

Compared to the emission intensity of the target, in emission intensity of the nanoparticles, red intensity ($^2F_{9/2} \rightarrow {}^4I_{15/2}$) was likely to be higher than green intensity ($^2H_{11/2}/^4S_{3/2} \rightarrow {}^4I_{15/2}$). That is, it was found that the red intensity ratio of the nanoparticles was higher than that of the targets. The amount of absorption of OH^- and CO_3^{2-} were increased by increase of specific surface area. The thermal relaxation rate was increased by OH phonon. That is, the thermal relaxation rate of $^4I_{11/2} \rightarrow {}^4I_{13/2}$ in Er was a rate-limiting. As a result, the red intensity ratio in the nanoparticles would be higher than that in the targets [23].

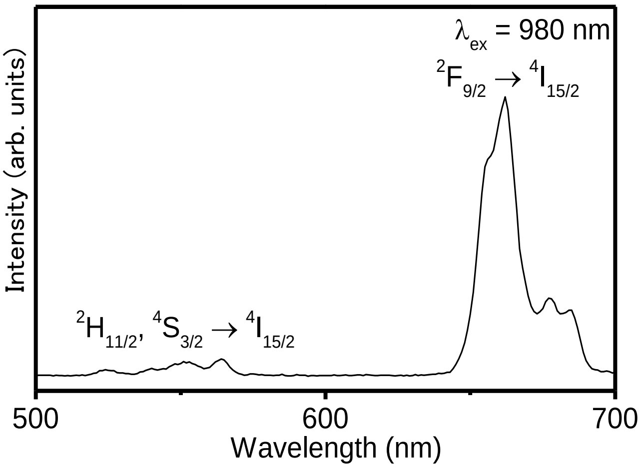

Figure 5-9. Upconversion spectrum of the filtered nanoparticles upon irradiation with 980 nm LD.

Also, the prepared nanoparticles were emitted by the same mechanism in figure 5-2. First, the red emission ($^2F_{9/2} \rightarrow {}^4I_{15/2}$) was considered. Upon irradiation with 980 nm LD, $^2F_{7/2} \rightarrow {}^2F_{5/2}$ of Yb and $^4I_{15/2} \rightarrow {}^4I_{11/2}$ of Er were excited. The energy transfer to Er happened because of the relaxation of Yb. Then, non-radiative relaxation of $^4I_{11/2} \rightarrow {}^4I_{13/2}$ occurred in Er. $^4I_{13/2} \rightarrow {}^4F_{9/2}$ of Er was excited by the irradiation with 980 nm LD and the energy transfer of Yb. Thereafter, the red emission happened by backing to the ground state ($^2F_{9/2} \rightarrow {}^4I_{15/2}$). Second, the green emission ($^2H_{11/2}/^4S_{3/2} \rightarrow {}^4I_{15/2}$) was considered. Upon irradiation with 980 nm LD, $^4I_{15/2} \rightarrow {}^4I_{11/2}$ of Er was excited. $^4I_{11/2} \rightarrow {}^4F_{7/2}$ of Er was excited by the irradiation of 980 nm LD and the energy transfer of Yb. The non-radiative relaxation of $^4F_{7/2} \rightarrow {}^2H_{11/2}$ and $^4F_{7/2} \rightarrow {}^4S_{3/2}$ in Er occurred. Then, the green emission occurred due to backing to the ground state ($^2H_{11/2}/^4S_{3/2} \rightarrow {}^4I_{15/2}$).

Figure 5-10 shows the red and green emission intensity as a function of the excitation light power (980 nm LD). In the prepared nanoparticles, the emission intensity increased with increasing excitation light power as well as target (Figure 5-3). The emission intensity was dramatically increased at an excitation power of 90 mW. Further, this phenomenon was also observed in the case of the green intensity. This effect was called photon avalanche. This mechanism is explained in [13]–[15]. The photon avalanche effect is a phenomenon that occurs in the cross-relaxation section. This mechanism was described in section 5.3.1

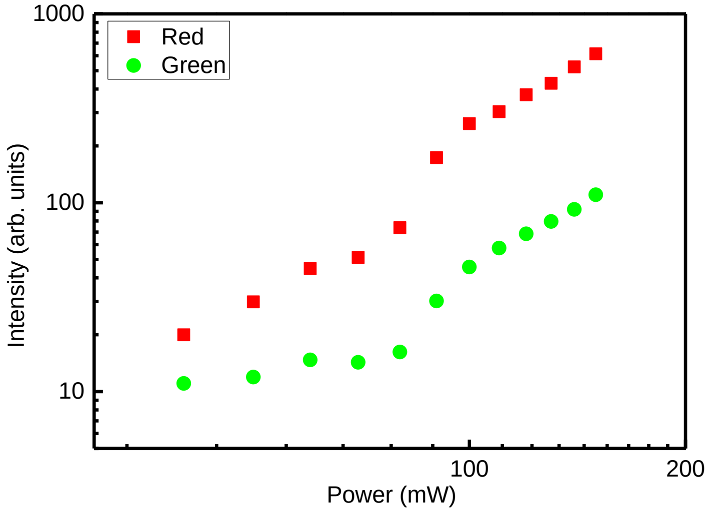

Figure 5-10 Red (660 nm) and green (565 nm) emission intensity as a function of the excitation power of 980 nm LD: target (a) and nanoparticles (b).

Table 5-2 shows slopes in the red and green emission intensity of nanoparticles as a function of the excitation power. In the excitation power under 80 mW, the slopes were 1.83 in the red emission. In the excitation power over 90 mW, the slopes were 2.38 and 2.33 in the red and green emission, respectively. That is, nanoparticles emitted light by absorbing about two photons. However, the slope of the excitation power under 80 mW in green emission was much lower than 2 (the value was 0.55). Because the green intensity of nanoparticles was lower, S/N ratio wouldn't be known.

Table 5-2. Slope in the red and green emission intensity of nanoparticles as a function of the excitation power.

	Slope under 80 mW	Slope over 90 mW
Red emission	1.83	2.38
Green emission	0.55	2.33

5.3.5 Single level nanoparticle spectroscopy

Figure 5-11(a) shows an SEM image of the Y_2O_3:Er,Yb nanoparticles. Most of the nanoparticles had a spherical shape, although there were a few that had a polyhedral shape, and a particle size of a few hundreds nm. Additionally, the nanoparticles showed some slight aggregation. The optical microscope image of the Y_2O_3:Er,Yb nanoparticles is shown in Figure 5-11(b).

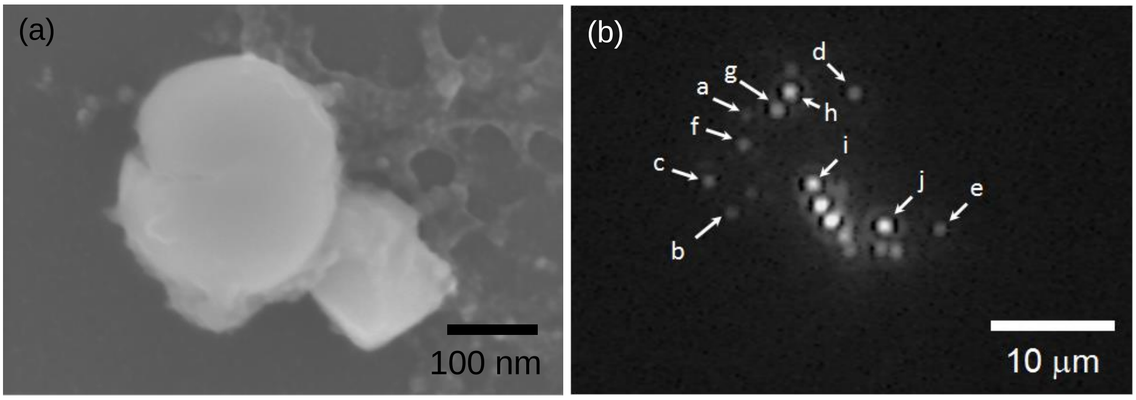

Figure 5-11 SEM image of Y_2O_3:Er,Yb nanoparticles (a), Optical microscope image of Y_2O_3:Er,Yb nanoparticles with excitation from a femtosecond laser (b).

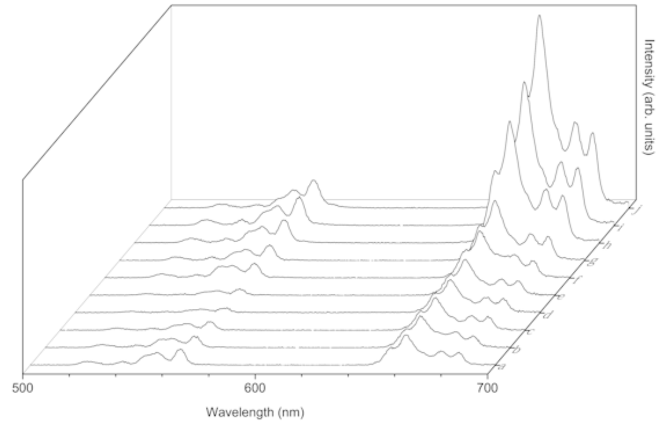

Figure 5-12. Upconversion spectra of each Y_2O_3:Er,Yb nanoparticle in Figure 5-11 (b).

Nanoparticles on a quartz glass slide were excited by a focused femtosecond laser beam. Each emission size was significantly larger than the size of a nanoparticle because of the scattering of light. There was a large deviation in the emission intensity for each nanoparticle, which could be due to the difference of crystallinity, size and/or surface defects of each nanoparticle. When excited by a femtosecond laser with a wavelength of 793 nm, the upconversion spectra of each nanoparticle are shown in Figure 5-12; these spectra were collected by usage of an aperture to eliminate the emission of the other nanoparticles. Compared to the upconversion spectra of the target material under irradiation of 793 nm femtosecond laser as excitation light, as shown in Figure 5-5(a), the intensity ratio of green emission ($^2H_{11/2}/^4S_{3/2} \rightarrow {}^4I_{15/2}$) to red emission ($^2F_{9/2} \rightarrow {}^4I_{15/2}$) in the nanoparticles was significantly smaller, with a value of 0.27 ± 0.12. Fragmentation by laser ablation in liquid would lead to a decrease in the intensity ratio of green emission to red emission, according to the following explanation.[17, 24] As mentioned above, the nonradiative relaxation processes of large energy gaps ($^4I_{9/2} \rightarrow {}^4I_{13/2}$, $^2H_{11/2}/^4S_{3/2} \rightarrow {}^4F_{9/2}$) are included in the red emission process. In general, nonradiative relaxation processes prevent emission. Therefore, the red emission ($^2F_{9/2} \rightarrow {}^4I_{15/2}$) was decreased in the bulk material. The rate of phonon emission, w, is expressed by the following equation[25, 26]:

$$w \propto \exp\left(-k\frac{\Delta E}{h\nu_{\max}}\right) \tag{5-2}$$

where ΔE is energy gap to the nearest lower level and $h\nu_{\max}$ is maximum energy of phonon. Nanoparticles have a large specific surface area, and functional groups such as OH^- and CO_3^{2-}, which have high vibrational modes, tend to adhere to this surface.[7, 8] This adhesion increases $h\nu_{\max}$ and increases the rate of phonon emission. Therefore, the nonradiative relaxation processes ($^4I_{9/2} \rightarrow {}^4I_{13/2}$, $^2H_{11/2}/^4S_{3/2} \rightarrow {}^4F_{9/2}$) would be bridged, and the population of $^4F_{9/2}$ would increase, leading to an increase in the observed red emission. Also, nonradiative transition can be considered by Franck-Condon factor [27].

5.4 Conclusions

Y_2O_3:Er,Yb upconversion nanoparticles prepared by laser ablation in liquid emitted red ($^2F_{9/2} \rightarrow {}^4I_{15/2}$) and green ($^2H_{11/2}/{}^4S_{3/2} \rightarrow {}^4I_{15/2}$) under irradiating 980 nm LD. As laser fluence or irradiation time was increased, emission intensity was increased. By effects of the productivity and particle size of the prepared nanoparticles, emission intensity would be increased.

The nanoparticles prepared by laser ablation in liquid under 100 nm were separated by using a membrane filter. Also, the filtered nanoparticles emitted red ($^2F_{9/2} \rightarrow {}^4I_{15/2}$) and green ($^2H_{11/2}/{}^4S_{3/2} \rightarrow {}^4I_{15/2}$). The emission intensity of the filtered nanoparticles was lower than that of target. It was suggested that the intensity ratio of red to green emission of the filtered nanoparticles was increased, compared to that of target. Nonradiative transitions in the red emission process would effectively be bridged by an increase in the multiphonon relaxation through surface groups such as OH^- and CO_3^{2-}. Further, it is found that these nanoparticles had a photon avalanche process.

Single level nanoparticle spectra were investigated by a femtosecond laser system with an optical microscope. In these spectra, the intensity of the red emission ($^2F_{9/2} \rightarrow {}^4I_{15/2}$) was stronger than that of the green emission ($^2H_{11/2}/{}^4S_{3/2} \rightarrow {}^4I_{15/2}$). As well as the filtered nanoparticles, because groups such as OH^- and CO_3^{2-} in the surface of the coarse nanoparticle were absorbed, the intensity ratio of red to green emission was increased.

5.5 References

[1] J. Zhou, Z. Liu, and F. Li, *Chemical Society Reviews* 41 (2012) 1323-1349.

[2] H. S. Qian, H. C. Guo, P. C-L. Ho, R. Mahendran, and Y. Zhang, *Small*, 5 (2009) 2285-2290.

[3] B. M. Ende, L. Aartsa, and A. Meijerink, *Physical Chemistry Chemical Physics*, 11 (2009) 11081-11095.

[4] J. L. Ferrari, K. O. Lima, E. Pecoraro, R. A. S. Ferreira, L. D. Carlos, and R. R. Gonçalves, *Journal of Materials Chemistry*, 22 (2012) 9901-9908.

[5] L. W. Yang, L. H. Han, Y. Y. Zhang, and J. X. Zhang, *Journal of Physical Chemistry C,* 113 (2009) 18995-18999.

[6] X. R. Hou, S. M. Zhou, T. T. Jia, H. Jia, H. Lin, and H. Teng, *Journal of Alloys and Compounds* 509 (2011) 2793-2796.

[7] F. Vetrone, J. C. Boyer, J. A. Capobianco, A. Speghini, and M. Bettinelli, *Journal of Applied Physics* 96 (2004) 661-667.

[8] J. A. Capobianco, F. Vetrone, T. Alesio, G. Tessari, M. Bettinelli, *Physical Chemistry Chemical Physics* 2 (2000) 3203-3207.

[9] F. Auzel, *Chemical Reviews* 104 (2004) 139-173

[10] F. Auzel, *F. C. R. Acad. Sci.* (Paris) 262 (1966) 1016

[11] F. Auzel, *F.C.R. Acad. Sci.* (Paris) 263B (1966) 819

[12] F. Auzel, *Journal of Luminescence,* 31-32 (1984) 759-761.

[13] J. S. Chivian, W. E. Case, and D. D. Eden, *Applied Physics Letters*, 35 (1979) 124-125.

[14] M. F. Joubert, S. Guy, and B. Jacquie, *Physical Review B,* 48 (1993) 10031-10037.

[15] M. F. Joubert: *Optical Materials* 11 (1999) 181-203.

[16] H. Song, B. Sun, T. Wang, S. Lu, L. Yang, B. Chen, X. Wang and X. Kong, *Solid State Communications* 132 (2004) 409-413.

[17] J. A. Capobianco, G. Prevost, P. P. Proulx, P. Kabro and M. Bettinelli, *Optical Materials* 6 (1996) 175-184.

[18] Y. Wang, L. Tu, J, Zhao, Y. Sun, X. Kong, and H. Zhang, *Journal of Physical Chemistry C* 113 (2009) 7164-7169.

[19] F. Wang, J. Wang, and X. Liu, *Angewandte Chemie International Edition* 49 (2010) 7456-7469.

[20] X. W. Fang, G. Mark, and C. Y. Sonntag, *Ultrasonics Sonochemistry,* 3 (1996) 57-63.

[21] S. Kanazawa, H. Kawano, S. Watanabe, T. Furuki, S. Akamine, R. Ichiki, T. Ohkubo, M. Kocik, and J. Mizeraczyk. *Plasma Sources Science Technology,* 20 (2011) 034010

[22] F. Vetrone, J. C. Boyer, J. A. Capobianco, A. Speghini, and M. Bettinelli, *Chemistry of*

Materials, 15 (2003) 2737-2743.

[23] T. Nunokawa, Y. Onodera, H. Kobayashi, T. Asahi, O. Odawara, and H. Wada, *Journal of Ceramic Processing Research* 14 (2013) S1-4.

[24] T. Hirai and T. Orikoshi, *Journal of Colloid and Interface Science* 273 (2004) 470-477.

[25] L. A. Riseberg and H. W. Moos, *Physical Review* 174 (1968) 429-438.

[26] J. M. F Dijk and M. F. H. Schuurmans *Journal of Chemical Physics* 78 (1983) 5317-5323.

[27] Y. Onodera, T. Nunokawa, O. Odawara, and H. Wada, *Journal of Luminescence* 137 (2013) 220-224.

Chapter 6 General conclusions and perspectives

6.1 General conclusions

In this dissertation, Y_2O_3:Er,Yb nanoparticles, which have upconversion optical properties, prepared by using laser ablation in liquid. The Y_2O_3:Er,Yb nanoparticles have potential of various applications in biological functioning and device. Morphology, crystallinity, and optical properties of the prepared nanoparticles were investigated. These investigations are important for applications of nano-phosphor. In this doctoral dissertation, this study has been performed in three objectives. As a conclusion in this doctoral dissertation, these results were summarized as follows.

First, morphology of Y_2O_3:Er,Yb nanoparticles were investigated by changing laser fluence and irradiation time. Y_2O_3:Er,Yb nanoparticles were successfully prepared by laser ablation in liquid. The coarse nanoparticles were observed by SEM. When targets are irradiated with a laser, a plume plasma is prepared on the surface of the target. High pressure of shock wave was generated by counteraction of plume plasma. After quenching the plasma plume, a cavitation bubble is generated. Then, a shock wave is generated by counteraction of the cavitation bubble. The coarse nanoparticles would be prepared by the shock wave. The coarse nanoparticles depend on particle of target surface. Conversely, the fine nanoparticles were prepared by quench of the plume plasma. The number of the fine nanoparticles was increased with increasing laser fluence or irradiation time. As a result, nano-strings would be prepared by increasing the number of the fine nanoparticles. Nano-string would form network structure by heat of the laser. Therefore, preparation mechanism in ceramics nano-phosphor by laser ablation in liquid could be suggested.

Secondly, crystallinity and distribution of the dopants in nanoparticles prepared by laser ablation in liquid were investigated. Y_2O_3:Er,Yb nanoparticles prepared by laser ablation in liquid maintained the high crystallinity of the target by XRD. In the TEM image, lattice fringes of the nanoparticles were observed in both the dot-like nanoparticles and the nano-strings. Further, highly crystalline nanoparticles were observed. From composition analysis by STEM-EDX, Y (K_α, K_β), Er ($LIII_{ab}$), and Yb (L_α) peaks were observed. That is, it was confirmed that uniformly Er-Yb-doped Y_2O_3 nanoparticles were prepared by laser ablation in liquid. The composition ratio was measured by ICP-MS. The composition ratio of the prepared nanoparticles was equal or close to that of the target. Therefore, by laser ablation in liquid, preparation of highly crystalline nanoparticles that dopant existed in host material was successful.

Finally, optical properties of Y_2O_3:Er,Yb nanoparticles prepared by laser ablation in liquid were investigated. The upconversion nanoparticles prepared by laser ablation in liquid emitted red ($^2F_{9/2} \rightarrow {}^4I_{15/2}$) and green ($^2H_{11/2}/{}^4S_{3/2} \rightarrow {}^4I_{15/2}$) under irradiating 980 nm LD. As laser fluence or irradiation time was increased, emission intensity was increased. By effects of the productivity and particle size of the prepared nanoparticles, emission intensity would be increased.

The nanoparticles prepared by laser ablation in liquid under 100 nm were separated by using a membrane filter. Also, the filtered nanoparticles emitted red ($^2F_{9/2} \rightarrow {}^4I_{15/2}$) and green ($^2H_{11/2}/{}^4S_{3/2} \rightarrow {}^4I_{15/2}$). The emission intensity of the filtered nanoparticles was lower than that of target. It was suggested that the intensity ratio of red to green emission of the filtered nanoparticles was increased, compared to that of target. Nonradiative transitions in the red emission process would effectively be bridged by an increase in the multiphonon relaxation through surface groups such as OH^- and CO_3^{2-}. Further, it is found that the prepared nanoparticles had a photon avalanche process.

Single level nanoparticle spectra were investigated by a femtosecond laser system with an optical microscope. In these spectra, the intensity of the red emission ($^2F_{9/2} \rightarrow {}^4I_{15/2}$) was stronger than that of the green emission ($^2H_{11/2}/{}^4S_{3/2} \rightarrow {}^4I_{15/2}$). As well as the filtered nanoparticles, because groups such as OH^- and CO_3^{2-} in the surface of the coarse nanoparticle were absorbed, the intensity ratio of red to green emission was increased.

From these results, optical properties of the nanoparticles prepared for applications, such as bio-imaging, and spectral converter for solar cell, were successfully investigated.

6.2 Perspectives

Y_2O_3:Er,Yb nanoparticles were successfully prepared by laser ablation in liquid. Cavitation bubble generated by laser ablation in liquid scatters laser light. Therefore, productivity of nanoparticles is decreased. In order to increase the productivity of the nanoparticles, it will be necessary to rotate the target. Nano-strings were often observed. Because a nanosecond laser that is comparatively weak pulse is used, nano-strings will be generated by laser ablation in liquid. To prevent the nano-string from forming, pico or femto second laser that is strong pulse should be used. In order to form mono-dispersive nanoparticles, it will be necessary to choice the solvents, such as surfactants and polymer. Emission intensity of nano-phosphor is decreased by the surface defect. In order to prevent emission intensity from decreasing, surface modifications, such as a silica coat, will be necessary. No surface modifications of the upconversion nanoparticles prepared by laser ablation in liquid have been carried out yet. Also, the potential as applications should be researched. Research of upconversion nanoparticles have been often carried out for biomaterials such as bio-imaging and PDT. However, no applications of the upconversion nanoparticles prepared by laser ablation in liquid have been carried out. Therefore, this study will be important for bio-application.

Appendix data

A. 1 Current as a function of the power in 980 nm LD

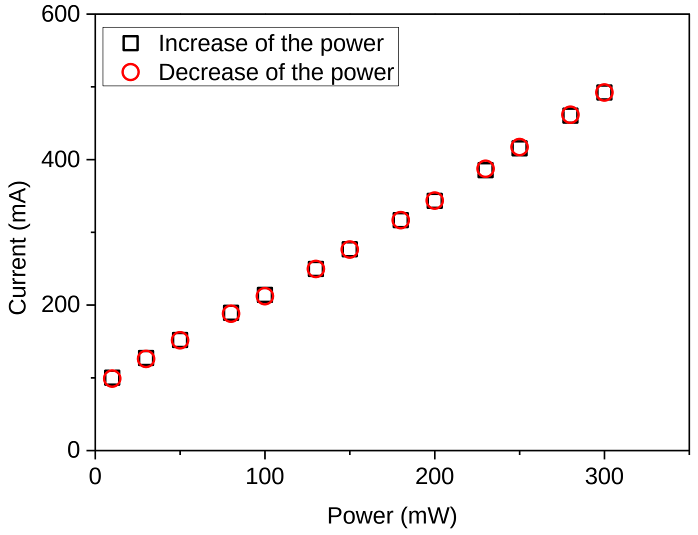

Figure A1. Current as a function of the power in 980 nm LD.

Figure A1 shows current as a function of the power in 980 nm LD. The power in 980 nm LD was linearly increased with increasing current, and vice versa. That is, no hysteresis was observed.

A. 2 UV-Vis spectroscopy

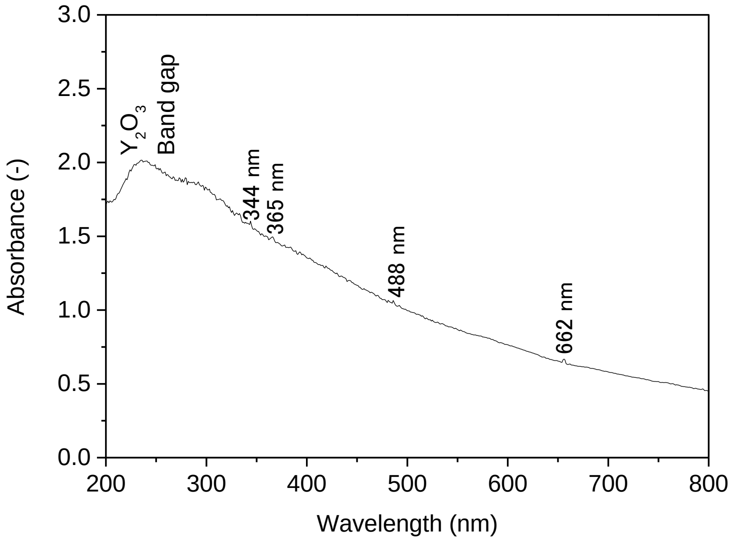

Figure A2. UV-Vis spectrum in Y_2O_3:Er,Yb nanoparticles prepared by laser ablation in liquid.

Figure A2 shows UV-Vis spectrum in Y_2O_3:Er,Yb nanoparticles prepared by laser ablation in liquid. Broad peak around 230 nm was observed. This peak would be derived from a band gap of Y_2O_3. Also, some smaller peaks of 344, 365, 488, and 662 nm were observed. These peaks were derived from energy band of Er^{3+}. Peaks of 344, 365, 488, and 662 nm were derived from absorptions of $^4I_{15/2} \rightarrow {}^4G_{5/2}$, $^4G_{9/2}$, $^4F_{7/2}$, and $^4F_{9/2}$ of Er^{3+}, respectively.

A. 3 Optical property of target materials

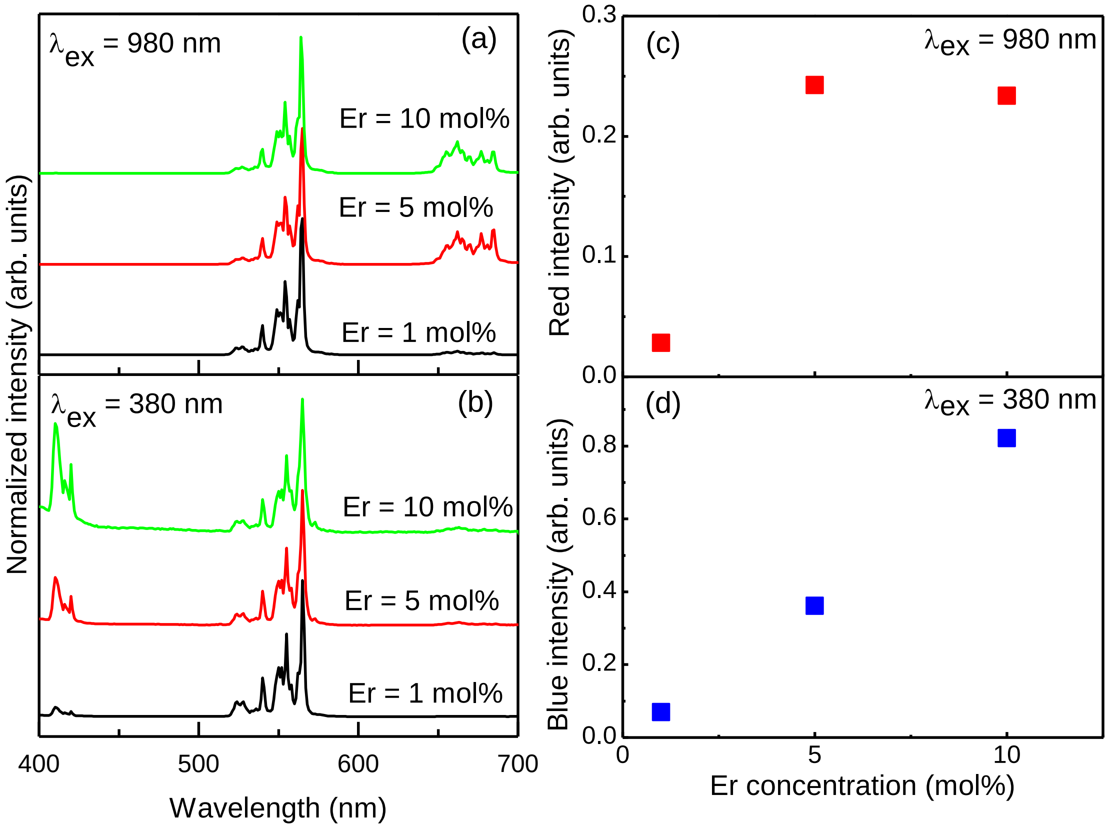

Figure A3. PL spectra of Y_2O_3:Er powder in excitation light of 980 nm (a) and 380 nm (b). Red intensity as function of Er concentration (c) and blue intensity as function of Er concentration (d).

Figure A3 (a) shows PL spectra of Y_2O_3:Er powder in excitation light of 980 nm. Er concentration was varied from 1 to 10 mol%. In excitation light of 980 nm, Er concentration was increased with increasing red emission intensity. In Er concentration of 10 mol%, however, red emission intensity was decreased. Decrease of the red emission would be caused by self-quenching (Figure A3 (c)). Also, Figure A3 (b) shows PL spectra of Y_2O_3:Er powder in excitation light of 380 nm. In excitation light of 380 nm, Er concentration was increased with increasing blue emission intensity.

A. 4 Observation of the ablated target with laser microscope

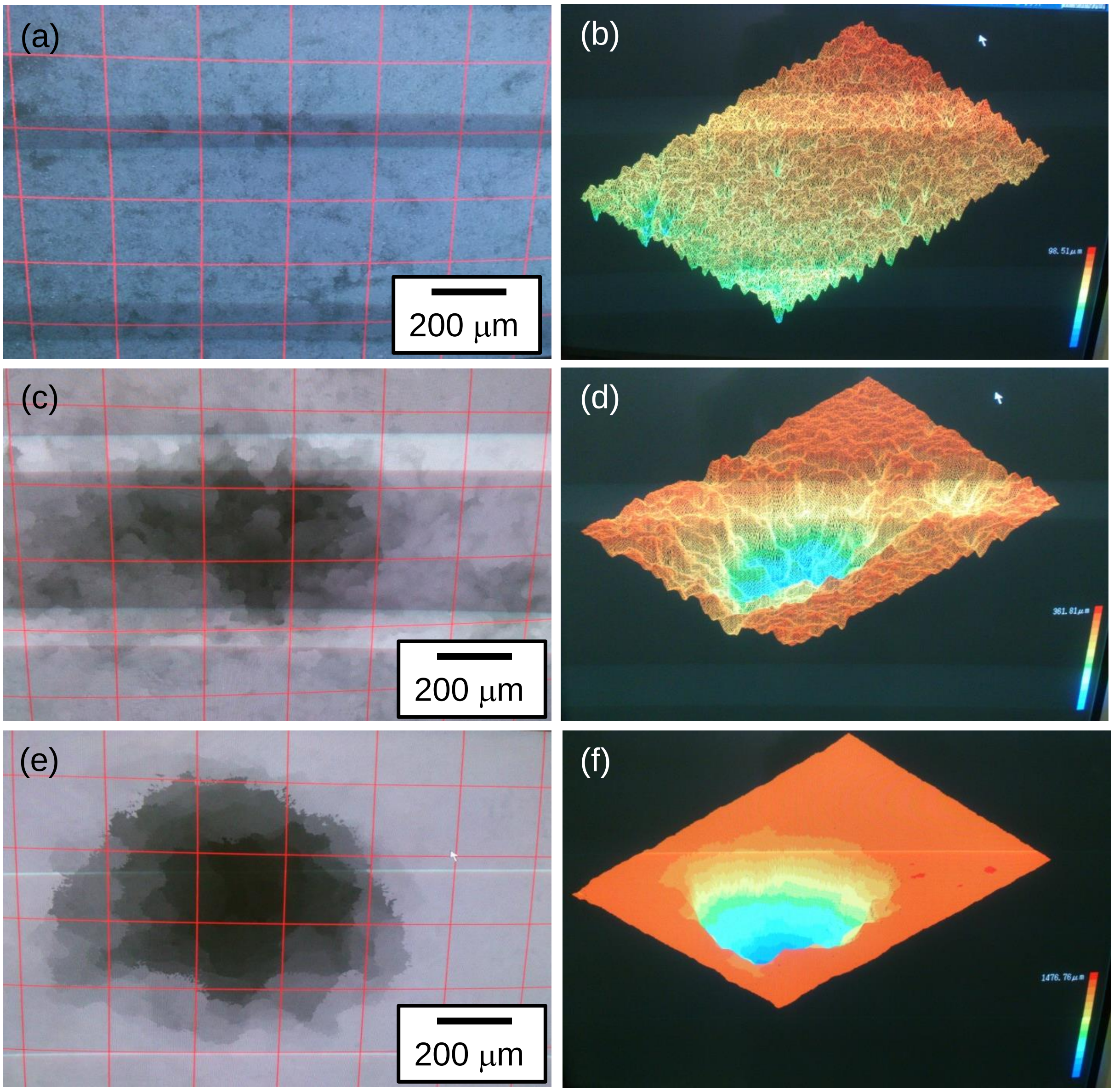

Figure A4. Laser microscope image of the ablated target: (a) two and (b) three dimensional images before laser irradiation, two (c) and three (d) dimensional images in laser fluence of 1.38 J/cm^2, and two (e) and three (f) dimensional images in laser fluence of 3.61 J/cm^2.

Figure A4 shows images of the target surface with laser microscope. Figure A4 (a) and (b) are the two and three dimensional images of target surface before laser irradiation, respectively. Flat surface was observed. Figure A4 (c), (d), (e) and (f) are the two and three dimensional images of target surface after laser irradiation, respectively. On the target surface, a hole formed by laser irradiation was observed. Productivity of the nanoparticles was calculated from volume of the hole. The results are showed in Table S1. The results of laser microscope observation were compared with those of ICP-MS. Although productivity of the nanoparticles in the laser microscope observation was nearly equal to that in ICP-MS, productivity in ICP-MS was a little more than that in the laser microscope observation. Upconversion powder would be detached from edge of the target by shock wave, which was generated by laser ablation in liquid.

Table S1. Productivity of nanoparticles calculated from laser microscope and ICP-MS.

Laser fluence (J/cm^2)	Productivity of nanoparticles calculated from laser microscope (mg)	Productivity of nanoparticles calculated from ICP-MS (mg)
3.61	1.32	1.35
1.38	0.19	0.24

A. 5 Laser ablation in polyvinylpyrrolidone (PVP)

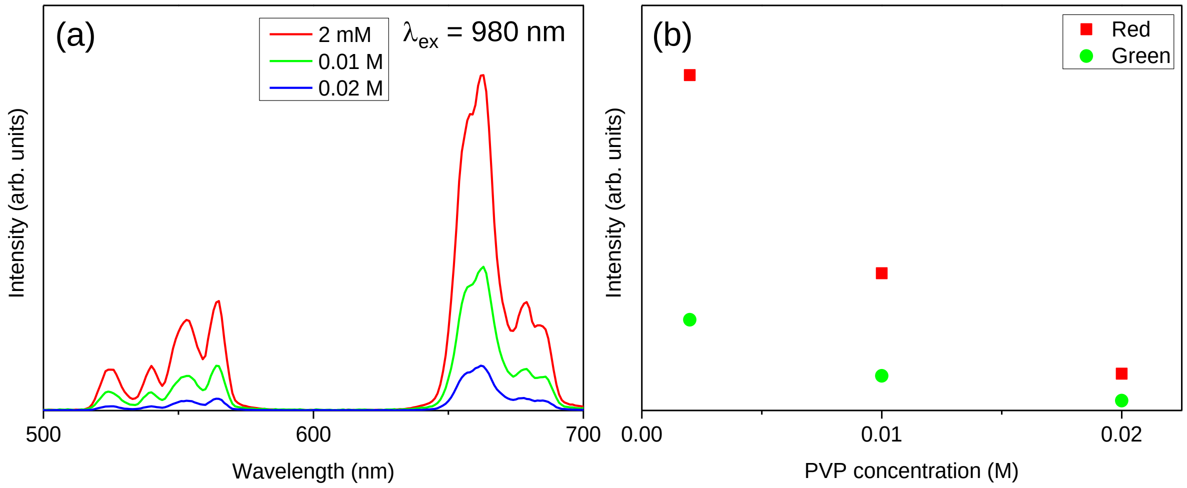

Figure A5. PL Spectra of Y_2O_3:Er,Yb colloidal solution prepared by laser ablation in PVP (a) and emission intensity as function of PVP concentration (b).

Laser ablation in PVP was carried out. Figure A5 (a) shows upconversion spectra of Y_2O_3:Er,Yb colloidal solution. The intensity of red ($^2F_{9/2} \rightarrow {}^4I_{15/2}$) and green ($^2H_{11/2}/^4S_{3/2} \rightarrow {}^4I_{15/2}$) under irradiating 980 nm LD were observed. Figure A5 (b) shows emission intensity as function of PVP concentration. PVP concentration was increased with decrease of emission intensity. PVP concentration increased with increase of viscosity of PVP. When viscosity of PVP was increased, cavitation bubble was hard to vanish. Because laser light was scattered by the cavitation bubble, productivity of the nanoparticles was decreased. Therefore, the emission intensity was decreased by decreasing productivity of the nanoparticles.

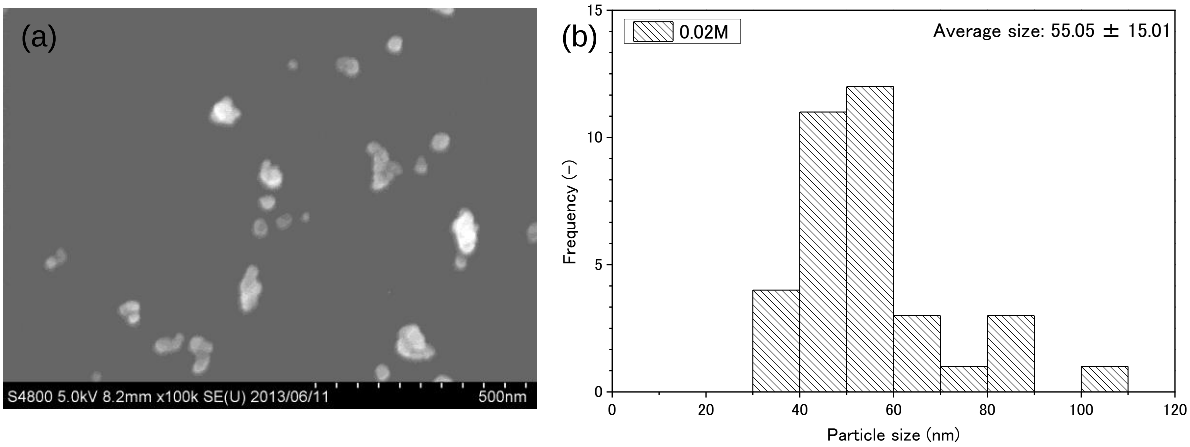

Figure A6. SEM image of Y_2O_3:Er,Yb nanoparticles prepared by laser ablation in PVP (0.02 M) (a) and histogram of the nanoparticles (b).

Figure A6 (a) and (b) shows SEM image of Y_2O_3:Er,Yb nanoparticles prepared by laser ablation in PVP (0.02 M) and histogram of the nanoparticles, respectively. From these results, nanoparticles around 55 nm were observed. Compared to particle of target, smaller nanoparticles were observed (Figure 3-4). When viscosity of PVP is high, movement of nanoparticles is confined. Therefore, particle size would be decreased by pulse laser irradiation.

Accomplishments

Journal publication

1) **Takashi Nunokawa**, Yuji Onodera, Masahiko Hara, Yoshitaka Kitamoto, Osamu Odawara, and Hiroyuki Wada, "Preparation of Y_2O_3:Er,Yb nanoparticles by laser ablation in liquid" *Applied Surface Science* 261 (2012) 118-122.
2) **Takashi Nunokawa**, Yuji Onodera, Hikaru Kobayashi, Tsuyoshi Asahi, Osamu Odawara, and Hiroyuki Wada, "Upconversion luminescence properties of Y_2O_3:Er,Yb colloid prepared by laser ablation in liquid" *Journal of Ceramic Processing Research* 14 (2013) s1-s4.
3) **Takashi Nunokawa**, Yuji Onodera, Kunio Fujii, Fumitaka Yoshimura, Osamu Odawara and Hiroyuki Wada, "Preparation and characterization of highly-crystalline fine particles by laser" *Journal of Japan Laser Processing Society* 20 (2013) 38-40. (in Japanese)
4) **Takashi Nunokawa**, Osamu Odawara, and Hiroyuki Wada, "Optical properties of highly crystalline Y_2O_3:Er,Yb nanoparticles prepared by laser ablation in water" To be submitted.

Related works

1) Yuji Onodera, **Takashi Nunokawa**, Osamu Odawara, and Hiroyuki Wada, "Upconversion properties of Y_2O_3:Er,Yb nanoparticles prepared by laser ablation in liquid" *Journal of Luminescence* 137 (2013) 220-224.
2) Yuji Onodera, **Takashi Nunokawa**, Osamu Odawara, and Hiroyuki Wada, "Photon-avalanche effect of Y_2O_3:Er,Yb nanoparticles prepared by laser ablation in liquid" *Transactions of the Materials Research Society of Japan* 38 (2013) 317-320.

Presentation lists

(International meetings)

1) **Takashi Nunokawa**, Yuji Onodera, Kazutaka Nakamura, Osamu Odawara, and Hiroyuki Wada "Preparation of Y_2O_3:Er,Yb colloidal solution by laser ablation in liquid" *JOINT CONFERENCE OF 5th INTERNATIONAL CONFERENCE ON SCIENCE AND TECHNOLOGY FOR ADVANCED CERAMICS (STAC5)*, Mielparque-Yokohama, Yokohama, Kanagawa, Japan, Jun. 22-24, 2011.
2) **Takashi Nunokawa**, Yuji Onodera, Hikaru Kobayashi, Tsuyoshi Asashi, Osamu Odawara, and Hiroyuki Wada: "Optical property of upconversion colloidal solution prepared by laser ablation in liquid" *PHOSPHOR SAFARI*, Niigata, Japan, Nov. 21-23, 2011.
3) **Takashi Nunokawa**, Yuji Onodera, Osamu Odawara, and Hiroyuki Wada "Optical properties and preparation of Er^{3+}, Yb^{3+} doped Y_2O_3 nanoparticles by laser ablation in liquid" *Tokyo Tech – EPFL Joint Workshop, Joint Workshop in Hakone*, Gora Seiunso, Hakone-machi, Kanagawa, Japan, Jan. 30 - Feb. 3, 2012.

4) **Takashi Nunokawa**, Yuji Onodera, Masahiko Hara, Yoshitaka Kitamoto, Osamu Odawara, and Hiroyuki Wada “Effects of energy densities on preparation of Y_2O_3:Er,Yb nanoparticles by laser ablation in liquid” *JOINT CONFERENCE OF 6th INTERNATIONAL CONFERENCE ON SCIENCE AND TECHNOLOGY FOR ADVANCED CERAMICS (STAC6),* Mielparque-Yokohama, Yokohama, Kanagawa, Japan, Jun. 26-28, 2012.
5) **Takashi Nunokawa**, Yuji Onodera, Anna Gubarevich, Osamu Odawara, and Hiroyuki Wada “Preparation rate of Y_2O_3:Er,Yb nanoparticles by laser ablation in liquid” *5th International Symposium on Advanced Plasma Science and its Applications for Nitrides and Nanomaterials (ISPlasma 2013),* Nagoya University, Toyama Campus, Nagoya, Aichi, Japan, Jan. 28 - Feb. 1, 2013.
6) **Takashi Nunokawa**, Osamu Odawara, and Hiroyuki Wada “Y_2O_3:Er,Yb Nano-String Prepared by Laser Ablation in Liquid” *8th International Conference on Reactive Plasmas/31st Symposium on Plasma Processing (ICRP-8/SPP-31),* Fukuoka Convention Center, Fukuoka, Japan, Feb. 3-7, 2014.
7) **Takashi Nunokawa**, Osamu Odawara, and Hiroyuki Wada “Upconversion Nanoparticles Prepared by Laser Ablation in Liquid” *The Workshop on Education and Research Center for Materials Innovation,* Tokyo Institute of Technology, Ookayama Campus, Kuramae Hall, Tokyo, Japan, Feb. 6, 2014.

(Domestic meetings)

1) **Takashi Nunokawa**, Yuji Onodera, Kazutaka Nakamura, Masahiko Hara, Osamu Odawara, and Hiroyuki Wada “Effect of energy densities on preparation of Y_2O_3:Er,Yb colloidal solution by laser ablation in liquid” *The 59th Spring Meeting, The Japan Society of Applied Physics,* Waseda University, Waseda Campus, Tokyo, Japan, Mar. 15-18, 2012.
2) **Takashi Nunokawa**, Yuji Onodera, Anna Gubarevich, Osamu Odawara, and Hiroyuki Wada “Optical properties and preparation of Y_2O_3:Er,Yb nanoparticles by laser ablation in liquid” *80th Spring Meeting, The Electrochemical Society of Japan,* Tohoku University, Kawauchi Campus, Miyagi, Japan, Mar. 29-31, 2013.
3) **Takashi Nunokawa**, Osamu Odawara, and Hiroyuki Wada “Morphology of Y_2O_3:Er,Yb nanoparticles prepared by laser ablation in liquid” *Symposium “液相高密度エネルギーナノ反応場” Pre-ANGEL 2014,* National Institute of Advanced Industrial Science and Technology, Tokyo Waterfront, Tokyo, Japan Aug. 8-9, 2013.
4) **Takashi Nunokawa**, Osamu Odawara, and Hiroyuki Wada “Characterization of Y_2O_3:Er,Yb nano-string prepared by laser ablation in liquid” *Fall Meeting, The Electrochemical Society of Japan,* Tokyo Institute of Technology, Ookayama Campus, Tokyo, Japan, Sep. 27-28, 2013.

Patent

特願 2011-147041

「蛍光粒子およびその製造方法」　発明者: 小野寺　裕司, 布川　貴史, 中村　一隆, 廣田　順二, 小田原　修,　和田　裕之 出願人:国立大学法人東京工業大学　出願日:2011/07/01

Acknowledgements

When I was in Tokyo Institute of Technology, Interdisciplinary Graduate School of Science and Engineering, Department of Innovative and Engineered Materials, Doctor Course, this study was performed under the guidance by Associate Professor Hiroyuki Wada in the same university. I would like to thank greatly Associate Professor Hiroyuki Wada for passionate guidance and great advice. I would like to thank greatly Professor Osamu Odawara for great advice on the research activities.

I would like to thank greatly Professor Osamu Odawara, Professor Mamoru Yoshimoto, Professor Masahiko Hara, and Associate Professor Kazutaka Nakamura for judge of this doctoral dissertation.

I would like to thank greatly Professor Tsuyoshi Asahi (Department of Material Science and Biotechnology, Graduate School of Science and Engineering, Ehime University) for collaborative research.

I would like to thank greatly Assistant Professor Anna V Gubarevich and Assistant Professor Junko Habasaki for great advice on the research activities.

I would like to thank greatly Nakamura laboratory (Materials and Structures Laboratory, Tokyo Tech) for using laser equipment, Yamaguchi laboratory (Chemical Resource Laboratory, Tokyo Tech) for using SEM, Hara·Hayashi laboratory (Department of Electronic Chemistry, Tokyo Tech) for using DLS, and Tsuge laboratory (Department of Innovative and Engineered Materials, Tokyo Tech) for using experimental equipment.

I would like to thank greatly Mr. Yuichi Suzuki and Mr. Hiroshi Iida (Center for Advanced Materials Analysis, Tokyo Tech) for XRD measurement, Mr. Katsuaki Hori and Mr. Naoyuki Hatakeyama (Center for Advanced Materials Analysis, Tokyo Tech) for TEM-EDX measurement, Dr. Teruaki Fuchigami (Matsushita laboratory, Materials and Structures Laboratory, Tokyo Tech) for TEM measurement, and Mr. Shinpei Nakamura for (Center for Advanced Materials Analysis, Tokyo Tech) ICP measurement.

I would like to thank greatly Mr. Shin Imamura (Hitachi research laboratory, Hitachi, Ltd) for great advice in internship.

I would like to thank greatly Professor Kenji Furuta (Innovative and Inventor Development Platform, Tokyo Tech), Mr. Yoshiro Mikami, and Mr. Hiroki Kaneko (Hitachi research laboratory, Hitachi, Ltd) for giving an opportunity of internship.

At every day research life of Odawara-Wada-Kondo group, I would like to thank greatly Dr. Kengo Ikema, Mr. Masayoshi Takeuchi, Mr. Hiroki Tanaka, Mr. Satoshi Yamagushi, Mr. Kazuki

Komoriya, Mr. Kei Nishihara, Mr. Yuji Onodera, Miss. Mika Ishizaki, Miss. Patterin Chewchinda, Mr. Ryuma Malik Matsuda, Mr. Yoshiki Igarashi, Mr. Naoyuki Karasawa, Mr. Hikaru Kobayashi, Mr. Hiroki Kobayshi, Mr. Noriyuki Tsuruoka, Mr. Kunio Fuji, Mr. Kazuhiro Gotoh, Mr. Sho Koyama, Mr. Masanori Hiraoka, Mr. Tomohiro Ikehata, Mr. Junpei Iwasaki, Mr. Tatsuya Numa, Mr. Nobutaka Tanishima, Mr. Satoshi Yone, Mr. Kosuke Kawasoe, Mr. Kazuhei Hayashi, and Mr. Kazuki Mori.

Finally, I deeply appreciate my parents and my brother. They gave me an opportunity to study and grow up in my life.

Takashi Nunokawa
March 2014